Fizika Nizkikh Temperatur, 2008, v. 34, No. 1, p. 3–44

X-ray magnetic circular dichroism in *d* and *f* ferromagnetic materials: recent theoretical progress. Part I

(Review Article)

V.N. Antonov, A.P. Shpak

Institute of Metal Physics, 36 Vernadskii Str., Kiev 03142, Ukraine
E-mail: antonov@imp.kiev.ua

A.N. Yaresko

Max-Planck-Institut for the Physics of Complex Systems, Dresden D-01187, Germany

Received April 10, 2007

The current status of theoretical understanding of the x-ray magnetic circular dichroism (XMCD) of 3*d* compounds is reviewed. Energy band theory based upon the local spin-density approximation (LSDA) describes the XMCD spectra of transition metal compounds reasonably well. Examples which we examine in detail are XPt_3 compounds (with X = V, Cr, Mn, Fe, Co, and Ni) in the $AuCu_3$ structure, Heusler compounds Co_2MnGe, Co_2NbSn, and compounds with noncollinear magnetic structure IrMnAl and Mn_3ZnC. Recently achieved improvements for describing the electronic and magnetic structures of 3*d* compounds are discussed.

PACS: 75.50.Cc Other ferromagnetic metals and alloys;
71.20.Lp Intermetallic compounds;
71.15.Rf Relativistic effects.

Keywords: electronic structure, density of electronic states, x-ray absorption spectra, x-ray magnetic circular dichroism, spin-orbit coupling, orbital magnetic moments.

Contents

1. Introduction

In 1845 Faraday discovered [1] that the polarization vector of linearly polarized light is rotated upon transmission through a sample that is exposed to a magnetic field parallel to the propagation direction of the light. About 30 years later, Kerr [2] observed that when linearly polarized light is reflected from a magnetic solid, its polarization plane also becomes rotated over a small angle with respect

to that of the incident light. This discovery has become known as the magneto-optical (MO) Kerr effect. Since then, many other magneto-optical effects, as for example the Zeeman, Voigt and Cotton–Mouton effects [3], have been discovered. These effects all have in common that they depend on the fact that the interaction of polarized light with a magnetic solid depends on its polarization.

The quantum mechanical understanding of the Kerr effect began as early as 1932 when Hulme [4] proposed that the Kerr effect could be attributed to spin-orbit (SO) coupling (see, also Kittel [5]). The symmetry between left- and right-hand circularly polarized light is broken due to the SO coupling in a magnetic solid. This leads to different refractive indices for the two kinds of circularly polarized light, so that incident linearly polarized light is reflected with elliptical polarization, and the major elliptical axis is rotated by the so called Kerr angle from the original axis of linear polarization. The first systematic study of the frequency dependent Kerr and Faraday effects was developed by Argyres [6] and later Cooper presented a more general theory using some simplifying assumptions [7]. The very powerful linear response techniques of Kubo [8] gave general formulas for the conductivity tensor which are being widely used now. A general theory for the frequency dependent conductivity of ferromagnetic (FM) metals over a wide range of frequencies and temperatures was developed in 1968 by Kondorsky and Vediaev [9]. The first *ab initio* calculation of MO properties was made by Callaway with co-workers in the middle of the 1970s [10,11]. They calculated the absorption parts of the conductivity tensor elements σ_{xx} and σ_{xy} for pure Fe and Ni and obtained rather good agreement with experiment.

In 1975 the theoretical work of Erskine and Stern showed that the x-ray absorption could be used to determine the x-ray magnetic circular dichroism (XMCD) in transition metals when left- and right-circularly polarized x-ray beams are used [12]. In 1985 Thole et al. [13] predicted a strong magnetic dichroism in the $M_{4,5}$ x-ray absorption spectra of magnetic rare-earth materials, for which they calculated the temperature and polarization dependence. A year later this MXD effect was confirmed experimentally by van der Laan et al. [14] at the Tb $M_{4,5}$-absorption edge of terbium iron garnet. The next year Schütz et al. [15] performed measurements using x-ray transitions at the *K*-edge of iron with circularly polarized x-rays, where the asymmetry in absorption was found to be of the order of 10^{-4}. This was shortly followed by the observation of magnetic EXAFS [16]. A theoretical description for the XMCD at the Fe K-absorption edge was given by Ebert et al. [17] using a spin-polarized version of relativistic multiple scattering theory. In 1990 Chen et al. [18] observed a large magnetic dichroism at the $L_{2,3}$ edge of nickel metal. Full multiplet calculations for 3*d* transition metal $L_{2,3}$ edges by Thole and van der Laan [19] were confirmed by several measurements on transition metal oxides. First considered as a rather exotic technique, MXD has now developed as an important measurement technique for local magnetic moments. Whereas optical and MO spectra are often swamped by too many transitions between occupied and empty valence states, x-ray excitations have the advantage that the core state has a purely local wave function, which offers site, symmetry, and element specificity. Recent progress in devices for circularly polarized synchrotron radiation have now made it possible to explore the polarization dependence of magnetic materials on a routine basis. Results of corresponding theoretical investigations can be found e.g. in a review papers [20,21] and a book [22].

We have divided the work into two papers, with this paper I, concentrating on the description of the methods and the results for the 3*d* transition metal compounds including XPt_3 compounds (with X = V, Cr, Mn, Fe, Co, and Ni) in the $AuCu_3$ structure, Heusler compounds Co_2MnGe, Co_2NbSn, and compounds with noncollinear magnetic structure IrMnAl and Mn_3ZnC. Paper II is devoted to the electronic structure and XMCD spectra of 4*f* and 5*f* compounds. As examples of 4*f* group we consider GdN compound. We also present uranium 5*f* compounds. In those compounds where the 5*f* electrons are rather delocalized, the LSDA describes the XMCD spectra reasonably well. As example of this group we consider UFe_2. Particular differences occur for the uranium compounds where the 5*f* electrons are neither delocalized nor localized, but more or less semilocalized. Typical examples are UXAl (X = Co, Rh, and Pt), and UX (X = S, Se,Te). The semilocalized 5*f*'s are, however, not inert, but their interaction with conduction electrons plays an important role. We also consider the electronic structure and XMCD spectra of heavy-fermion compounds UPt_3, URu_2Si_2, UPd_2Al_3, UNi_2Al_3, and UBe_{13} where the degree of the 5*f* localization is increased in comparison with other uranium compounds. The electronic structure and XMCD spectra of UGe_2 which possesses simultaneously ferromagnetism and superconductivity also presented.

2. Theoretical framework

2.1 Magneto-optical effects

Magneto-optical effects refer to various changes in the polarization state of light upon interaction with materials possessing a net magnetic moment, including rotation of the plane of linearly polarized light (Faraday, Kerr rotation), and the complementary differential absorption of left and right circularly polarized light (circular dichroism). In the near visible spectral range these effects result from excitation of electrons in the conduction band. Near x-ray absorption edges, or resonances, magneto-optical effects can

be enhanced by transitions from well-defined atomic core levels to transition symmetry selected valence states. There are at least two alternative formalisms for describing resonant soft x-ray MO properties. One uses the classical dielectric tensor [20]. Another uses the resonant atomic scattering factor including charge and magnetic contributions [23,24]. The equivalence of these two description (within dipole approximation) is demonstrated in Ref. 25.

For the polar Kerr magnetization geometry and a crystal of tetragonal symmetry, where both the fourfold axis and the magnetization **M** are perpendicular to the sample surface and the z-axis is chosen to be parallel to them, the dielectric tensor is composed of the diagonal ε_{xx} and ε_{zz}, and the off-diagonal ε_{xy} component in the form

$$\varepsilon = \begin{pmatrix} \varepsilon_{xx} & \varepsilon_{xy} & 0 \\ -\varepsilon_{xy} & \varepsilon_{xx} & 0 \\ 0 & 0 & \varepsilon_{zz} \end{pmatrix}. \qquad (1)$$

A complete description of MO effects in this formalism is given by the four nonzero elements of the dielectric tensor or, equivalently, by the complex refractive index $n(\omega)$

$$n(\omega) \equiv \sqrt{\varepsilon(\omega)} = 1 - \delta(\omega) + i\beta(\omega) \qquad (2)$$

for several normal modes corresponding to the propagation of pure polarization states along specific directions in the sample. The solution of Maxwell's equations yields these normal modes [26]. One of these modes is for circular components of opposite $(\pm)$ helicity with wave vector $\mathbf{h} \,||\, \mathbf{M}$ having indexes

$$n_{\pm} = 1 - \delta_{\pm} + i\beta_{\pm} = \sqrt{\varepsilon_{xx} \pm i\varepsilon_{xy}}\ . \qquad (3)$$

The two other cases are for linear polarization with $\mathbf{h} \perp \mathbf{M}$ [25]. One has electric vector $\mathbf{E} \,||\, \mathbf{M}$ and index $n_{\|} = 1 - \delta_{\|} + i\beta_{\|} = \sqrt{\varepsilon_{zz}}$. The other has $\mathbf{E} \perp \mathbf{M}$ and $n_{\perp} = 1 - \delta_{\perp} + i\beta_{\perp} = \sqrt{(\varepsilon_{xx}^2 + \varepsilon_{xy}^2)/\varepsilon_{xx}}$.

At normal light incidence the complex Faraday angle given by [25,27]

$$\phi_F(\omega) = \theta_F(\omega) - i\eta_F(\omega) = \frac{\omega l}{2c}(n_+ - n_-) \qquad (4)$$

where c is the speed of light, $\theta_F(\omega)$ and $\eta_F(\omega)$ are the Faraday rotation and the ellipticity. The complex Faraday response describes the polarization changes to the incident linear polarization on propagation through the film of thickness l. (The incident linearly polarized light is a coherent superposition of two circularly waves of opposite helicity.)

Magnetic circular dichroism is first order in M (or ε_{xy}) and is given by $\beta_+ - \beta_-$ or $\delta_+ - \delta_-$, respectively, the later representing the magneto-optical rotation (MOR) of the plane of polarization (Faraday effect). Magnetic linear dichroism (MLD) $n_{\perp} - n_{\|}$ (also known as the Voigt effect) is quadratic in M. The Voigt effect is present in both ferromagnets and antiferromagnets, while the first order MO effects in the forward scattering beam are absent with the net magnetization in antiferromagnets.

The alternative consideration of the MO effects is based on the atomic scattering factor $f(\omega, q)$, which provides a microscopic description of the interaction of x-ray photons with magnetic ions. For forward scattering $(q = 0)$ $f(\omega) = Z + f'(\omega) + if''(\omega)$, where Z is the atomic number. $f'(\omega)$ and $f''(\omega)$ are the anomalous dispersion corrections related to each other by the Kramers-Kronig transformation. The general equivalence of these two formalisms can be seen by noting the one-to-one correspondence of terms describing the same polarization dependence for the same normal modes [25]. For a multicomponent sample they relate to δ and β through:

$$\delta(\omega) = \frac{2\pi c^2 r_e}{\omega^2} \sum_i Z_i f_i'(\omega) N_i \qquad (5)$$

$$\beta(\omega) = \frac{2\pi c^2 r_e}{\omega^2} \sum_i f_i''(\omega) N_i\ , \qquad (6)$$

where the sum is over atomic spheres, each having number density N_i, and r_e is the classical electron radius. The x-ray absorption coefficient $\mu^{\lambda}(\omega)$ of polarization λ may be written in terms of the imaginary part of $f_{\lambda}(\omega)$ as

$$\mu^{\lambda}(\omega) = \frac{4\pi r_e c}{\Omega\omega} f_{\lambda}''(\omega)\,, \qquad (7)$$

where Ω is the atomic volume. X-ray MCD which is the difference in x-ray absorption for right- and left-circularly polarized photons $(\mu^+ - \mu^-)$ can be presented by $(f_+'' - f_-'')$. Faraday rotation $\theta_F(\omega)$ of linear polarization measures MCD in the real part f_{λ}' of the resonant magnetic x-ray-scattering amplitude, i.e. [6],

$$\theta_F(\omega) = \frac{\omega l}{2c} \mathrm{Re}[n_+ - n_-] = \frac{\pi l r_e}{\Omega\omega}[f_-'(\omega) - f_+'(\omega)]\,. \qquad (8)$$

Finally, the scattering x-ray intensity from an elemental magnet at the Bragg reflection measured in the resonant magnetic x-ray-scattering experiments is just the squared modulus of the total scattering amplitude, which is a linear combination of $(f_{\pm}' + if_{\pm}''$, $f_z' + if_z'')$ with the coefficients fully determined by the experimental geometry [27]. Multiple scattering theory is usually used to calculate the resonant magnetic x-ray scattering amplitude $(f' + if'')$ [20,27,28].

We should mention that the general equivalence of the dielectric tensor and scattering factor descriptions holds only in the case considering dipole transitions contributing to atomic scattering factor $f(\omega)$. Higher-order multipole terms have different polarization dependence [23].

Using straightforward symmetry considerations it can be shown that all magneto-optical phenomena (XMCD,

MO Kerr and Faraday effects) are caused by symmetry reduction, in comparison to the paramagnetic state, caused by magnetic ordering [29]. XMCD properties are only manifest when SO coupling is considered in addition. The theoretical description of magnetic dichroism can be cast into four categories. On the one hand, there are one-particle (ground-state) and many-body (excited-state) theories; on the other hand, there are theories for single atoms and those which take into account the solid state. To name a few from each category, for atomic one-particle theories we refer to Refs. 30 and 31, for atomic many-particle multiplet theory to Refs. 32–35, for solid many-particle theories to Ref. 36, and for solid one-particle theories (photoelectron diffraction) to Refs. 37–40. A multiple-scattering approach to XMCD, a solid-state one-particle theory, has been proposed by Ebert et al. [41–43] and Tamura et al. [44].

To calculate the XMCD properties one has to account for magnetism and SO coupling at the same time when dealing with the electronic structure of the material considered. Performing corresponding band structure calculations, it is normally sufficient to treat SO coupling in a perturbative way. A more rigorous scheme, however, is obtained by starting from the Dirac equation set up in the framework of relativistic spin density functional theory [45]:

$$[c\boldsymbol{\alpha}\cdot\mathbf{p}+\beta mc^2+\mathbf{I}V+V_{sp}\beta\sigma_z]\psi_{n\mathbf{k}}=\varepsilon_{n\mathbf{k}}\psi_{n\mathbf{k}} \qquad (9)$$

with $V_{sp}(\mathbf{r})$ being the spin-polarized part of the exchange-correlation potential corresponding to the z quantization axis, $\psi_{n\mathbf{k}}$ is the four-component Bloch electron wave function. All other parts of the potential are contained in $V(\mathbf{r})$. The 4×4 matrices $\boldsymbol{\alpha}, \beta$, and $\mathbf{I}$ are defined by

$$\boldsymbol{\alpha}=\begin{pmatrix}0 & \boldsymbol{\sigma}\\ \boldsymbol{\sigma} & 0\end{pmatrix},\ \beta=\begin{pmatrix}1 & 0\\ 0 & -1\end{pmatrix},\ \mathbf{I}=\begin{pmatrix}1 & 0\\ 0 & 1\end{pmatrix}, \qquad (10)$$

where $\boldsymbol{\sigma}$ are the standard Pauli matrices, and $\mathbf{I}$ is the 2×2 unit matrix.

There are quite a few band structure methods available now that are based on the above Dirac equation [45]. In one of the schemes the basis functions are derived from the proper solution of the Dirac equation for the spin dependent single-site potentials. In another one, the basis functions are obtained initially by solving the Dirac equation without the spin-dependent term and then this term is accounted for in the variational step. In spite of this approximation, the latter scheme gives results in a close agreement with the former, while being simpler to implement.

Within the one-particle approximation, the absorption coefficient μ for incident x-ray of polarization λ and photon energy $\hbar\omega$ can be determined as the probability of electron transition from an initial core state (with wave function ψ_j and energy E_j) to a final unoccupied state (with wave function $\psi_{n\mathbf{k}}$ and energy $E_{n\mathbf{k}}$)

$$\mu_j^{\lambda}(\omega)=\sum_{n\mathbf{k}}|\langle\Psi_{n\mathbf{k}}|\Pi_\lambda|\Psi_j\rangle|^2\,\delta(E_{n\mathbf{k}}-E_j-\hbar\omega)\,\theta(E_{n\mathbf{k}}-E_F). \qquad (11)$$

The Π_λ is the dipole electron-photon interaction operator

$$\Pi_\lambda=-\varepsilon\boldsymbol{\alpha}\mathbf{a}_\lambda, \qquad (12)$$

where $\boldsymbol{\alpha}$ are the Dirac matrices, $\mathbf{a}_\lambda$ is the λ polarization unit vector of the photon potential vector [$a_\pm = 1/\sqrt{2}(1,\pm i,0)$, $a_z=(0,0,1)$]. (Here +/– denotes, respectively, left- and right-circular photon polarizations with respect to the magnetization direction in the solid.) More detailed expressions of the matrix elements for the spin-polarized fully relativistic LMTO method may be found in Refs. 43,46.

While XMCD is calculated using equation (11), the main features can be understood already from a simplified expression for paramagnetic solids. With restriction to electric dipole transitions, keeping the integration only inside the atomic spheres (due to the highly localized core sates) and averaging with respect to polarization of the light one obtains the following expression for the absorption coefficient of the core level with (l, j) quantum numbers [47]:

$$\mu_{lj}^{0}(\omega)=\sum_{l',j'}\frac{2j+1}{4}\left(\frac{\delta_{l',l+1}\delta_{j',j+1}}{j+1}+\frac{\delta_{l',l-1}\delta_{j',j-1}}{j}+\right.$$
$$\left.+\frac{\delta_{l',l+1}\delta_{j',j}}{j(j+1)(2j+1)}\right)N_{l',j'}(E)C_{l,j}^{l',j'}(E) \qquad (13)$$

where $N_{l',j'}(E)$ is the partial density of empty states and the $C_{l,j}^{l',j'}(E)$ is radial matrix elements [47].

Equation (13) allows only transitions with $\Delta l=\pm 1$, $\Delta j=0,\pm 1$ (dipole selection rules) which means that the absorption coefficient can be interpreted as a direct measure for the sum of (l, j)-resolved DOS curves weighed by the square of the corresponding radial matrix element (which usually is a smooth function of energy). This simple interpretation is also valid for the spin-polarized case [20].

To compare the theoretically calculated and experimental XMCD spectra one has take into account the background intensity which affects the high energy part of the experimentally measured spectra due to different kind of inelastic scattering of the electron promoted to the conduction band above Fermi level (scattering on potentials of surrounding atoms, defects, phonons etc.). To calculate the background spectra can be used the model proposed by Richtmyer et al. [48]. The absorption coefficient for the background intensity is

$$\mu(\omega)=\frac{C\Gamma_c}{2\pi}\int_{E_{cf_0}}^{\infty}\frac{dE_{cf}}{(\Gamma_c/2)^2+(\hbar\omega-E_{cf})^2}, \qquad (14)$$

where $E_{cf} = E_c - E_f$, E_c and Γ_c are the energy and the lifetimes broadening of the core hole, E_f is the energy of empty continuum level, E_{f_0} is the energy of the lowest unoccupied continuum level, and C is a normalization constant which in this paper has been used as an adjustable parameter.

Concurrent with the development of the x-ray magnetic circular dichroism experiment, some important magneto-optical sum rules have been derived [49–52].

For the $L_{2,3}$ edges the l_z sum rule can be written as [22]

$$\langle l_z \rangle = n_h \frac{4 \int\limits_{L_3+L_2} d\omega(\mu_+ - \mu_-)}{3 \int\limits_{L_3+L_2} d\omega(\mu_+ + \mu_-)} \qquad (15)$$

where n_h is the number of holes in the d band $n_h = 10 - n_d$, $\langle l_z \rangle$ is the average of the magnetic quantum number of the orbital angular momentum. The integration is taken over the whole $2p$ absorption region. The s_z sum rule can be written as

$$\langle s_z \rangle + \frac{7}{2}\langle t_z \rangle = n_h \frac{\int\limits_{L_3} d\omega(\mu_+ - \mu_-) - 2\int\limits_{L_2} d\omega(\mu_+ - \mu_-)}{\int\limits_{L_3+L_2} d\omega(\mu_+ + \mu_-)} \qquad (16)$$

where t_z is the z component of the magnetic dipole operator $\mathbf{t} = \mathbf{s} - 3\mathbf{r}(\mathbf{r}\cdot s)/|\mathbf{r}|^2$ which accounts for the asphericity of the spin moment. The integration $\int_{L_3}$ ($\int_{L_2}$) is taken only over the $2p_{3/2}$ ($2p_{1/2}$) absorption region.

For the K edges the l_z sum rule was proposed in Ref. 53 and can be written as

$$\langle l_z \rangle = n_h \frac{2 \int\limits_{K} d\omega(\mu_+ - \mu_-)}{3 \int\limits_{K} d\omega(\mu_+ + \mu_-)} \qquad (17)$$

where $\langle l_z \rangle$ represents the expectation value of orbital angular momentum, n_h is the number of empty states per atom in the $4p$ conduction bands. The integration is taken over the whole 1s absorption region.

2.2. LSDA + U method

The application of standard LSDA methods to f-shell systems meets with problems in most cases, because of the correlated nature of the f-electrons. To account better for the on-site f-electron correlations, we have adopted as a suitable model Hamiltonian that of the LSDA + U approach [54]. The main idea is the same as in the Anderson impurity model [55]: the separate treatment of localized f -electrons for which the Coulomb $f - f$ interaction is taken into account by a Hubbard-type term in the Hamiltonian $(1/2)U \sum\limits_{i \neq j} n_i n_j$ (n_i are f-orbital occupancies), and delocalized s, p, d electrons for which the local density approximation for the Coulomb interaction is regarded as sufficient.

Hubbard [56,57] was one of the first to point out the importance, in the solid state, of Coulomb correlations which occur inside atoms. The many-body crystal wave function has to reduce to many-body atomic wave functions as lattice spacing is increased. This limiting behavior is missed in the LDA/DFT. The spectrum of excitations for the shell of an f-electron system is a set of many-body levels describing processes of removing and adding electrons. In the simplified case, when every f electron has roughly the same kinetic energy ε_f and Coulomb repulsion energy U, the total energy of the shell with n electrons is given by $E_n = \varepsilon_f n + Un(n-1)/2$ and the excitation spectrum is given by $\varepsilon_n = E_{n+1} - E_n = \varepsilon_f + Un$.

Let us consider f ion as an open system with a fluctuating number of f electrons. The correct formula for the Coulomb energy of f–f interactions as a function of the number of f electrons N given by the LDA should be $E = UN(N-1)/2$ [58]. If we subtract this expression from the LDA total energy functional and add a Hubbard-like term (neglecting for a while exchange and non-sphericity) we will have the following functional:

$$E = E^{\mathrm{LDA}} - UN(N-1)/2 + \frac{1}{2}U \sum_{i \neq j} n_i n_j . \qquad (18)$$

The orbital energies ε_i are derivatives of (18):

$$\varepsilon_i = \frac{\partial E}{\partial n_i} = \varepsilon^{\mathrm{LDA}} + U\left(\frac{1}{2} - n_i\right). \qquad (19)$$

This simple formula gives the shift of the LDA orbital energy $-U/2$ for occupied orbitals ($n_i = 1$) and $+U/2$ for unoccupied orbitals ($n_i = 0$). A similar formula is found for the orbital dependent potential $V_i(\mathbf{r}) = \delta E/\delta n_i(\mathbf{r})$ where variation is taken not on the total charge density $\rho(\mathbf{r})$ but on the charge density of a particular ith orbita $n_i(\mathbf{r})$:

$$V_i(\mathbf{r}) = V^{\mathrm{LDA}}(\mathbf{r}) + U\left(\frac{1}{2} - n_i\right). \qquad (20)$$

Expression (20) restores the discontinuous behavior of the one-electron potential of the exact density-functional theory.

The functional (18) neglects exchange and non-sphericity of the Coulomb interaction. In the most general rotationally invariant form the LDA + U functional is defined as [59,60]

$$E^{\mathrm{LDA}+U}[\rho(\mathbf{r}), \hat{n}] = E^{\mathrm{L(S)DA}}[\rho(\mathbf{r})] + E^{U}(\hat{n}) - E^{\mathrm{dc}}(\hat{n}), \quad (21)$$

where $E^{\mathrm{L(S)DA}}[\rho(\mathbf{r})]$ is the LSDA (or LDA as in Ref. 58) functional of the total electron spin densities, $E^U(\hat{n})$ is the electron–electron interaction energy of the localized electrons, and $E^{\mathrm{dc}}(\hat{n})$ is the so-called «double counting» term which cancels approximately the part of an electron-electron energy which is already included in E^{LDA}. The last two terms are functions of the occupation matrix $\hat{n}$ defined using the local orbitals $\{\phi_{lm\sigma}\}$.

The matrix $\hat{n} = ||n_{\sigma m,\sigma' m'}||$ generally consists of both spin-diagonal and spin-non-diagonal terms. The latter can appear due to the spin-orbit interaction or a non-collinear magnetic order. Then, the second term in Eq. (21) can be written as [59–61]:

$$E^U = \frac{1}{2}\sum_{\sigma,\sigma',\{m\}} (n_{\sigma m_1,\sigma m_2} U_{m_1 m_2 m_3 m_4} n_{\sigma' m_3,\sigma' m_4} - n_{\sigma m_1,\sigma' m_2} U_{m_1 m_4 m_3 m_2} n_{\sigma' m_3,\sigma m_4}) \quad (22)$$

where $U_{m_1 m_2 m_3 m_4}$ are the matrix elements of the on-site Coulomb interaction which are given by

$$U_{m_1 m_2 m_3 m_4} = \sum_{k=0}^{2l} a^k_{m_1 m_2 m_3 m_4} F^k , \quad (23)$$

with F^k being *screened* Slater integrals for a given l and

$$a^k_{m_1 m_2 m_3 m_4} = \frac{4\pi}{2k+1}\sum_{q=-k}^{k} \langle lm_1|Y_{kq}|lm_2\rangle \langle lm_3|Y^*_{kq}|lm_4\rangle . \quad (24)$$

The $\langle lm_1|Y_{kq}|lm_2\rangle$ angular integrals of a product of three spherical harmonics Y_{lm} can be expressed in terms of Clebsch-Gordan coefficients and Eq. (24) becomes

$$a^k_{m_1 m_2 m_3 m_4} = \delta_{m_1 - m_2 + m_3, m_4} (C^{l0}_{k0,l0})^2 \times C^{lm_1}_{km_1 - m_2, lm_2} C^{lm_4}_{km_1 - m_2, lm_3} . \quad (25)$$

The matrix elements $U_{mmm'm'}$ and $U_{mm'm'm}$ which enter those terms in the sum in Eq. (22) which contain a product of the diagonal elements of the occupation matrix can be identified as have the usual meaning of pair Coulomb and exchange integrals

$$U_{mmm'm'} = U_{mm'}, \quad U_{mm'm'm} = J_{mm'} . \quad (26)$$

The averaging of the matrices $U_{mm'}$ and $U_{mm'} - J_{mm'}$ over all possible pairs of m, m' defines the averaged Coulomb U and exchange J integrals which enter the expression for E^{dc}. Using the properties of Clebsch–Gordan coefficients one can show that

$$U = \frac{1}{(2l+1)^2}\sum_{mm'} U_{mm'} = F^0, \quad (27)$$

$$U - J = \frac{1}{2l(2l+1)}{\sum_{mm'}}' (U_{mm'} - J_{mm'}) = F^0 - \frac{1}{2l}\sum_{k=2}^{2l} (C^{l0}_{n0,l0})^2 F^k , \quad (28)$$

where the primed sum is over $m' \neq m$. Equations (27) and (28) allow us to establish the following relation between the average exchange integral J and Slater integrals:

$$J = \frac{1}{2l}\sum_{k=2}^{2l} (C^{l0}_{n0,l0})^2 F^k , \quad (29)$$

or explicitly

$$J = \frac{1}{14}(F^2 + F^4) \quad \text{for} \quad l = 2 , \quad (30)$$

$$J = \frac{1}{6435}(286F^2 + 195F^4 + 250F^6) \quad \text{for} \quad l = 3 . \quad (31)$$

The meaning of U has been carefully discussed by Herring [62]. In, e.g., a f-electron system with nf-electrons per atom, U is defined as the energy cost for the reaction

$$2(f^n) \rightarrow f^{n+1} + f^{n-1} , \quad (32)$$

i.e., the energy cost for moving a f-electron between two atoms which both initially had nf-electrons. It should be emphasized that U is a renormalized quantity which contains the effects of screening by fast s and p electrons. The number of these delocalized electrons on an atom with $(n+1)f$-electrons decreases whereas their number on an atom with $(n-1)f$-electrons increases. The screening reduces the energy cost for the reaction given by Eq. (32). It is worth noting that because of the screening the value of U in L(S)DA + U calculations is significantly smaller then the bare U used in the Hubbard model [56,57].

In principle, the screened Coulomb U and exchange J integrals can be determined from supercell LSDA calculations using Slater's transition state technique [63] or from constrained LSDA calculations [64–66]. Then, the LDA + U method becomes parameter free. However, in some cases, as for instance for bcc iron [53], the value of U obtained from such calculations appears to be overestimated. Alternatively, the value of U estimated from the photo-emission spectroscopy (PES) and x-ray Bremsstrahlung isochromat spectroscopy (BIS) experiments can be used. Because of the difficulties with unambiguous determination of U it can be considered as a parameter of the model. Then its value can be adjusted so to achieve the best agreement of the results of LDA + U calculations with PES or optical spectra. While the use of an adjustable parameter is generally considered an anathema among first principles practitioners, the LDA + U approach does offer a plausible and practical method to

approximately treat strongly correlated orbitals in solids. It has been fond that many properties evaluated with the LDA + U method are not sensitive to small variations of the value of U around some optimal value. Indeed, the optimal value of U determined empirically is often very close to the value obtained from supercell or constrained density functional calculations.

2.3. General properties of spin density waves

The magnetic configuration of an incommensurate spin spiral shows the magnetic moments of certain atomic planes varying in direction. The variation has a well-defined period determined by a wave vector **q**. When the magnetic moment is confined to the lattice sites the magnetization **M** varies as [67]

$$\mathbf{M}(\mathbf{r}_n) = m_n \begin{bmatrix} \cos(\mathbf{q}\mathbf{r}_n + \phi_n)\sin(\theta_n) \\ \sin(\mathbf{q}\mathbf{r}_n + \phi_n)\sin(\theta_n) \\ \cos(\theta_n) \end{bmatrix}, \qquad (33)$$

where the polar coordinates are used and m_n is the magnetic moment of atom n with a phase ϕ_n at the position $\mathbf{r}_n$. Here we consider only planar spirals, that is, $\theta_n = \pi/2$ which also give the minimum of the total energy. The magnetization of Eq. (33) is not translationally invariant but transforms as

$$\mathbf{M}(\mathbf{r} + \mathbf{R}) = D(\mathbf{q}\mathbf{R})\mathbf{M}(\mathbf{r}), \qquad (34)$$

where **R** is a lattice translation and D is a rotation around the z axis. A spin spiral with a magnetization in a general point **r** in space can be defined as a magnetic configuration which transforms according to Eq. (34). Since the spin spiral describes a spatially rotating magnetization, it can be correlated with a frozen magnon.

Because the spin spiral breaks translational symmetry, the Bloch theorem is no longer valid. Computationally, one should use large super-cells to obtain total-energy of the spin spirals. However, when the spin-orbit interaction is neglected spins are decoupled from the lattice and only the relative orientation of the magnetic moments is important. Then, one can define generalized translations which contain translations in the real space and rotations in the spin space [68]. These generalized translations leave the magnetic structure invariant and lead to a generalized Bloch theorem. Therefore the Bloch spinors can still be characterized by a **k** vector in the Brillouin zone, and can be written as

$$\psi_k(\mathbf{r}) = \exp(i\mathbf{k}\mathbf{r}) \begin{pmatrix} \exp(-i\mathbf{q}\mathbf{r}/2)\, u_k(\mathbf{r}) \\ \exp(+i\mathbf{q}\mathbf{r}/2) d_k(\mathbf{r}) \end{pmatrix} \qquad (35)$$

The functions $u_k(\mathbf{r})$ and $d_k(\mathbf{r})$ are invariant with respect to lattice translations having the same role as for normal Bloch functions. Due to this generalized Bloch theorem the spin spirals can be studied within the chemical unit cell and no large super-cells are needed. Although the chemical unit cell can be used, the presence of the spin spiral lowers the symmetry of the system. Only the space-group operations that leave invariant the wave vector of the spiral remain. When considering the general spin space groups, i.e., taking the spin rotations into account, the space-group operations which reverse the spiral vector together with a spin rotation of π around the x axis are symmetry operations [68].

Although the original formulation of the local-spin-density approximation of density-functional theory allowed noncollinear magnetic order, first-principles calculations for this aspect have begun only recently (for a review, see Ref. 69). One application has been the study of noncollinear ground states, for example, in γ-Fe (Refs. 70–72) or in frustrated antiferromagnets [73,74]. In addition, the noncollinear formulation enables studies of finite-temperature properties of magnetic materials. Since the dominant magnetic excitations at low temperatures are spin waves which are noncollinear by nature, it is possible to determine the magnon spectra and ultimately the Curie temperature from first principles [75–79].

3. «Toy» XMCD spectra

In order to illustrate the effect of the symmetry breaking, caused by the simultaneous presence of the spin orbit coupling and spin polarization, and the matrix elements described in the previous section we present in Fig. 1 model K-edge XMCD spectra. These calculations are performed assuming that the absorption is determined by transitions between occupied «core» s states and completely empty «valence» p states. The spin splitting of the s states is neglected. All radial matrix elements are assumed to be equal. The spectra are obtained by Gaussian broadening of individual contributions from the transitions between the discrete atomic-like states. The length of vertical bars in Fig. 1 is proportional to the difference of the squared angular matrix elements for left- and right-circularly polarized photons.

When either the spin orbit coupling strength ξ or the effective magnetic field B is equal to zero, as in the lower panels of Fig. 1, p states with the quantum numbers $|\mu|$ and $-|\mu|$ are degenerate. The transitions with $\Delta\mu = \pm 1$ occur at the same energy and the absorption spectra for left- and right-circularly polarized x-rays are the same that leads to the absence of the dichroic signal. If both the SO coupling and magnetic field are switched on the degeneracy of the $\pm|\mu|$ states is lifted. Then, the transitions with $\Delta\mu = 1$ and $\Delta\mu = -1$ have different energies and no longer compensate each other which is reflected in the increasing magnitude of the XMCD spectra. If the p states were partially occupied the transition to the occupied states would be prohibited and the low frequency part of the

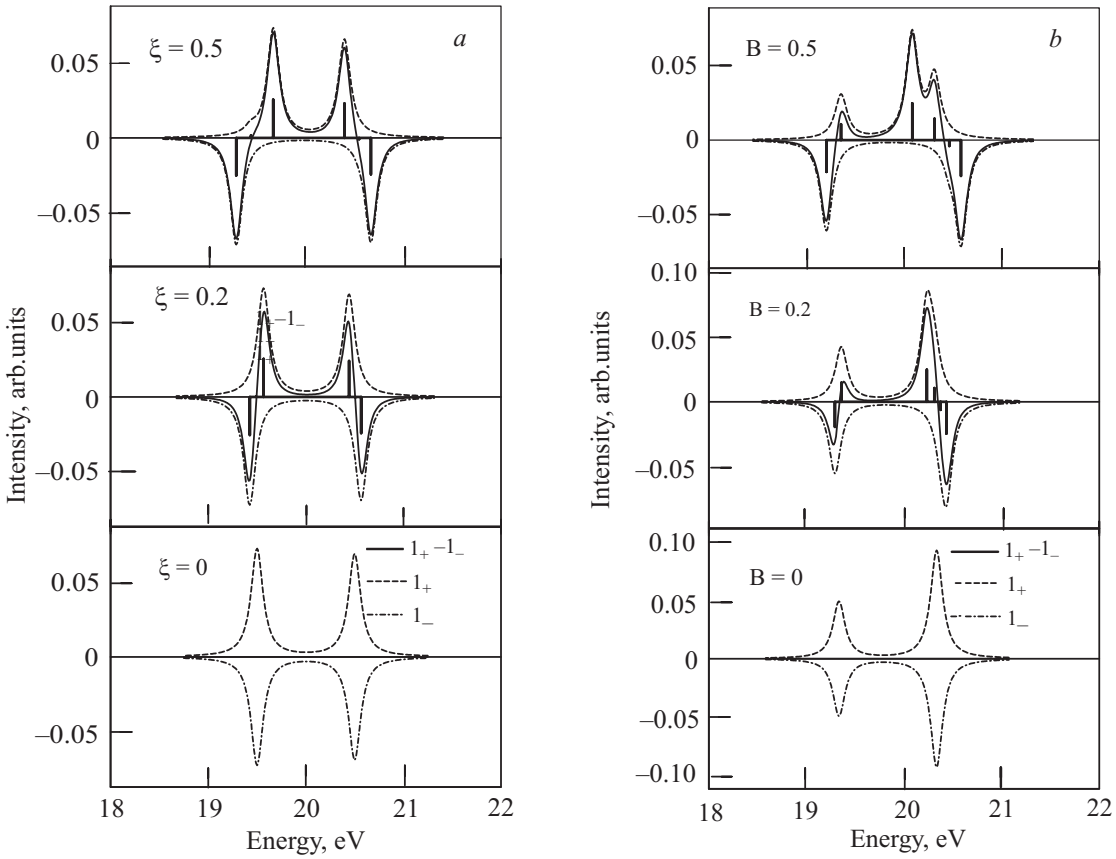

Fig. 1. Model *K*-edge XMCD spectra calculated for the cases of strong spin-polarization ($B = 1$) and increasing SO coupling (*a*) and strong SO coupling ($\xi = 1$) and increasing spin polarization (*b*) of the «valence» *p* electrons [21].

spectra up to the energy corresponding to the transition to the first unoccupied *p* state would become zero.

The dependence of the model $L_{2,3}$ XMCD spectra on ξ and *B* is illustrated by Fig. 2. In this example «core» *p* states are split by strong SO interaction into $p_{1/2}$ and $p_{3/2}$ sub-shells whereas their exchange splitting is set to zero. As a result a non-zero XMCD signal appears even if the spin orbit coupling of «valence» *d* states is neglected and only their spin-polarization is taken into account (lower panel in Fig. 2,*a*). This situation is typical for magnetic 3*d* metal compounds.

When the SO coupling of *d* states is strong they are also split into well separated $d_{3/2}$ and $d_{5/2}$ sub-shells (Fig. 2,*b*). One can note that because of the difference of the corresponding angular matrix elements L_3 spectrum is mainly formed by $p_{3/2} \to d_{5/2}$ transitions; the $p_{3/2} \to d_{3/2}$ contribution being much weaker. Similar to the case of the model *K* spectra switching on the magnetic field *B* lifts the degeneracy of $d_{\kappa,\mu}$ and $d_{\kappa,-\mu}$ states which, in turn, leads to the appearance of non-zero XMCD.

4. 3*d* metals and compounds

At the core level edge XMCD is not only element-specific but also orbital specific. For 3*d* transition metals, the electronic states can be probed by the *K*, $L_{2,3}$ and $M_{2,3}$ x-ray absorption and emission spectra. The experimental investigations at the *K* edge of 3*d* transition metals are relatively unproblematic to perform. Because dipole allowed transitions dominate the absorption spectrum for unpolarized radiation, the absorption coefficient $\bar{\mu}_K(E)$ reflects primarily the DOS of unoccupied $4p$-like states of 3*d* transition metals. The corresponding matrix elements for the $1s_{1/2} \to 4p_{1/2,3/2}$ transitions increase monotonically by nearly a factor 3 over the displayed range of energy in pure Fe and Ni [20]. Therefore there is no strict one-to-one correspondence $\mu_K(E)$ and $N_p(E)$. Because of the extremely small exchange splitting of the initial 1*s* state the exchange and spin-orbit splitting of the final $4p$-states that is responsible for the observed dichroism at the *K* edge. For this reason the dichroism in the terms of the difference in absorption $\Delta\mu_K = \mu_K^+ - \mu_K^-$ for left and right circularly polarized radiation $R_K = \Delta\mu_K/(2\bar{\mu}_K)$ is found to be only of order of 1%, being highest directly at the absorption edge [20].

Apart from the studies of XMCD spectra at the *K* edge on the pure elements Fe [15,80–85], Co [80,85], and Ni [83,85], many different systems have been investigated so far. *K* edge studies supply valuable additional information, for example, on the exchange coupling in compounds (Mn in PtMnSb [80], Fe in Fe_3Pt, FePt and $FePt_3$

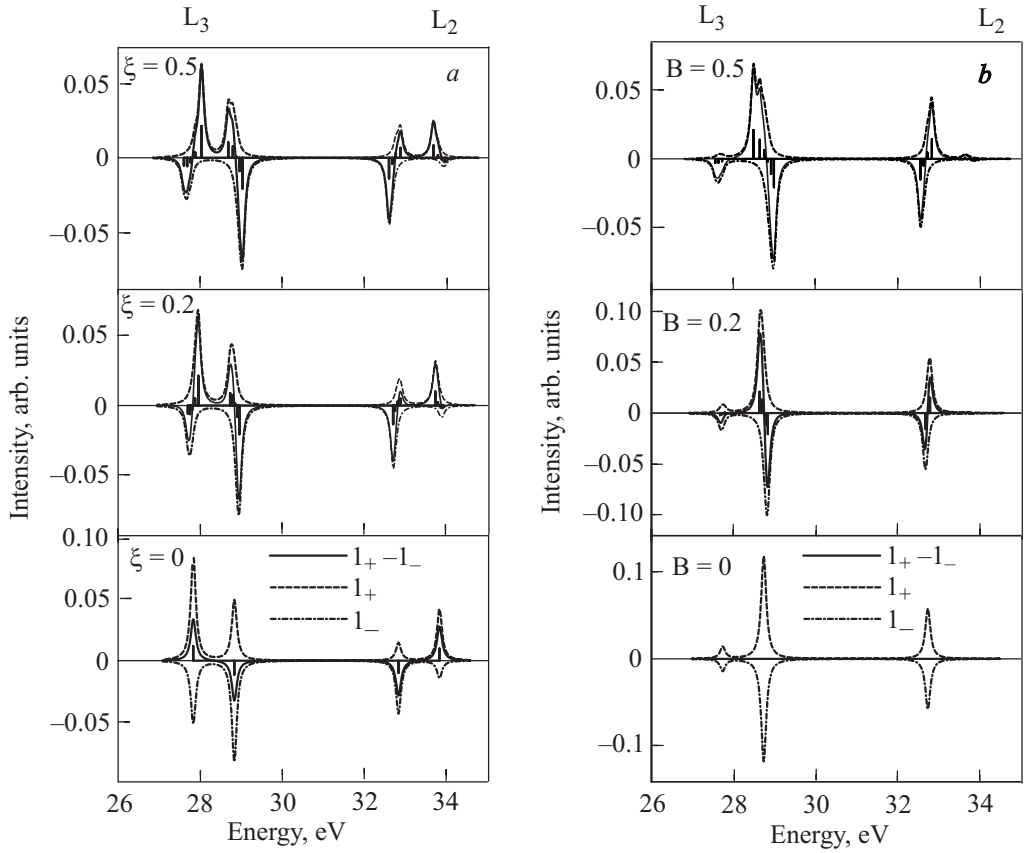

Fig. 2. Model $L_{2,3}$ XMCD spectra calculated for the cases of strong spin-polarization ($B = 1$) and increasing SO coupling (*a*) and strong SO coupling ($\xi = 1$) and increasing spin polarization (*b*) of the *d* electrons [21].

[86], Fe_2R with R = Ce, Sm, Gd, Tb, Tm, Lu [87], Fe_2Gd [88], Fe_nGd_m [87], $Nd_2Fe_{14}B$ [83], $Ce_2Fe_{17}H_x$ [89], alloys (Fe and Co in Fe_xCo_{1-x} [80,90], Fe and Ni in Fe_xNi_{1-x}) [91], Fe in Fe_xPt_{1-x} [80,92] and multilayer systems (Fe in Fe/Co [90], Fe/Cu [93,94], Fe/La [81], Fe/Ce [81], Fe/Nd [95,96], Fe/Gd [97], Co in Co/Cu [93,94,98], Cu in Co/Cu [93,94,98], Fe/Cu [93,94].

In contrast to the *K* edge, the dichroism spectra at the L_2 and L_3 edges are also influenced by the spin-orbit coupling of the initial $2p$ core states. In general, it gives rise to a very pronounced dichroism even if the local spin-polarization of the absorbing atom is rather small [20]. This was first demonstrated for the $L_{2,3}$ spectra of $5d$ transition metals dissolved substantially in Fe [20]. In these systems a relative difference in absorption for left- and right-circularly polarized radiation $R_{L_{2,3}}$ of up to 20% has been found. The first experimental investigation of XMCD at the $L_{2,3}$ edge of pure Ni have been done by Chen et al. [18]. Many different systems have been investigated experimentally so far, such as various diluted and concentrated alloy systems (Fe in Fe_xPd_{1-x} [99], Co in Co_xPd_{1-x} [99], Ni in Ni_xPd_{1-x} [99], Cr, Mn, Fe and Co in Ni [100]), compounds and multilayer systems (Fe and V in Fe/V [101,102], Co in Co/Ni, Co/Pd, Co/Pt [103], Co and Cu in Co/Cu [104]).

Ab initio calculations of the XMCD spectra of Fe, Co, and Ni at the *K* and $L_{2,3}$ edges have been carried out by a number of researches [20,43,105–111].

In the following four sections the results of theoretical investigations on the XMCD in some representative transition metal systems will be presented in details. They are transition-metal alloys consisting of a ferromagnetic $3d$ element and Pt atom, Heusler alloys and noncollinear IrMnAl and Mn_3ZnC compounds.

4.1. Cu_3Au-*type transition metal platinum alloys*

Transition-metal alloys consisting of a ferromagnetic $3d$ element and Pt have drawn attention over the last years due to their wide variety of magnetic properties. In these intermetallic compounds, the Pt sites have induced magnetic moments due to the hybridization with the transition metal spin-polarized $3d$ states. The contribution of the orbital moment to the total moment on the Pt sites is expected to be important because the Pt atom is so heavy (atomic number $Z = 78$) that the spin-orbit coupling of the Pt $5d$ electrons is fairly large (coupling constant $\zeta_{5d} = 0.5$ eV). The $3d$-Pt system also was found to have a good magneto-optical properties (see, e.g., Ref. 112–114). Especially multilayers of Co and Pt or Pd are at present intensively studied because of their potential application as optical storage material in MO storage devices [115,116].

Besides being of interest in applications, transition-metal platinum alloys XPt_3 and X_3Pt are interesting because the 3*d* electronic states in the former compounds have less direct overlap and are expected to be more localized relative to the 3*d* states in the X_3Pt materials. Also of interest is how the filling of the 3*d* band across the series affects the hybridization with the Pt 5*d* states and how this in turn affects the Pt spin and orbital moments.

The electronic structure, magnetic and MO properties of XPt_3 compounds have been investigated intensively both theoretically and experimentally. We briefly review the rather extensive number of studies below. Several band structure calculations within the local spin density approximation have been performed. Kübler calculated the spin magnetic moment of VPt_3 using the augmented spherical wave (ASW) method [117]. The electronic structure of several ordered phases of the Fe–Pt system, namely, Fe_3Pt, $FePt_3$, Fe_2Pt_2, and Fe_3Pt_5 have been investigated by Podgorny using the LMTO method [118]. Spin-polarized band structures of $MnPt_3$ and $FePt_3$ were reported by Hasegawa [119]. Tohyama et al. studied the systematic trends in the electronic structure and magnetic moments of XPt_3 (X = Ti, V, Cr, Mn, Fe, and Co) based on their tight-binding calculations [120]. Suda et al. carried out APW band calculations for $FePt_3$ in the nonmagnetic an antiferromagnetic phases [121]. Their calculated local magnetic moment at the Fe site agrees well with experiment. Shirai et al. performed spin-polarized band structure calculations for XPt_3 (X = V, Cr, Mn, Fe, Co) using the scalar-relativistic version of the LAPW method [122]. They obtained good agreement between their calculated and the experimental spin magnetic moment at the transition metal site. On the other hand, the calculated spin moment of Pt atom differs significantly from the observed magnetic moment due to neglect of the spin-orbit interaction. The self-consistent band structure calculations of Fe_3Pt were performed using a spin-polarized, scalar relativistic full-potential LAPW method in Ref. 123 to calculate the magnetic Compton profile. The orbital and spin magnetic moments of the Cu_3Au- type transition metal intermetallics XPt_3 (X = V, Cr, Mn, Fe, and Co) have been evaluated using the full-potential LAPW method with the spin-orbit interaction as a perturbation [124]. The calculation reproduced the experimental trend of the orbital and spin moments well. The orbital moment of Pt in $CoPt_3$ is, however, underestimated by a factor of about two. Energy band structure calculations for XPt_3 (X = V, Cr, Mn, Fe, Co) were performed in Refs. 125, 126 to investigate their MO properties by means of relativistic ASW and LMTO methods using the local spin density approximation. The electronic structure, optical conductivity tensor and MO spectra of $CoPt_3$ and Co_3Pt along with some other multilayered Co/Pt structures have been investigated experimentally and theoretically in Ref. 127.

Recently, Maruyama et al. measured magnetic circular x-ray dichroism for $CrPt_3$, $MnPt_3$, $CoPt_3$, and ferromagnetic Fe_3Pt and obtained an interesting variation in the orbital and spin magnetic moments on the Pt sites [128,129]. The spin magnetic moment of Pt in $CrPt_3$ almost vanishes and the orbital moment is about $-0.1\ \mu_B$, antiferromagnetically coupled with the Cr magnetic moment. On the other hand, the orbital moment of Pt in $MnPt_3$ vanishes almost completely and a small but positive spin component (of the order of $0.1\ \mu_B$ parallel to the transition metal moment) contributes to the Pt moment. In $CoPt_3$ and Fe_3Pt, the Pt orbital and spin components are positive and relatively larger (in the range 0.1 to $0.3\ \mu_B$). Magnetic circular dichroism in the x-ray absorption spectrum in the $2p$–$3d$ excitation region of the transition-metal element was also measured for ferromagnetic Cu_3Au-type alloys, $MnPt_3$, Fe_3Pt and $CoPt_3$ in Ref. 130. The x-ray magnetic circular dichroism and Faraday effect were studied in ordered and disordered Fe_3Pt at K- and L_3-edges in Ref. 131. Angle dependent XMCD experiments have been performed at both Co and Pt $L_{2,3}$ edges in two epitaxial (111) $CoPt_3$ thin films grown at 690 and 800 K [132]. The analysis of the angular variations of the 3*d* orbital magnetic moment shows a strong perpendicular magneto-crystalline anisotropy (PMA) for the film grown at 690 K. It was related to the existence of anisotropic chemical local order yielding the formation of microscopic Co-rich and Co-poor planar local regions. In contrast, films grown above 800 K possess no PMA. These changes were correlated to their isotropic fcc structure of $L1_2$ type. The MCD spectrum of ferromagnetic $CoPt_3$ was observed in the photon energy range of 50 to 80 eV in Ref. 133. MCD spectrum in the Pt $N_{6,7}$ ($4f \rightarrow 5d$) region shows very unusual features. This MCD spectral shape deviates significantly from the one expected by considering the conventional selection rule of the dipole transition. It was shown in the frame of the Anderson impurity model that the unusual line shape of the MCD is caused by a strong interference (Fano effect for resonant photoemission). X-ray Faraday rotation — the dispersive analogue of XMCD — has been measured near the platinum L edge of ferromagnetic disordered Fe_3Pt [134].

The electronic structure, spin and orbital magnetic moments and XMCD spectra of the series XPt_3, X = V, Cr, Mn, Fe, Co, Ni and X_3Pt (X = Fe, Co, Ni) reported in Ref. 135. The XAS and XMCD spectra were calculated at K, $L_{2,3}$ and $M_{2,3}$ edges for transition metals and $L_{2,3}$, $M_{2,3}$, $M_{4,5}$, $N_{2,3}$, $N_{4,5}$, $N_{6,7}$ and $O_{2,3}$ edges at Pt sites.

1. Magnetic moments. Orbital and spin magnetic moments are determined by the interplay of hybridization, exchange, and Coulomb interactions, crystal-field and spin-orbit coupling. Table 1 presents the calculated spin M_s and orbital M_l magnetic moments in XPt_3 and X_3Pt compounds. Our calculated results are in good agreement

Table 1. Calculated spin M_s and orbital M_l magnetic moments (in μ_B) of XPt_3 and X_3Pt compounds [135].

		X atom		*Pt* atom	
	X	M_s	M_l	M_s	M_l
XPt_3	V	1.3751	0.0141	–0.0509	–0.0276
	Cr	2.6799	0.1789	–0.0300	–0.0558
	Mn	3.6985	0.0239	0.1244	–0.0014
	Fe	3.1370	0.1004	0.3045	0.0534
	Co	1.7079	0.0401	0.2384	0.0486
	Ni	0.4379	–0.0770	0.0780	0.0305
X_3Pt	Fe	2.5062	0.0870	0.2889	0.0522
	Co	1.6379	0.0786	0.3153	0.0687
	Ni	0.5178	0.0198	0.2343	0.0866

with those from the FLAPW calculations by Iwashita et al. [124]. The variation in the spin and orbital magnetic moments calculated inside the 3*d* transition metal and Pt atomic spheres in the XPt_3 intermetallics is compared with the experimentally measured moments in Fig. 3. The magnetic moments of the XPt_3 alloys were studied experimentally through neutron-scattering experiments already years ago [136,137]. These experiments showed that $CoPt_3$ and $MnPt_3$ are ferromagnets, while $CrPt_3$ and VPt_3 are ferrimagnets, and $FePt_3$ is an antiferromagnet. The calculated spin magnetic moments of $CoPt_3$ and $MnPt_3$ at the 3*d* site are in good agreement with the experiment, and for $CrPt_3$ and VPt_3 the ferrimagnetic structure is in accordance with experiment, but the values of the moments are less accurately reproduced. Due to band filling, linear and symmetric behavior centered at $MnPt_3$ is clearly seen in the spin magnetic moments on the 3*d* transition metal sites (Fig. 3,*a*.)

The characteristic feature of the electronic structure of XPt_3 compounds is the strong hybridization of transition metal 3*d* and Pt 5*d* states, the later being much more delocalized. Figure 4 shows the spin- and site-projected densities of the electronic states (DOS) for the transition metal site and the Pt site in XPt_3 compounds. Strong spin-orbit interaction in the Pt atomic sphere results in splitting of $d_{3/2}$ and $d_{5/2}$ states with the energy difference between their centers being ~1.5 eV. Inside the X atomic spheres the effect of the spin-orbit coupling is much weaker than the effect of the exchange field. The centers of both Pt $d_{3/2}$ and $d_{5/2}$ states lie at lower energies than the centers of the corresponding X *d* states. As a result of the X *d* – Pt *d* hybridization, the electronic states at the bottom of the valence band are formed mainly by Pt states while the states in the vicinity of the Fermi level E_F have predominantly transition metal *d* character with an

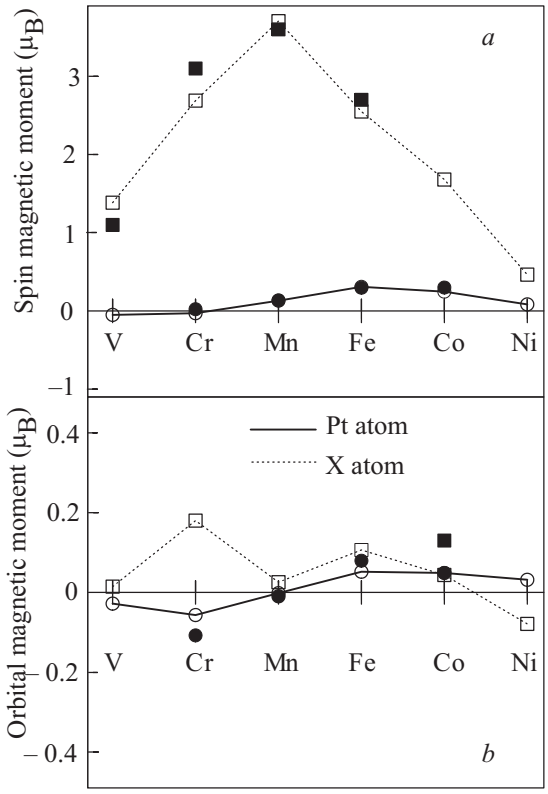

Fig. 3. Theoretically calculated spin (*a*) and orbital (*b*) magnetic moments on the Pt sites (open circles) and X sites (open squares) [135] in comparison with the experimental data for XPt_3 and Fe_3Pt compounds. The experimental Pt orbital moments (solid circles) for X = Cr, Mn, and Fe are from Ref. 129, Co orbital (solid square) and Pt orbital for $CoPt_3$ are from Ref. 132, the experimental spin magnetic moments on X sites (solid squares) are from Ref. 136 and on Pt sites (solid circles) from Ref. 138.

admixture of Pt *d* states. The hybridization with the exchange split X *d* states leads to a strong polarization of Pt *d* states near E_F. The resulting difference in occupation numbers for Pt states with the opposite spin projections gives rise to the appearance of a comparatively large spin magnetic moment at the Pt site. A large energy splitting between the spin-up and spin-down bands is found only for states with predominant 3*d* character. The minority-spin 3*d* states form rather narrow bands located near the top of the Pt *d* band in XPt_3 compounds. It is definitely seen in Fig. 4 that, as one proceeds from the lighter to heavier 3*d* elements, the spin-up 3*d* band is first filled up to $MnPt_3$ and then electrons start to occupy the spin-down 3*d* band. This explains the linear and symmetric behaviors in the spin moments of the 3*d* atoms mentioned above.

The Pt spin moment reflects hybridization of the Pt 5*d* states with the 3*d* bands. At the beginning of 3*d* series (VPt_3 and $CrPt_3$) and at the end ($NiPt_3$) the spin magnetic moment at Pt sites is very small. The spin-up 3*d* bands in $MnPt_3$, $FePt_3$, and $CoPt_3$ are nearly filled, therefore the spin-down hole in the Pt *d* states mixes with the empty 3*d* bands. Due to

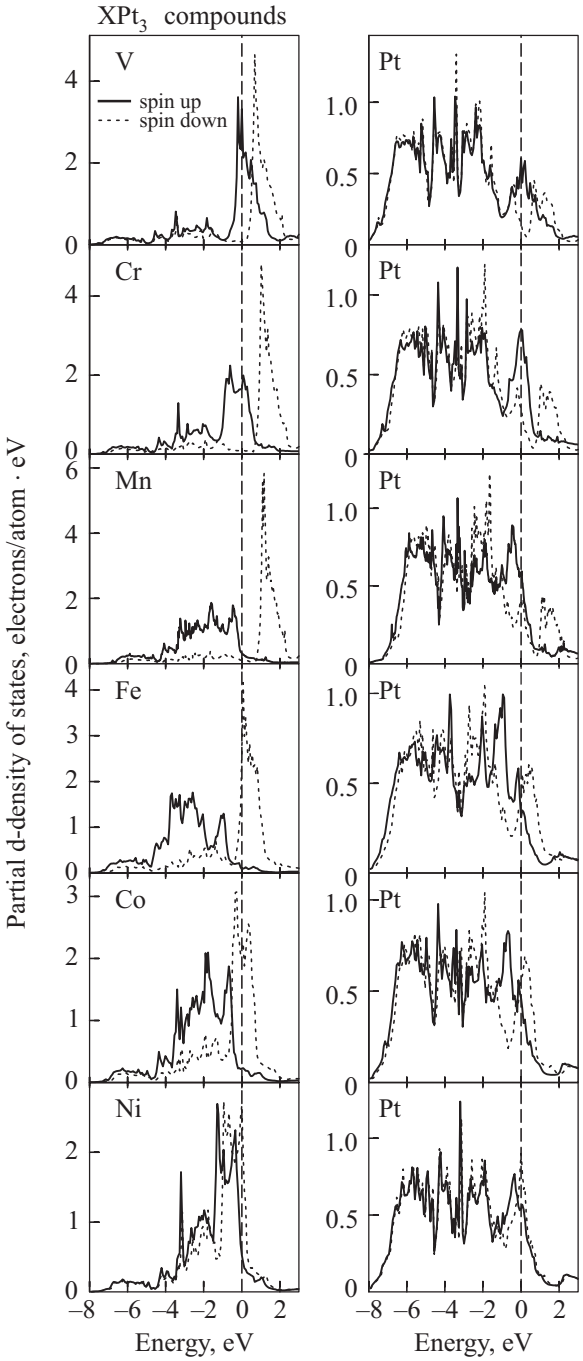

Fig. 4. Self-consistent fully relativistic, spin-polarized partial *d*-density of states of XPt_3 compounds (in electrons/atom· eV) [135].

stronger hybridization between the Pt *d* states and the empty 3*d* bands in $FePt_3$ and $CoPt_3$ (Fig. 4) the Pt spin moments are larger than in $MnPt_3$ where the largest 3*d* moment was found. The agreement between calculated spin magnetic moments at Pt sites and the experimentally derived moments is very good (Fig. 1,*a*.)

As can be seen from Fig. 1,*b* the variation in the orbital magnetic moments on the Pt sites observed by Maruyama et al. in XMCD experiments [129] is well reproduced by our calculations. However, the interpretation of the orbital moments is more complicated than in the case of the spin moments.

To illustrate the influence of the spin-orbit interaction on the initial and final states involved in the transitions let us introduce a site-dependent function $dm_{tl}(E)$ given by [139]

$$dm_{tl}(E) = \sum_{n\mathbf{k}} \langle \Psi_{tl}^{n\mathbf{k}} | \hat{l}_z | \Psi_{tl}^{n\mathbf{k}} \rangle \, \delta(E - E_{n\mathbf{k}}) \qquad (36)$$

where $\hat{l}_z$ is *z*-projection of the angular momentum operator, $E_{n\mathbf{k}}$ and $\Psi_{tl}^{n\mathbf{k}}$ are the energy of the *n*th band and the part of the corresponding LMTO wave function formed by the states with the angular momentum *l* inside the atomic sphere centered at the site *t*, respectively. In analogy to the *l*-projected density of states, $dm_{tl}(E)$ can be considered as the site- and *l*-projected density of the expectation value of $\hat{l}_z$. This quantity has purely relativistic origins and when the SO interaction is equal to zero $dm_{tl}(E) \equiv 0$. As van Vleck [140] showed for a free ion, the absence of orbital degeneracy is a sufficient condition for the quenching of the orbital moment, which means that the first-order contribution should vanish: $\langle \Psi_{\mathbf{k}} | \hat{l}_z | \Psi_{\mathbf{k}} \rangle = 0$. Thus, $dm_{tl}(E)$ can be considered as a measure of the SO interaction of the electronic states.

Furthermore, just as the number of states is defined as the integral of DOS, we can define the integral of $dm_{tl}(E)$

$$m_{tl}(E) = \int_{E_b}^{E} dm_{tl}(E)\, dE\,, \qquad (37)$$

where E_b is the bottom of the valence band. Then, the orbital moment M_l at the site *t* is given by:

$$M_l \equiv m_{tl}(E_F) \qquad (38)$$

(here and henceforth we will drop the index *t* for simplicity).

Both $dm_l(E)$ and $m_l(E)$ are defined in the local coordinate system chosen in such a way that *z* axis is directed along the magnetization. It is worth noting that the only nonzero matrix elements of the $\hat{l}_z$ operator calculated between real harmonics with $l = 2$ are $|\langle d_{x^2-y^2} | \hat{l}_z | d_{xy} \rangle| = 2$ and $|\langle d_{xz} | \hat{l}_z | d_{yz} \rangle| = 1$. Hence, the largest contribution to $m_l(E)$ can be expected from the $d_{x^2-y^2}$ and d_{xy} orbitals. The $m_l(E)$ function is proportional to the strength of the SO interaction and the value of the spin magnetic moment and it depends on the local symmetry. In the particular case of XPt_3 compounds the local symmetry for X atoms is O_h and for Pt atom it is D_{4h}. For the O_h group, basis functions are $E_g(d_{z^2}, d_{x^2-y^2})$, and T_{2g} (d_{xy}, d_{yz}, d_{xz}) while for the D_{4h} group they are A_{1g} (d_{z^2}), B_{1g} $(d_{x^2-y^2})$, B_{2g} (d_{xy}) and E_g (d_{yz}, d_{xz}). So the largest contribution to $m_l(E)$ can be expected in the case when we have simultaneously (at the same energy) a large contribution from the B_{1g} and B_{2g} states at Pt sites and the E_g and T_{2g} states at X sites in XPt_3 compounds.

Figure 5 shows the functions $dm_l(E)$ and $m_l(E)$ calculated for Co and Pt sites together with the partial d density of states in $CoPt_3$ as an example. Here and in the rest of the paper we will only consider the contribution coming from d orbitals to the m_l related functions. Both the $dm_l(E)$ and $m_l(E)$ functions show strong energy dependence. Although the variations of the functions at Co site are significantly larger in comparison with those at Pt sites, Pt and Co d orbital moments M_l are almost equal (see Fig. 3,*b* and Table 1).

When considering the $m_l(E)$ (Fig. 6) as well as $dm_l(E)$ (not shown) functions for XPt_3 compounds, one recognizes that especially those of $CrPt_3$, $MnPt_3$, $FePt_3$ and $CoPt_3$ are very similar for both the X and Pt sites, respectively. In going from $CrPt_3$ to $CoPt_3$ the Fermi level is simply shifted upwards by filling the bands with electrons. In $CrPt_3$ the Fermi level crosses $m_l(E)$ function at maximum and minimum at Cr and Pt sites, respectively producing rather large Cr and Pt orbital moments with opposite sign (Fig. 3,*b* and Table 1). In $MnPt_3$ due to filling the bands with one more electron, the Fermi level is situated at the local minimum in $m_l^{Mn}(E)$ and at zero crossing in $m_l^{Pt}(E)$. As a result $MnPt_3$ has a very small orbital magnetic moment at the Mn site and almost a zero Pt orbital moment. Further shifting of the Fermi level in $FePt_3$ places the Fermi level at a local maximum at both the Fe and Pt sites, providing rather large Fe and Pt orbital moments with the same sign. We should also mention that absolute magnitude deviation of the $m_l(E)$ function decreases at the beginning and end of the 3d row reflecting the decreasing of the spin magnetic moments in the compounds.

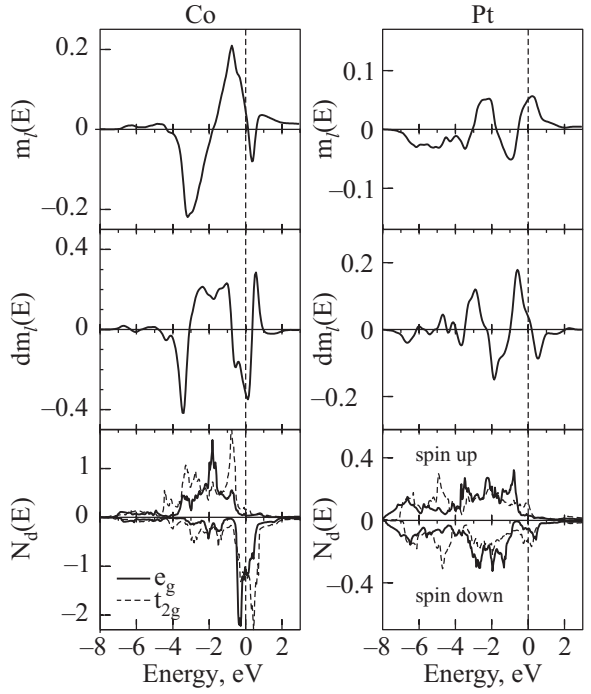

Fig. 5. The $dm_l(E)$, $m_l(E)$ functions and partial densities of states (in electrons/atom· eV· spin) for $l = 2$ in $CoPt_3$ [135].

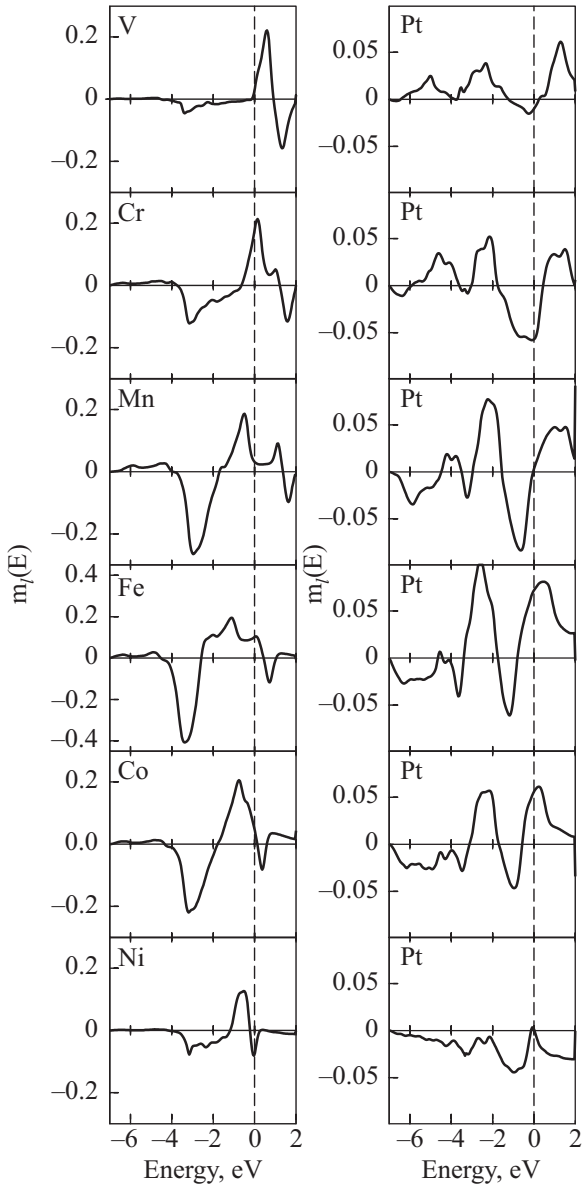

Fig. 6. The $m_l(E)$ functions for $l = 2$ in XPt_3 compounds [135].

It is interesting to compare the electronic structure and orbital magnetic moments in the XPt_3 and X_3Pt compounds. Figure 7 shows d partial density of states in $CoPt_3$ and Co_3Pt compounds at both the Co and Pt sites. In the $CoPt_3$ compound the transition metal site is surrounded by 12 Pt sites. On the other hand, in Co_3Pt, 4 of the nearest neighbors are Pt sites and the other 8 are Co sites. This difference in Co–Co coordination has a dramatic effect on the width of the 3d spin down DOS near the Fermi level. The 3d spin up states are centered more in the middle of the energy range of the Pt 5d states and therefore the Co orbitals hybridize rather effectively with the 5d orbitals in both the $CoPt_3$ and Co_3Pt compounds. On the other hand, 3d spin down states are centered in vicinity of the Fermi level where the Pt 5d DOS is rather

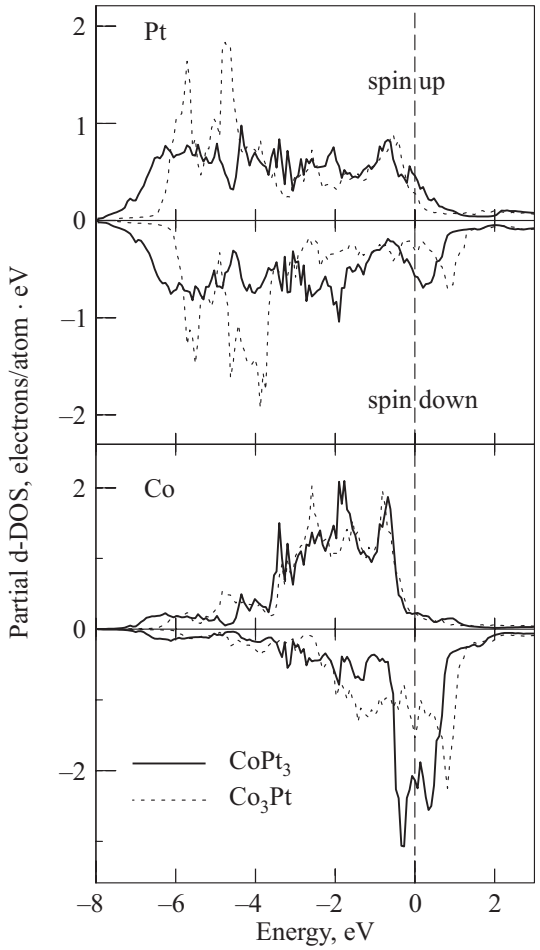

Fig. 7. Self-consistent fully relativistic, spin-polarized partial *d*-density of states of XPt_3 compounds (in electrons/atom· eV) [135].

small. As a result they have smaller $3d$–$5d$ hybridization. Thus the $3d$ spin down states are more localized in $CoPt_3$ and more itinerant in Co_3Pt.

2. XMCD spectra. At the core level edge XMCD is not only element-specific but also orbital specific. For $3d$ transition metals, the electronic states can be probed by the K, $L_{2,3}$ and $M_{2,3}$ x-ray absorption and emission spectra whereas in $5d$ transition metals one can use the K, $L_{2,3}$, $M_{2,3}$, $M_{4,5}$, $N_{2,3}$, $N_{4,5}$, $N_{6,7}$, and $O_{2,3}$ spectra. As pointed out above, Eq. (13) for unpolarized absorption spectra $\mu^0(\omega)$ allows only transitions with $\Delta l = \pm 1$, $\Delta j = 0, \pm 1$ (dipole selection rules). Therefore only electronic states with an appropriate symmetry contribute to the absorption and emission spectra under consideration (Table 2). We should mention that in some cases quadrupole transitions may play an important role, as it occurs, for example, in rare earth materials ($2p \to 4f$ transitions) [141].

3. *K edge of 3d transition metal elements.* Figure 8 shows the theoretically calculated K XMCD in XPt_3 (X = Mn, Fe, and Co) compounds. Because dipole allowed transitions dominate the absorption spectrum for unpolarized radiation, the absorption coefficient $\mu_K^0(E)$ (not shown) reflects primarily the DOS of unoccupied $4p$ like states $N_p(E)$ of X above the Fermi level. Due to the energy dependent radial matrix element for the $1s \to 4p$ there is no strict one-to-one correspondence between $\mu_K(E)$ and $N_p(E)$. The exchange splitting of the initial $1s$ core state is extremely small [142] therefore only the exchange and spin-orbit splitting of the final $4p$ states is responsible for the observed dichroism at the K edge. For this reason the dichroism is found to be very small (Fig. 8). It was first pointed out by Gotsis and Strange [107] as well as Brooks and Johansson [143] that XMCD K spectrum reflects the orbital polarization in differential form $d\langle l_z \rangle/dE$ of the p states. As Fig. 8 demonstrates, where K XMCD spectra is shown together with $dm_l(E)$ functions (Eq. (36)), both quantities are indeed closely related to one another giving a rather simple and straightforward interpretation of the XMCD spectra at the K edge.

Table 2. Angular momentum symmetry levels indicating the dipole allowed transitions from core states to the unoccupied valence states with the indicated partial density of states character.

Spectra	K	L_2 M_2 N_2 O_2	L_3 M_2 N_3 O_3	M_4 N_4	M_5 N_5	N_6	N_7
Core level	$1s_{1/2}$	$2p_{1/2}$ $3p_{1/2}$ $4p_{1/2}$ $5p_{1/2}$	$2p_{3/2}$ $3p_{3/2}$ $4p_{3/2}$ $5p_{3/2}$	$3d_{3/2}$ $4d_{3/2}$	$3d_{5/2}$ $4d_{5/2}$	$4f_{5/2}$	$4f_{7/2}$
Valence states	$p_{1/2}$ $p_{3/2}$	$s_{1/2}$ $d_{3/2}$	$s_{1/2}$ $d_{3/2}$ $d_{5/2}$	$p_{1/2}$ $p_{3/2}$ $f_{5/2}$	$p_{3/2}$ $f_{5/2}$ $f_{7/2}$	$d_{3/2}$ $d_{5/2}$ $g_{7/2}$	$d_{3/2}$ $g_{7/2}$ $g_{9/2}$

As in the case of absorption, K emission XMCD spectrum (not shown) is in close relationship with site- and l projected density of the expectation value of $\hat{l}_z$. Using the sum rule derived for K spectra in Ref. 110 we obtain a Mn $5p$ orbital magnetic moment of around $-0.0019\ \mu_B$ in a good agreement with LSDA calculations ($-0.0016\ \mu_B$).

4. $L_{2,3}$ and $M_{2,3}$ edges of 3d transition metal elements. Because of the dipole selection rules, apart from the $4s_{1/2}$ states (which have a small contribution to the XAS due to relatively small $2p \to 4s$ matrix elements [20]) only $3d_{3/2}$ states occur as final states for L_2 XAS for unpolarized radiation, whereas for the L_3 XAS $3d_{5/2}$ states also contribute (Table 2. Although the $2p_{3/2} \to 3d_{3/2}$ radial matrix elements are only slightly smaller than for the $2p_{3/2} \to 3d_{5/2}$ transitions the angular matrix elements strongly suppress the $2p_{3/2} \to 3d_{3/2}$ contribution (see Eq. (13)). Therefore in neglecting the energy

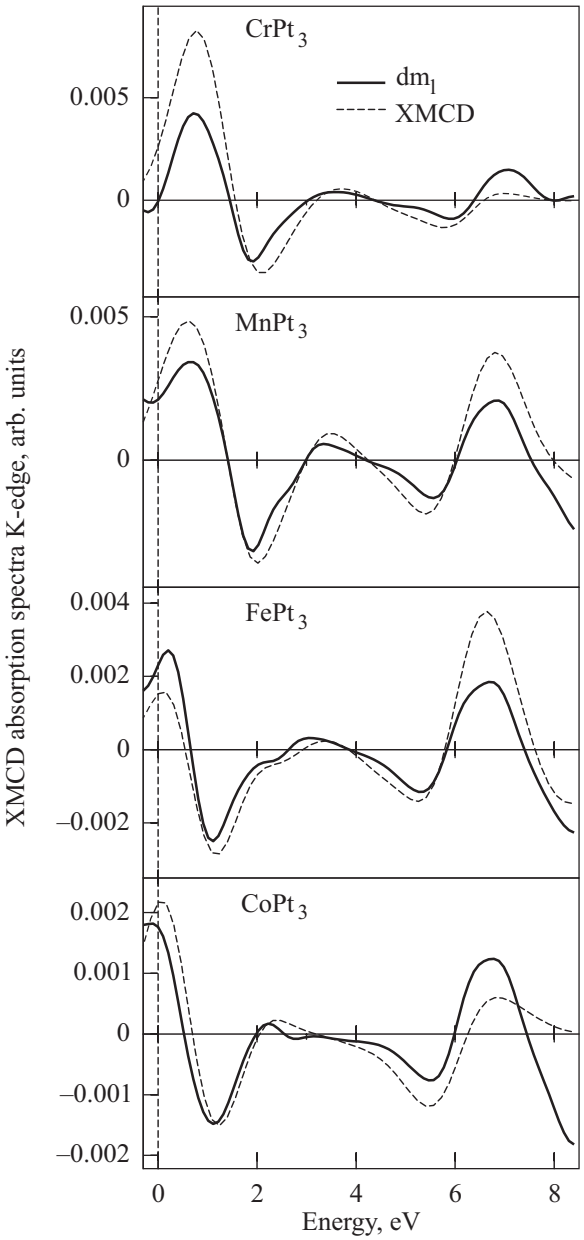

Fig. 8. Theoretically calculated 3*d* transition metal *K* XMCD absorption spectra in comparison with $dm_l(E)$ function in XPt_3 alloys [135].

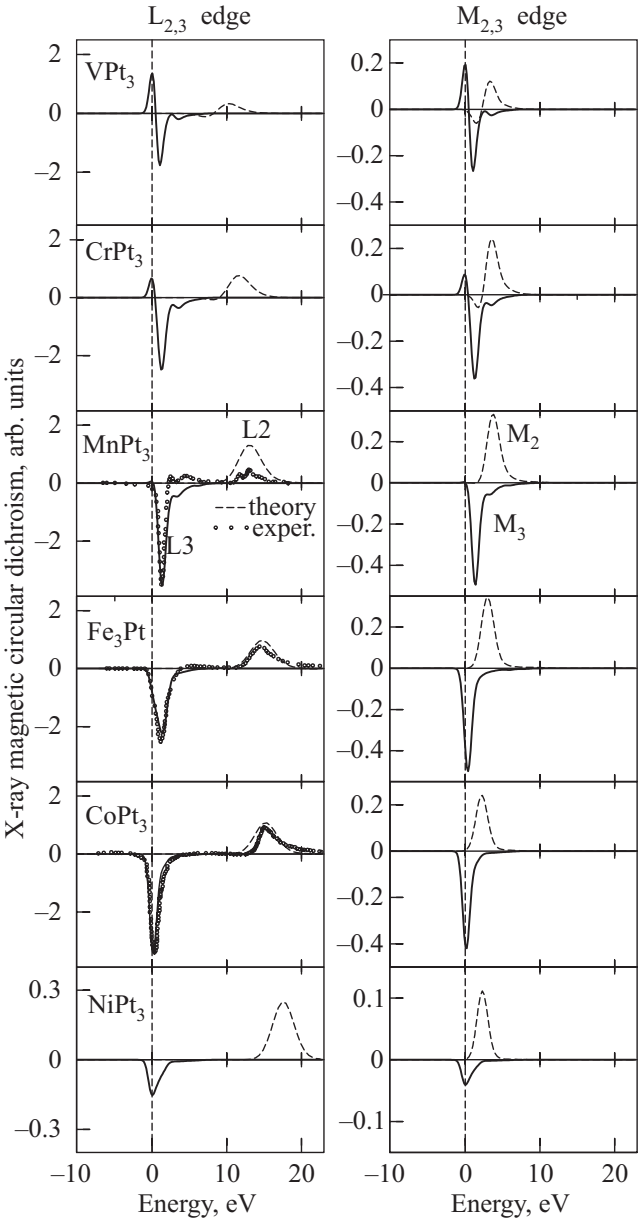

Fig. 9. Theoretically calculated 3*d* transition metal L_3 (full line), L_2 (dotted line) and M_3 (full line), M_2 (dotted line) XMCD spectra in XPt_3 alloys [135] in comparison with experimental data (circles) [130].

dependence of the radial matrix elements, the L_2 and L_3 spectra can be viewed as a direct mapping of the DOS curve for $3d_{3/2}$ and $3d_{5/2}$ character, respectively.

In contrast to the *K* edge, the dichroism at the L_2 and L_3 edges is also influenced by the spin-orbit coupling of the initial $2p$ core states. This gives rise to a very pronounced dichroism in comparison with the dichroism at the *K* edge. Figure 9 shows the theoretically calculated 3*d* transition metal $L_{2,3}$ XMCD spectra in XPt_3 alloys in comparison with the experimental data [130]. One finds that the theoretical XMCD spectra for the late transition metals to be in good agreement with experiment. For $MnPt_3$ the calculated magnetic dichroism is somewhat too high at the L_2 edge. As one can see, the XMCD spectra for Fe_3Pt, $CoPt_3$ and $NiPt_3$ are very similar with strong decreasing of the dichroism in $NiPt_3$ reflecting first of all the decrease of the spin magnetic moment in the later compound at the transition metal site (Table 1). The XMCD spectra of ferrimagnetic VPt_3 and $CrPt_3$ differ significantly at the L_3 edge from the spectra of the ferromagnetic compounds. The former spectra have an additional positive peak in the low energy region.

The XMCD spectra at the $L_{2,3}$ edges are mostly determined by the strength of the SO coupling of the initial $2p$ core states and spin-polarization of the final empty $3d_{3/2,5/2}$ states while the exchange splitting of the $2p$ core states as well as the SO coupling of the 3*d* valence states

are of minor importance for the XMCD at the $L_{2,3}$ edge of transition metals [20].

To investigate the influence of the initial state on the resulting XMCD spectra we calculated also the XAS and XMCD spectra of XPt_3 compounds at the $M_{2,3}$ edge. The spin-orbit splitting of the $3p$ core level is of one order of magnitude smaller (from about 0.73 eV in V to 2.2 eV in Ni) than for the $2p$ level (from 7.7 eV in V to 17.3 eV in Ni) at the X-site in the XPt_3 compounds. As a result the magnetic dichroism at the $M_{2,3}$ edge is much smaller than at the $L_{2,3}$ edge (Fig. 9). Besides the M_2 and the M_3 spectra are strongly overlapped and the M_3 spectrum contributes to some extent to the structure of the total $M_{2,3}$ spectrum in the region of the M_2 edge. To decompose a corresponding experimental $M_{2,3}$ spectrum into its M_2 and M_3 parts will therefore be quite difficult in general. It worth to mentioning that the shape of L_3 and M_3 XMCD spectra are very similar.

5. Pt $L_{2,3}$ *edges*. As mentioned above, XMCD investigations supply information on magnetic properties in a component resolved way. This seems especially interesting if there is a magnetic moment induced at a normally nonmagnetic element by neighboring magnetic atoms. The underlying mechanism of the magnetic and magneto-optical properties of the systems considered here is the well known ability of transition metals to induce large spin polarization of Pt via strong $3d-5d$ hybridization and exchange interaction. A very extreme example for this situation occurs for Pt in the XPt_3 compounds.

Results of the theoretical calculations for the circular dichroism at the $L_{2,3}$ edge of Pt are shown in Fig. 10 in comparison with the experimental data [128,129]. As one can see, a rather pronounced XMCD is found. In ferromagnetic compounds $MnPt_3$, Fe_3Pt, and $CoPt_3$, the XMCD spectrum is negative at the L_3 and positive at the L_2 edge as has been seen for the XMCD spectra at $L_{2,3}$ edges of the $3d$ transition metals (Fig. 9). The XMCD in $MnPt_3$ at the L_3 and L_2 edges are of nearly equal magnitude, which suggest that an orbital magnetic moment almost vanishes in the Pt $5d$ states in this compound [129]. In ferrimagnetically ordered VPt_3 and $CrPt_3$ the XMCD spectra at the L_3 edge are positive with a double peak structure in a good agreement with the experimental measurements [128]. The experimental XMCD spectrum of $CrPt_3$ at the Pt L_2 edge shows a positive sign although the theoretically calculated spectrum has additional negative components at both the low and high energy sides of the main peak (Fig. 10).

6. Pt M, N *and* O *edges*. To investigate the influence of the initial state on the resulting Pt XMCD spectra we calculated also the XAS and XMCD spectra of XPt_3 compounds at the $M_{2,3}$, $M_{4,5}$, $N_{2,3}$, $N_{4,5}$, $N_{6,7}$, and $O_{2,3}$ edges. We found a systematic decreasing of the XMCD spectra in terms of $R = \Delta\mu/(2\mu^0)$ in the row $L_{2,3} - M_{2,3} - N_{2,3}$ edges.

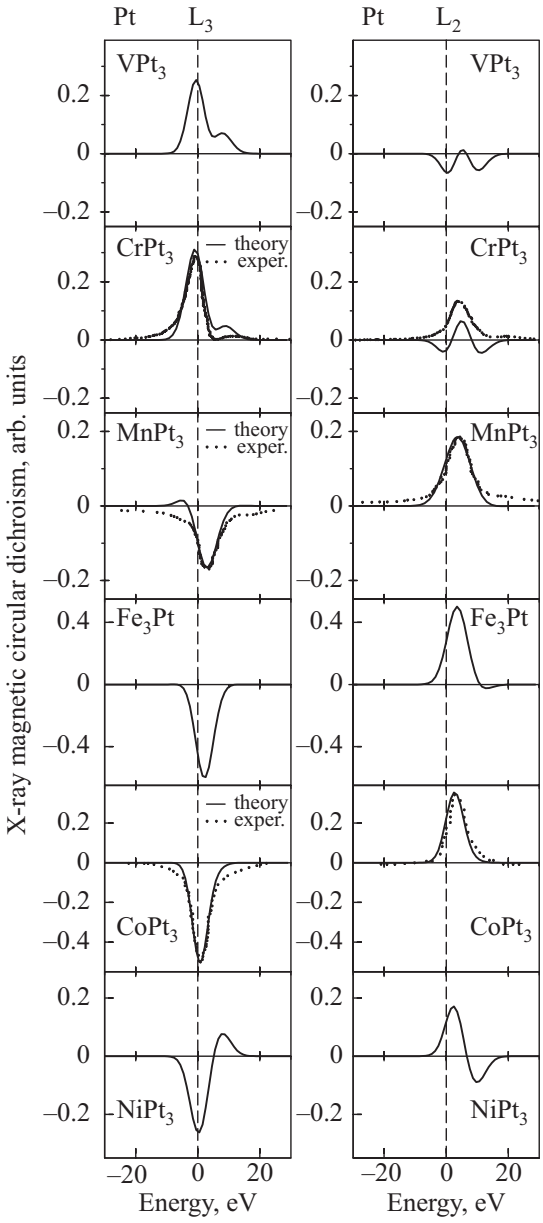

Fig. 10. Theoretically calculated Pt $L_{2,3}$ XMCD spectra in XPt_3 alloys (full line) [135] in comparison with the experiment (circles), the experimental data for $CrPt_3$ are from Ref. 128, $MnPt_3$ from Ref. 129, and $CoPt_3$ from Ref 132.

Although the magnetic dichroism at the $O_{2,3}$ and $N_{6,7}$ edges became almost as large as at the $L_{2,3}$ edge. Besides, the lifetime widths of the core $O_{2,3}$ and $N_{6,7}$ levels are much smaller than $L_{2,3}$ ones [144]. Therefore the spectroscopy of Pt atoms in the ultra-soft x-ray energy range at the $O_{2,3}$ and $N_{6,7}$ edges may be a very useful tool for investigating the electronic structure of magnetic materials.

Pt $M_{4,5}$ and $N_{4,5}$ spectra to some extent can be considered as an analog of the K spectrum. As it was mentioned above, K absorption spectrum at both sites reflects the energy distribution of empty $p_{1/2}$ and $p_{3/2}$ energy states (Table 2). The M_4 (N_4) absorption spectra due to the dipole selection rules occur for the transition

from the $3d_{3/2}$ ($4d_{3/2}$) core states to the $p_{1/2}$, $p_{3/2}$, and $f_{5/2}$ valence states above Fermi level, whereas for the M_5 (N_5) XAS the $p_{3/2}$, $f_{5/2}$, and $f_{7/2}$ states contributes. Results of the theoretical calculations of the circular dichroism in absorption at the $N_{4,5}$ edge of Pt in the XPt_3 (X = Cr, Mn and Fe) are shown in Fig. 11. Comparing this spectra with the corresponding XMCD spectra of transition metals at the K edge (Fig. 8) one can see an obvious resemblance between these two quantities (the magnetic dichroism at the N_4 edge has an opposite sign to the XMCD at the K and N_5 edge). Such a resemblance reflects the similarity of the energy distribution of unoccupied p local partial densities of states $N_p(E)$ just above the Fermi level at X and Pt sites (not shown). It occurs due to a strong X p–Pt p hybridization effect. The major difference is seen at 0 to 2 eV. It can be attributed to an additional contribution of the $f_{5/2,7/2}$ energy states to the $N_{4,5}$ spectra and to the difference in the radial matrix elements ($1s \to p_{1/2,3/2}$ in K spectra and $4d_{3/2,5/2} \to p_{1/2,3/2}$ in $N_{4,5}$ spectra). Although the later plays a minor role due to the fact that radial matrix elements are smooth functions of energy.

It is interesting to compare Pt XAS and XMCD spectra at the $L_{2,3}$, $O_{2,3}$ and $N_{6,7}$ edges. Due to the dipole selection rules, for unpolarized radiation (apart from the $s_{1/2}$ states which have a small contribution to the XAS) only $3d_{3/2}$ states occur as final states for L_2 as well as for O_2 spectra (Table 2). The L_3 and O_3 spectra reflect the energy distribution of both the $3d_{3/2}$ and $3d_{5/2}$ empty states. On the other hand, the N_7 absorption spectrum reflects only the $3d_{5/2}$ states (the density of the $g_{7/2,9/2}$ states is really very small) whereas for the N_6 XAS both the $3d_{3/2}$ and $3d_{5/2}$ states contribute. Therefore we have an inverse situation: N_6 absorption spectra correspond to the L_3 and O_3 spectra, whereas the N_7 is the analog of the L_2 and O_2 ones. This situation is clearly seen in Fig. 12 where the theoretically calculated XMCD spectra of XPt_3 compounds at the $O_{2,3}$ and $N_{6,7}$ edges is presented. The XMCD spectra at O_3 edges are almost identical to the spectra at the N_6 edges. The XMCD spectra at O_2 edges are also very similar to the spectra at the N_7 edges (but not identical because the energy distribution of Pt $3d_{3/2}$ and $3d_{3/2}$ states is not exactly the same due to SO interaction). The magnetic dichroism (e.g. in $CoPt_3$) is negative at the O_3 edge and positive at the O_2 edge (as it was at $L_{2,3}$ edges, see Fig. 10), but the XMCD is positive at the N_7 edge and negative at the N_6 one. However, we emphasize that O_3 (O_2) and N_6 (N_7) XMCD spectra are not identical to the L_3 (L_2) ones. One can argue that at least for Pt the $L_{2,3}$ spectra predominantly reflect atomic aspects of the valence band while for the $O_{2,3}$ and $N_{6,7}$ edge the itinerant aspects are more important. This is especially pronounced in ferrimagnetic VPt_3, $CrPt_3$ and ferromagnetic $MnPt_3$ with more itinerant character of the valence states than in $CoPt_3$ and $NiPt_3$ with relatively more localized $3d$ states.

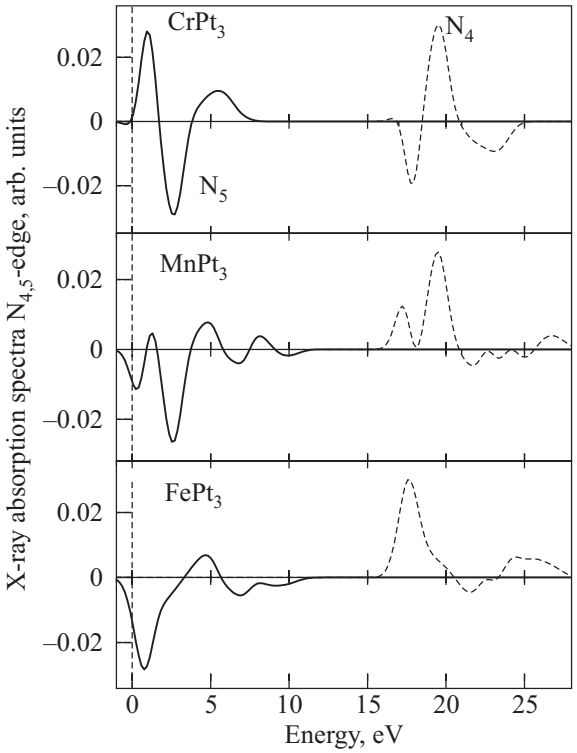

Fig. 11. Theoretically calculated Pt $N_{4,5}$ XMCD spectra in XPt_3 alloys [135].

Because of the relatively small spin-orbit splitting of the $4f$ states of Pt (~3.3 eV), the N_6 and the N_7 spectra have an appreciable overlap. For this reason the N_7 spectrum contributes to some extent to the structure of the total $N_{6,7}$ spectrum in the region of the N_6 edge, as can be seen from the Fig. 12. To decompose a corresponding experimental $N_{6,7}$ spectrum into its N_6 and N_7 parts will therefore be quite difficult in general.

Finally, we explored the anisotropy of the XMCD spectra with respect to the magnetization direction in these compounds. The influence of the direction of the magnetization on the XMCD spectra was found to be very small in XPt_3 compounds. The comparatively small dependence of the XMCD spectra on the magnetization direction is related to the high degree of isotropy inherent to the Cu_3Au structure.

7. XMCD sum rules. It is interesting to compare the spin and orbital magnetic moments obtained from the theoretically calculated XAS and XMCD spectra through the sum rules (Eqs. (15), (16)) with directly calculated LSDA values. In this case we at least avoid all the experimental problems.

Figure 13 shows direct and sum rule derived spin and orbital magnetic moments from the theoretical XMCD $L_{2,3}$ spectra. The general trend of the sum rule results is in a good agreement with the LSDA calculated spin and orbital magnetic moments for both the X and Pt sites. The

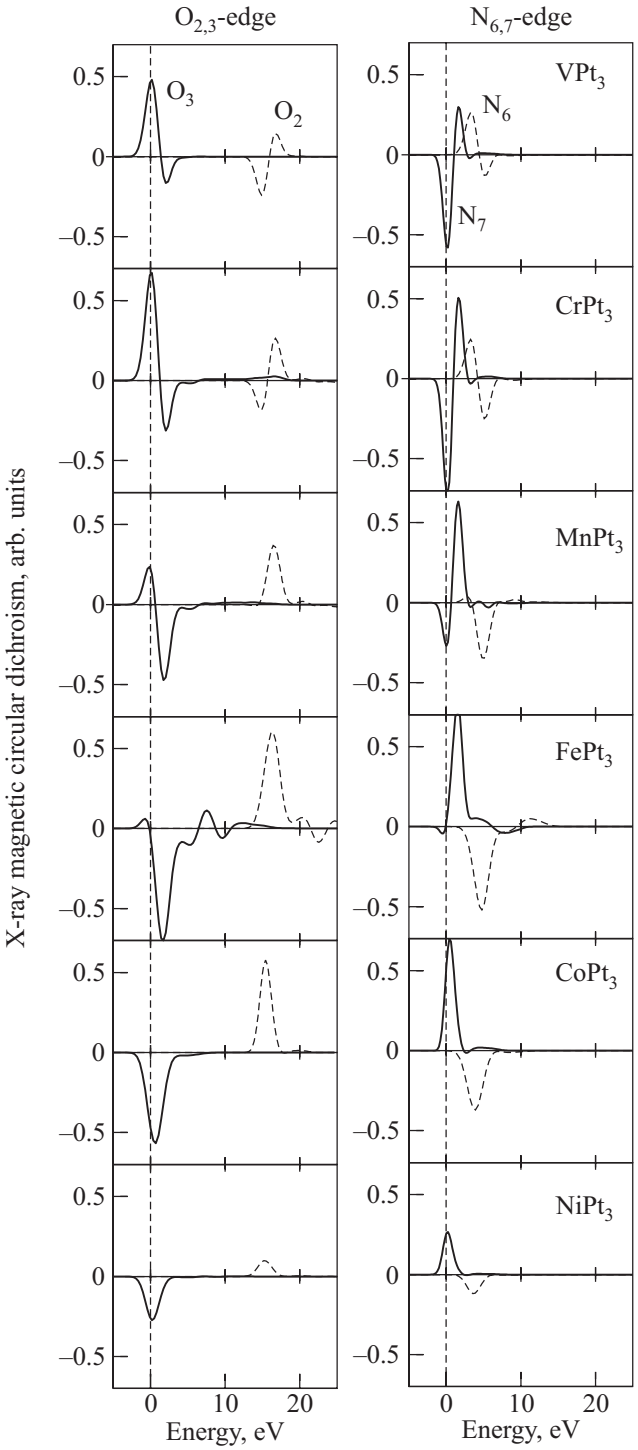

Fig. 12. Theoretically calculated Pt $O_{2,3}$ and $N_{6,7}$ XMCD spectra in XPt_3 alloys [135].

orbital magnetic moments at X and Pt sites agree well with the direct calculations, but the spin magnetic moments deduced from the theoretical XMCD spectra are underestimated for VPt_3, $CrPt_3$, and $MnPt_3$ for both the transition metal and Pt sites. The disagreement at X sites reaches the 40% in VPt_3 and reduces to 19% in $CrPt_3$, 15% in $MnPt_3$ and becomes less than 10% in Fe_3Pt, $CoPt_3$ and $NiPt_3$ compounds. Such behavior arises be-

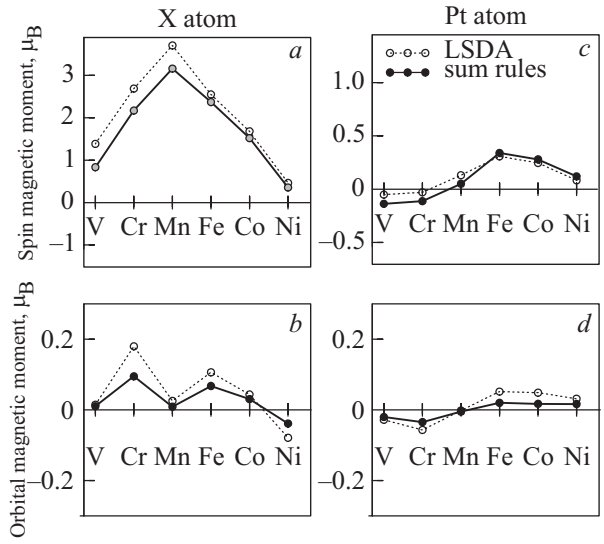

Fig. 13. Theoretically LSDA calculated spin (*a*), (*c*) and orbital (*b*), (*d*) magnetic moments at the X and Pt sites (open circles) in comparison with estimated data using the sum rules (solid circles) for XPt_3 and Fe_3Pt compounds [135].

cause the sum rules ignore the *p* transitions which play an essential role in the formation of the spin magnetic moments in early transition metals. In Fe, Co and Ni the relative contribution of the *s* states is reduced and the effect plays a minor role. Thus, first principles determinations of both the XMCD spectra and ground state properties (M_l and M_s) are probably required for quantitative interpretation of the experimental results.

4.2. Heusler compounds

4.2.1. Co_2MnGe. Electronic devices exploiting the spin of an electron have attracted great scientific interest [145]. The basic element is a ferromagnetic electrode providing a spin-polarized electric current. Materials with a complete spin-polarization at the Fermi level would be most desirable. The rapid development of magneto-electronics intensified the interest in such materials. Adding the spin degree of freedom to conventional electronic devices has several advantages such as the nonvolatility, the increased data processing speed, the decreased electric power consumption and the increased integration densities [145,146]. The current advances in new materials are promising for engineering new spintronic devices in the near future [146].

A metal for spin-up and a semiconductor for spin-down electrons is called half-metallic ferromagnet [147] (HMF) and Heusler compounds have been considered potential candidates to show this property [147]. The full Heusler alloys are defined as well-ordered ternary intermetallic compounds, at the stoichiometric composition X_2YZ, which have the cubic $L2_1$ structure. These compounds involve two different transition metal atoms *X* and *Y* and a third element *Z* which is a nonmagnetic

metal or nonmetallic element. Currently the Heusler alloys are at the focus of a large scientific interest due to their potential for applications in magnetic field sensors and spintronics devices [145]. Numerous theoretical and experimental studies of Heusler alloys have been carried out, and it has been shown that composition and heat treatment are important parameters determining their magnetic properties.

Co_2MnGe has a very high Curie temperature of about 905 K and a huge magnetization ($M \sim 5\mu_B$). The half-metalicity in the Co_2MnGe bulk compound was predicted for the first time in the pioneering Korringa–Kohn–Rostoker (KKR) calculations performed by Fujii et al. [148]. More recently, Ishida et al. [149] showed that the half-metallic character of Co_2MnGe strongly depends on the type of surface termination (Mn and Ge-terminated [001] surfaces are generally half metallic, Co-terminated ones are not), growth direction, and thickness of the film. Within this same framework, density-functional layer KKR simulations using the coherent potential approximation by Orgassa et al. [150,151] for the half-Heusler compound NiMnSb showed that atomic disorder (i.e., interchange of Ni and Mn or vacancies) leads to the disappearance of the half-metallic character. The Co antisite defect in Co_2MnGe were investigated in Ref. 152. It was found that half-metalicity could be lost because of defect-induced minority gap states. However, these states are efficiently screened out, as shown by the fast decay of the minority-spin charge density around E_F as a function of the distance from the defective site. The same authors extend their analysis by the investigation of the effects of several kind of defects such as swaps and antisites in both Co_2MnSi and Co_2MnGe hosts, in terms of formation energy and defect-induced electronic and magnetic properties [153]. They show that Mn antisites have the lowest formation energy and a retain half-metallic character. The effect of atomic disorder on the half-metalicity of similar Heusler alloys Co_2CrAl and Co_2FeAl has been investigated by Miura et al. [154,155]. They have shown that disorder between Cr and Al does not significantly reduce the spin polarization of Co_2CrAl, while disorder between Co and Cr causes a considerable reduction of the spin polarization. Block et al. [156] studied the effect of uniform strain and tetragonal distortion on the electronic and magnetic properties of the Heusler compounds Co_2CrAl and NiMnSb. They showed that the half-metallic character of the Heusler phases is lost with only a few percent uniform stress or tetragonal distortion of the lattice. The orbital magnetism in some half-metallic Heusler alloys including Co_2MnGe have been studied recently by Galanakis [157] using the fully relativistic screened KKR method. It was found that the calculated orbital magnetic moments are negligible compared with the spin moments.

X-ray magnetic circular dichroism in the ferromagnetic Co_2MnGe alloy has been measured at the Co and Mn $L_{2,3}$ edges [158,159]. Using the magneto-optical sum rules the orbital moments of Co and Mn have been deduced to be 0.07 and 0.03 μ_B, respectively.

1. Crystal structure. The Heusler-type X_2YZ compound crystallizes in the cubic $L2_1$ structure with $Fm\bar{3}m$ space group (No. 225). It is formed by four interpenetrating fcc sublattices as shown in Fig. 14. The X ions occupy the 8c Wyckoff positions ($x = 1/4$, $y = 1/4$, $z = 1/4$). The Y ions occupy the 4a positions ($x = 0$, $y = 0$, $z = 0$), and the Z ions are placed at the 4b sites ($x = 1/2$, $y = 1/2$, $z = 1/2$). All atoms have eight nearest neighbors at the same distance. The Y and Z atoms have eight X atoms as nearest neighbors, while for X there are four Y and four Z atoms.

2. Energy band structure. The total and partial DOS's of Co_2MnGe are presented in Fig. 15. The results agree well with previous band structure calculations [148,149,152,153]. The occupied part of the valence band can be subdivided into several regions. Ge 2s states appear between –12.0 and –9.9 eV. The states in the energy range –7.0 to 4.0 eV are formed by Co and Mn d states and Ge p states. Our calculations show that Co_2MnGe has a local magnetic moments of 0.956 μ_B on Co, 3.121 μ_B on Mn and –0.068 μ_B on Ge. The orbital moments are equal to 0.032 μ_B and 0.024 μ_B on the Co and Mn sites, respectively. The results are in good agreement with recent relativistic KKR calculations [157]. The interaction between the transition metals is ferromagnetic, leading to a total calculated moment of 4.964 μ_B.

The crystal field at the Co 8c site (T_d point symmetry) causes the splitting of d orbitals into a doublet e ($3z^2 - 1$ and $x^2 - y^2$) and a triplet t_2 (xy, yz, and xz). The crystal field at the Mn 4a site (O_h point symmetry) splits Mn d states into e_g ($3z^2 - 1$ and $x^2 - y^2$) and t_{2g} (xy, yz, and xz) states. The hybridization between Mn and Co d states plays an important role in the formation of the band structure of Co_2MnGe.

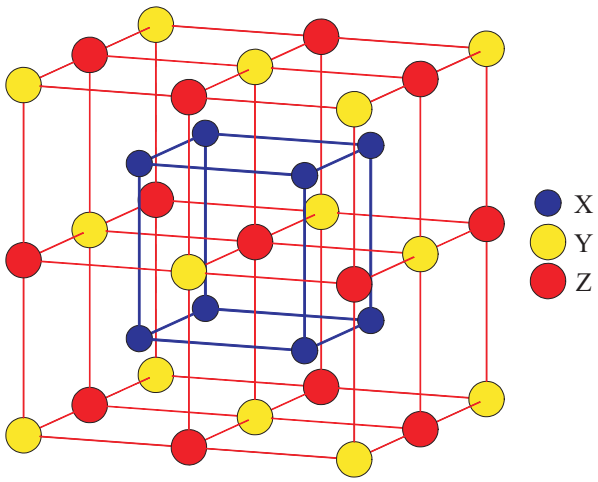

Fig. 14. Schematic representation of the $L2_1$ structure. The cubic cell contains four primitive cells.

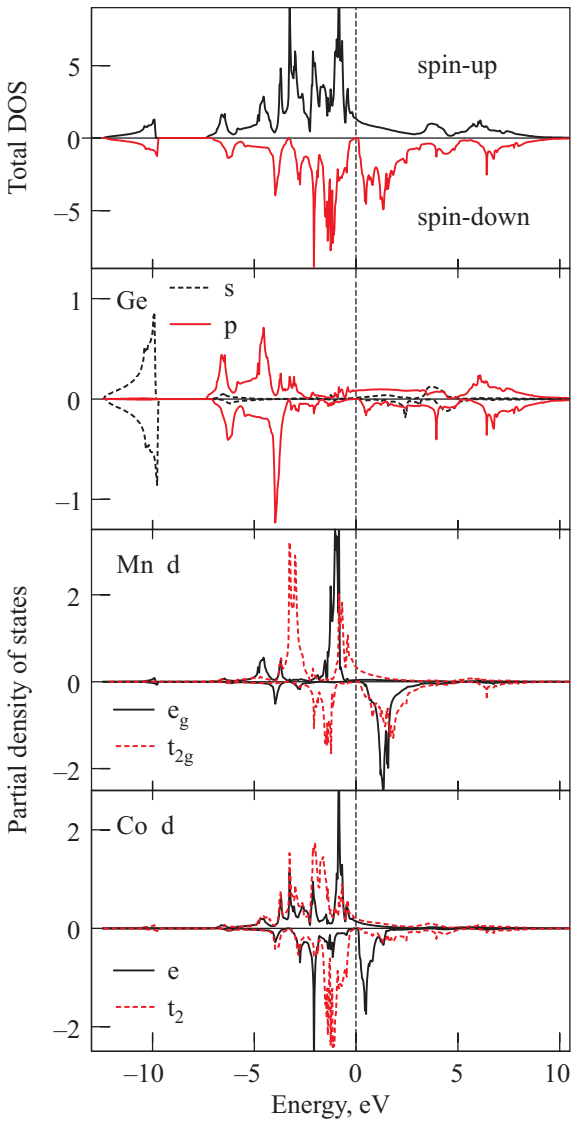

Fig. 15. The total (in states/(cell·eV)) and partial (in states/(atom·eV)) density of states of Co_2MnGe [160]. The Fermi energy is at zero.

It leads to the splitting of the *d* states into the bonding states which have Co and Mn *d* character and antibonding states with stronger contribution of Mn *d* states.

Without the spin-orbit coupling the strong hybridization between the minority spin Mn *d* and Co *d* states leads to the opening of a gap of 0.1 eV. Thus, according to the spin-polarized calculations Co_2MnGe is a half-metallic ferromagnet. Although spin-orbit splitting of the *d* energy bands for both the Co and Mn atoms is much smaller than their spin and crystal-field splittings this interaction closes the energy gap for the minority spin states. The Fermi level falls in a region of very low but finite minority-spin DOS. The spin polarization of the electron states at the Fermi energy is equal to 95%. Similar results for some other Heusler alloys were obtained in Refs. 161,162 where it was shown that the spin-orbit interaction can result in a nonvanishing density of states in the minority-spin gap of the half metals around the Fermi level, which reduces the spin polarization at E_F.

3. XMCD spectra. Recently x-ray magnetic circular dichroism in the ferromagnetic Co_2MnGe alloy has been measured at the Co and Mn $L_{2,3}$ edges [158,159]. The experimentally measured dichroic lines have different signs at the L_3 and L_2 edges of Co and Mn [159].

Figure 16 shows the XAS and XMCD spectra at the $L_{2,3}$ edges of Co calculated in the LSDA approach together with the experimental data [159]. The corresponding spectra for Mn are presented in Fig. 17. The contribution from the background scattering is shown by dotted line in the upper panel of Figs. 16 and 17.

Because of the dipole selection rules, apart from the $4s_{1/2}$ states (which have a small contribution to the XAS due to relatively small $2p \to 4s$ matrix elements) only $3d_{3/2}$ states occur as final states for L_2 XAS for unpolarized radiation, whereas for the L_3 XAS the $3d_{5/2}$ states also contribute [22]. Although the $2p_{3/2} \to 3d_{3/2}$ radial matrix elements are only slightly smaller than for the $2p_{3/2} \to 3d_{5/2}$ transitions the angular matrix elements strongly suppress the $2p_{3/2} \to 3d_{3/2}$ contribution [22]. Therefore neglecting the energy dependence of the radial matrix elements, the L_2 and the L_3 spectrum can be viewed as a direct mapping of the DOS curve for $3d_{3/2}$ and $3d_{5/2}$ character, respectively.

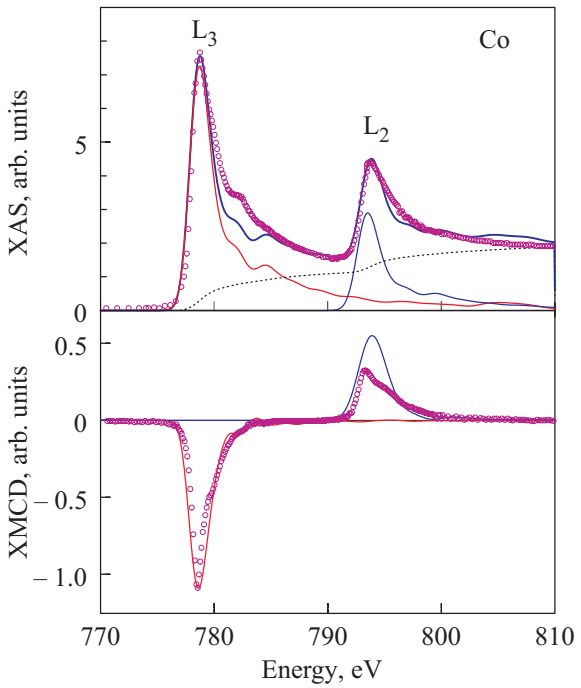

Fig. 16. Upper panel: calculated (thin full line) and experimental (circles) x-ray absorption spectra for the right polarized x-rays μ^- of Co_2MnGe at the Co $L_{2,3}$ edges. Experimental spectra (see Ref. 159) were measured by mean of total photoelectron yield with external magnetic field (1.4 T). Dotted lines show the theoretically calculated background spectra, full thick lines are sum of the theoretical XAS and background spectra. Low panel: theoretically calculated (full lines) and experimental (circles) XMCD spectra of Co_2MnGe at the Co $L_{2,3}$ edges [160].

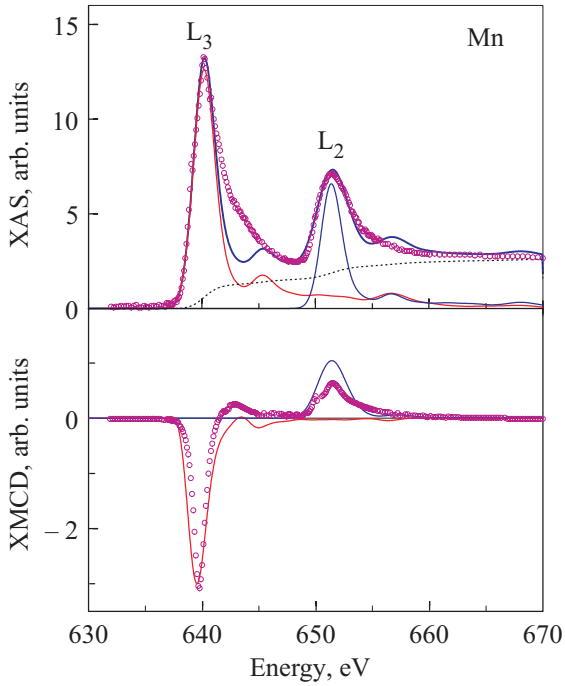

Fig. 17. Upper panel: calculated (thin full line) and experimental (circles) x-ray absorption spectra for the right polarized x-rays μ^- of Co_2MnGe at the Mn $L_{2,3}$ edges. Experimental spectra (see Ref. 159) were measured by mean of total photoelectron yield with external magnetic field (1.4 T). Dotted lines show the theoretically calculated background spectra, full thick lines are sum of the theoretical XAS and background spectra. Low panel: theoretically calculated (full lines) and experimental (circles) XMCD spectra of Co_2MnGe at the Mn $L_{2,3}$ edges [160].

The experimental Co XAS has a pronounced shoulder at the L_3 peak at around 782 eV shifted by about 3 eV with respect to the maximum to higher photon energy. This structure is less pronounced at the L_2 edge. This result can be ascribed to the lifetime broadening effect because the lifetime of the $2p_{1/2}$ core hole is shorter than the $2p_{3/2}$ core hole due to the L_2L_3V Coster-Kronig decay. This feature is partly due to the interband transitions from $2p$ core level to $3d$ empty states at around 4 eV. Actually as can be seen from Fig. 18 Co d partial DOS's have two pronounced peaks at 4 eV and 6.5 eV above the Fermi level. Both the features are reflected in the theoretically calculated XAS at the Co L_3 edge around 782 and 784.5 eV, respectively (Fig. 16). Although the second peak is less pronounced in the experimental spectrum.

Figure 17 presents the calculated XAS as well as XMCD spectra of the Co_2MnGe compound at the Mn $L_{2,3}$ edges compared with the experimental data [159]. The first peak in the empty Mn d partial DOS's at 4 eV above the Fermi level is less intensive in comparison with the corresponding peak in the Co d PDOS (see Fig. 18), therefore the theoretically calculated XAS has only one pronounced feature at the high energy part of the XAS at around 645 eV (Fig. 17).

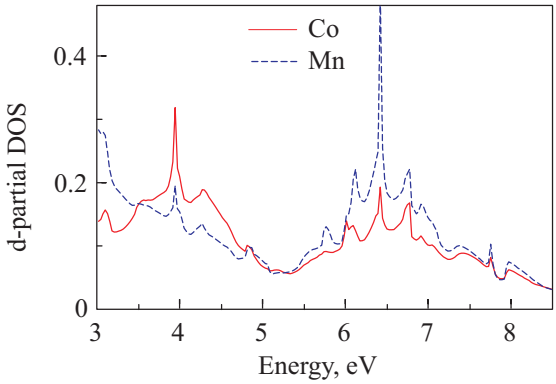

Fig. 18. The Co and Mn d-partial density of unoccupied states (in states/(atom·eV)) of Co_2MnGe [160]. Energies are relative to the Fermi energy.

It may be seen in the upper part of Fig. 16 that the experimentally measured Co L_3 XAS has some additional intensity around 782 eV which is not completely reproduced by the theoretical calculations. A similar situation also appear in the Mn L_3 XAS (Fig. 17) where the theoretical one-particle calculations does not reproduce all the intensity at around 643 eV. This might indicate that additional satellite structures may appear due to many-body effects at the high energy tails of both the Co and Mn $L_{2,3}$ XAS's. This question needs additional theoretical investigation using an appropriate many-body treatment.

The XMCD spectra at the $L_{2,3}$ edges are mostly determined by the strength of the SO coupling of the initial $2p$ core states and spin-polarization of the final empty $3d_{3/2,5/2}$ states while the exchange splitting of the $2p$ core states as well as the SO coupling of the $3d$ valence states are of minor importance for the XMCD at the $L_{2,3}$ edge of $3d$ transition metals [22].

4. Magnetic moments. In magnets, the atomic spin M_s and orbital M_l magnetic moments are basic quantities and their separate determination is therefore important. Methods of their experimental determination include traditional gyromagnetic ratio measurements [163], magnetic form factor measurements using neutron scattering [164], and magnetic x-ray scattering [165]. In addition to these, the recently developed x-ray magnetic circular dichroism combined with several sum rules [49–52] has attracted much attention as a method of site- and symmetry-selective determination of M_s and M_l.

Because of the significant implications of the sum rules, numerous experimental and theoretical studies aimed at investigating their validity for itinerant magnetic systems have been reported, but with widely different conclusions. The claimed adequacy of the sum rules varies from very good (within 5% agreement) to very poor (up to 50% discrepancy) [22]. This lack of a consensus may have several origins. For example, on the theoretical side, it has been demonstrated by circularly polarized $2p$ resonant photoemission measure-

ments of Ni that both the band structure effects and electron-electron correlations are needed to satisfactorily account for the observed MCD spectra [166]. However, it is extremely difficult to include both of them in a single theoretical framework. Besides, the XAS as well as XMCD spectra can be strongly affected (especially for the early transition metals) by the interaction of the excited electron with the created core hole [167,168].

On the experimental side, the indirect x-ray absorption techniques, i.e., the total electron and fluorescence yield methods, are known to suffer from saturation and self-absorption effects that are very difficult to correct for [100]. The total electron yield method can be sensitive to the varying applied magnetic field, changing the electron detecting efficiency, or, equivalently, the sample photocurrent. The fluorescence yield method is insensitive to the applied field, but the yield is intrinsically not proportional to the absorption cross section, because the radiative to non-radiative relative core-hole decay probability depends strongly on the symmetry and spin polarization of the XAS final states [169].

The Mn L_3 and the L_2 spectra in Co_2MnGe are strongly overlapped therefore the decomposition of a corresponding experimental $L_{2,3}$ spectrum into its L_3 and L_2 parts is quite difficult and can lead to a significant error in the estimation of the magnetic moments using the sum rules (the integration $\int_{L_3}$ and $\int_{L_2}$ in Eq. (16) must be taken over the $2p_{3/2}$ and $2p_{1/2}$ absorption regions separately). Besides, the experimentally measured Co and Mn $L_{2,3}$ x-ray absorption spectra have background scattering intensity and the integration of the corresponding XASs may lead to an additional error in the estimation of the magnetic moments using the sum rules.

It is interesting to compare the spin and orbital moments obtained from the theoretically calculated XAS and XMCD spectra through sum rules [Eqs. (15), (16)] with directly calculated LSDA values in order to avoid additional experimental problems. The number of the transition metal 3*d* electrons is calculated by integrating the occupied *d* partial density of states inside the corresponding atomic sphere which gives the values averaged for the nonequivalent sites $n_{Co} = 7.786$ and $n_{Mn} = 5.682$. Sum rules reproduce the spin magnetic moments within 29%, and 23% and the orbital moments within 41% and 54% for Co and Mn, respectively (Table 3). XMCD sum rules are derived within an ionic model using a number of approximations. For $L_{2,3}$, they are [20]: (1) ignoring the exchange splitting of the core levels; (2) replacing the interaction operator $\boldsymbol{\alpha}\cdot\mathbf{a}_l$ in Eq. (11) by $\boldsymbol{\nabla}\cdot\mathbf{a}_\lambda$; (3) ignoring the asphericity of the core states; (4) ignoring the difference of $d_{3/2}$ and $d_{5/2}$ radial wave functions; (5) ignoring $p \to s$ transitions; (6) ignoring the energy dependence of the radial matrix elements. To investigate the influence of the last point we applied the sum rules to the XMCD spectra neglecting the energy dependence of the radial matrix elements. As can be seen from Table 3 using the energy independent radial matrix elements reduces the disagreement in spin magnetic moments to 3% and 2% and in the orbital moment to 3% and 4% for Co and Mn, respectively. Additionally the omitting of the $p \to s$ transitions leads to almost perfect agreement between LSDA and sum rule results within 1% for the spin moments and 0% for the orbital moments. These results show that the energy dependence of the matrix elements and the presence of $p \to s$ transitions affect strongly the values of both the spin and the orbital magnetic moments derived from the sum rules.

Table 3. The experimental and calculated spin M_s and orbital M_l magnetic moments (in μ_B) of Co_2MnGe.

Method	Atom	M_s	M_l
LSDA	Ge	–0.068	0.001
	Co	0.956	0.032
	Mn	3.121	0.024
Sum rules	Co	0.681	0.019
	Mn	2.412	0.011
Sum rules[a]	Co	0.925	0.031
	Mn	3.060	0.023
Sum rules[b]	Co	0.944	0.032
	Mn	3.101	0.024
LSDA + U	Co	0.989	0.041
	Mn	3.049	0.031
Expt.[c]	Co	1.04	0.07
	Mn	3.17	0.03

Comment: [a]Sum rules applied for the XMCD spectra calculated ignoring the energy dependence of the radial matrix elements.
[b]Sum rules applied for the XMCD spectra calculated ignoring the energy dependence of the radial matrix elements and ignoring $p \to s$ transitions.
[c]Reference 159.

The value of the orbital magnetic moments derived from the experimental XMCD spectra is considerably higher in comparison with our band structure calculations (Table 3). It is a well-known fact, however, that LSDA calculations are inaccurate in describing orbital magnetism [20,22]. In the LSDA, the Kohn-Sham equation is described by a local potential which depends on the electron spin density. The orbital current, which is responsible for M_l, is, however, not included in the equations. This means, that although M_s is self-consistently determined in the LSDA, there is no framework to determine simultaneously M_l self-consistently. Numerous attempts have been made to better estimate M_l in solids. They can be roughly classified into two categories. One is based on

the so-called current density functional theory [170–172] which is intended to extend density functional theory to include the orbital current as an extra degree of freedom, which describes M_l. Unfortunately an explicit form of the current density functional is at present unknown. The other category includes orbital polarization [173–176], self-interaction correction, [177] and LSDA + U [59,60] approaches.

To calculate M_l beyond the LSDA scheme we used the rotationally invariant LSDA + U method [60] using a double-counting correction term in the fully-localized limit approximation [178.179]. We used $U = J = 1.0$ eV for the transition metal sites. In this case $U_{\text{eff}} = U - J = 0$ and the effect of the LSDA + U comes from non-spherical terms which are determined by F^2 and F^4 Slater integrals. This approach is similar to the orbital polarization corrections mentioned above [22]. The LSDA + U calculations produce orbital magnetic moments equal to 0.041 μ_B and 0.031 μ_B for Co and Mn sites, respectively. The Co LSDA + U orbital moment is somewhat smaller than the experimental estimates, however, the value for Mn is in perfect agreement with the experimental data. We should mention that the shape of the XMCD spectra in Co_2MnGe is less sensitive to the orbital polarization correction in comparison with the evaluated orbital magnetic moments. The XAS and XMCD spectra calculated in LSDA and LSDA + U approximations have almost identical shape.

4.2.2. Co_2NbSn. Ferromagnetic shape-memory alloys displaying large magnetic-field-induced strain have recently emerged as a new class of active materials, very promising for actuator and sensor applications. The interest in ferromagnetic shape memory compounds stems from the possibility of controlling the phase transition by application of a magnetic field [180]. The response of the system to a field is potentially faster than that obtained by changing temperature or applying stress, thus substantially increasing the range of applications. Ni_2MnGa is the only known ferromagnetic material exhibiting a martensitic transition from a high-temperature Heusler structure to a related tetragonal form [18] with a 6.6% c axis contraction at $T_s = 200$ K. Associated with this phase transition the material exhibits shape memory properties enabling the system to reverse large deformations in the martensitic phase by heating into the cubic phase.

Co_2NbSn is also reported to belong to the group of ferromagnetic shape memory Heusler alloys. However, unlike Ni_2MnGa, for which the martensitic phase transition (T_s = 200 K) occurs within the ferromagnetically ordered phase (T_c = 376 K), for Co_2NbSn the martensitic phase transition temperature T_s = 233 K is well above the ferromagnetic ordering temperature of T_c = 116 K [182]. Consequently the shape memory behavior in Co_2NbSn cannot be controlled by a magnetic field.

A striking feature of Co_2NbSn is the very strong sample dependence of its physical properties. Sample-to-sample variations of transition temperatures by 20 K (T_c) and 50 K (T_s) are observed [183–185]. Moreover, a resistivity ratio $\rho_{300K}/\rho_{4.2K} = 1$ and a negative temperature derivative $d\rho/dT$ over a wide temperature range are observed. This is in conflict with a fairly large density of states at the Fermi level, as derived from the electronic specific heat coefficient [184,185]. Further, at the first-order transition, T_s, the accompanying specific heat anomaly is smeared out over a wide temperature range of 60 K. Such behavior points to the presence of crystallographic disorder, which has been identified recently by means of a detailed microscopic study of the local crystallographic site symmetry in Ref. 182. Co_2NbSn is disordered on an atomic scale, i.e., there are random displacements of Co, Nb and Sn ions from their nominal positions in both the *Fm*3*m* and *Pmma* lattices.

The band structure calculations of Ni_2MnGa and Co_2NbSn both in the cubic and tetragonal phases were carried out in early work of Fujii et al. [186] using the KKR method. The structural transition in these compounds has been proposed as being driven by a band Jahn–Teller effect, i.e., an energy gain is provided by the lifting of the degeneracy of electron bands. One should mention that although the energy band structure of the low temperature phase of Co_2NbSn was evaluated in Ref. 186 as tetragonal, recent structural investigations [182] shows that the low temperature phase of this compound has orthorhombic *Pmma* symmetry.

The study of the magnetic and structural phase transitions of the pseudo-ternary Heusler series $(Co_{1-x}Ni_x)_2NbSn$ (x = = 0, 0.18, 0.56, 0.81, and 1) are presented in Ref. 187. Upon alloying Co_2NbSn with Ni, both the structural and the magnetic phase transition temperatures are suppressed to zero temperature with Ni content at x = 0.32 (T_c) and 0.47 (T_s). This might indicate a very strong interlocking of the two phenomena. Moreover, if such a coincidence of a first- and second-order phase transition occurs, it might be interesting in the context of quantum phase transitions. For instance, for MnSi a second-order phase transition is replaced by a first-order transition upon approaching the quantum critical point [188]. Authors of Ref. 187 have also presented arguments for the disorder to control the unusual magnetic domain behavior, i.e., the formation of very narrow domain walls occurring in an itinerant magnet.

Recently x-ray magnetic circular dichroism in the ferromagnet Co_2NbSn has been measured at the Co $L_{2,3}$ edges [189]. Using the magneto-optic sum rules the spin moment and the orbital moment of Co have been deduced to be 0.38, and 0.09 μ_B, , respectively.

1. Crystal structure. The Heusler-type Co_2NbSn compound crystallized at high temperatures in the cubic $L2_1$ structure with *Fm*3*m* symmetry (No. 225) is formed by

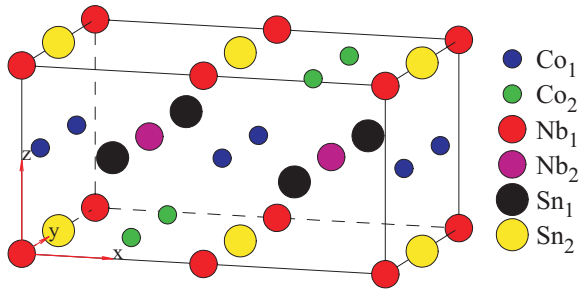

Fig. 19. The orthorhombic low-temperature lattice structure of Co_2NbSn with space group *Pmma* (No. 51).

four interpenetrating fcc sublattices. The Co ions occupy the 4*b* Wyckoff positions ($x = 1/4$, $y = 1/4$, $z = 1/4$). The Nb ions occupy the 4*a* positions ($x = 0$, $y = 0$, $z = 0$) and the Sn ions are placed at the 4*b* sites ($x = 1/2$, $y = 1/2$, $z = 1/2$). Both the Co and Nb atoms have eight nearest neighbors at the same distance. Nb has eight Co atoms as nearest neighbors, while for Co there are four Nb and four Sn atoms (Table 4).

Co_2NbSn undergoes a structural transition at T_s 233 K from the cubic Heusler *Fm*3*m* high-temperature phase into a simple orthorhombic low-temperature lattice of *Pmma* symmetry (No. 51) [182]. Two inequivalent Co ions occupy the 4*h* ($x = 0$, $y = 0.253$, $z = 1/2$) and 4*k* ($x = 1/4$, $y = 0.746$, $z = 0.051$) Wyckoff positions. The Nb ions occupy also two inequivalent Wyckoff positions 2*a* ($x = 0$, $y = 0$, $z = 0$) and 2*f* ($x = 1/4$, $y = 1/2$, $z = 0.527$). Sn ions are placed at the 2*e* ($x = 1/4$, $y = 0$, $z = 0.537$) and 2*b* ($x = 0$, $y = 1/2$, $z = 0$) [182] sites. (Fig. 19). In the following we will refer to Co_1, Co_2, Nb_1, Nb_2, Sn_1, and Sn_2 as situated at the 4*h*, 4*k*, 2*a*, 2*f*, 2*e*, and 2*b* sites, respectively. The structural transition gives rise to a large variation of interatomic distances up to 4%, compared to the cubic lattice (Table 4). In contrast, the volume of the unit cell remains almost constant over the whole temperature range.

While on a macro- and mesoscopic scale Co_2NbSn appears to be fully ordered, from microscopic Mössbauer and NMR studies it was found that on an atomic scale site disorder is present in form of random displacements of Co, Nb and Sn ions from their nominal positions in both the *Fm*3*m* and *Pmma* lattices [182].

The energy band structure and total DOS of Co_2NbSn for the high temperature *Fm*3*m* structure obtained from fully relativistic LDA calculations are presented in Fig. 20. The results agree well with previous band structure calculations [186]. The occupied part of the valence band can be subdivided into several regions. The tin 2*s* bands appear between –11.4 and –9.0 eV. The next three energy bands in the energy region –6.9 to –3.1 eV are the tin 5*p* bands. The Co and Nb *d* energy bands are located above and below E_F at about –3.1 to 2.0 eV. The corresponding spin-polarized partial densities of states are shown in Fig. 21.

Table 4. Number and distance of the nearest neighbors for different type of atoms in the high (*Fm*3*m*) and low (*Pmma*) phases of Co_2NbSn (in arb. unuts).

*Fm*3*m*			*Pmma*		
Atom	Neighbors	Distance	Atom	Neighbors	Distance
Co	4× Sn	5.034	Co_1	2× Sn_2	5.026
				2× Sn_1	5.039
			Co_2	1× Sn_1	4.973
				2× Sn_2	5.004
				1× Sn_1	5.167
	4× Nb	5.034	Co_1	2× Nb_2	4.997
				2× Nb_1	5.063
			Co_2	1× Nb_21	4.853
				2× Nb_12	5.054
				1× Nb_21	5.189
	6× Co	5.813	Co_1	1× Co_1	5.533
				2× Co_1	5.610
				1× Co_1	5.667
				2× Co_1	6.217
			Co_2	1× Co_2	5.511
				1× Co_2	5.690
Nb	8× Co	5.034	Nb_1	4× Co_2	5.052
				4× Co_1	5.063
			Nb_2	2× Co_2	4.853
				4× Co_1	4.997
				2× Co_2	5.189

Because of strong Sn *p*–*p* hybridization Sn *p* states are split into bonding and antibonding states. The former are located between approximately –7 and –2 eV, while

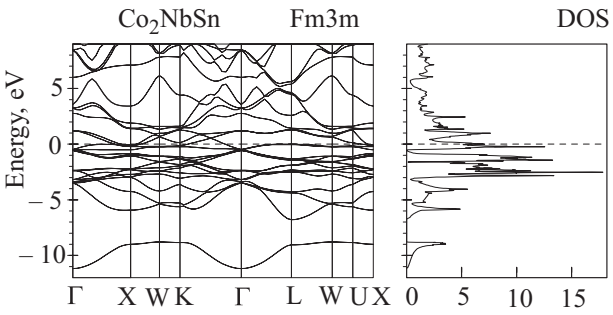

Fig. 20. The fully relativistic LDA energy band structure and total DOS (in states/(cell·eV)) of Co_2NbSn for the high temperature *Fm*3*m* structure [190].

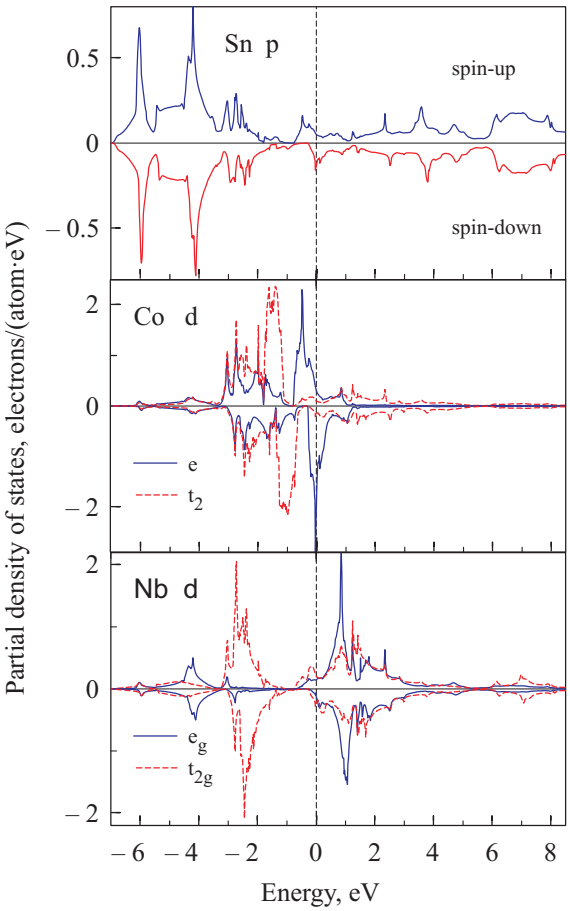

Fig. 21. The symmetry separated partial density of states of Co_2NbSn for the high temperature *Fm*3*m* structure [190].

the latter are spread over a broad energy range above –1 eV. The center of Nb *d* states, defined as the energy at which the corresponding logarithmic derivative is equal to $-l-1$, lies at $\varepsilon_v = 0.28$ eV just above the bottom of the antibonding Sn *p* states. The crystal field at the Nb 4*a* site (O_h point symmetry) splits Nb *d* states into E_g ($3z^2-1$ and x^2-y^2) and T_{2g} (*xy*, *yz*, and *xz*) ones. The E_g states, which form σ bonds with Sn *p* states, are strongly hybridized with the latter and give a significant contribution to the bonding states below –2 eV. The T_{2g} states form weaker Ni *d* – Sn *p* π bonds but they hybridize strongly with *d* states of eight Co nearest neighbors.

The center of Co *d* states ($\varepsilon_v = -1.2$ eV) is found in a gap between the bonding and antibonding Sn *p* states. The crystal field at the Co 4*b* site (T_d point symmetry) causes the splitting of *d* orbitals into a doublet *E* ($3z^2-1$ and x^2-y^2) and a triplet T_2 (*xy*, *yz*, and *xz*). The hybridization between Co T_2 and Nb T_{2g} states, causes the splitting of the Nb T_{2g} states into two peaks, the bonding one located at ~2.5 eV below the Fermi level E_F and the unoccupied antibonding peak centered at 1.5 eV. The Co *E* orbitals are weakly hybridized with Sn and Nb states, however, they are split into well separated bonding and antibonding peaks by strong Co *d* –Co *d* σ hopping. It is important to note, that in the *Fm*3*m* structure the antibonding Co *E* states form a peak in the DOS at the Fermi level. The presence of the peak of antibonding states at E_F is a possible source of structure instability and can be responsible for the site disorder on an atomic scale in the *Fm*3*m* structure of Co_2NbSn [182].

In addition to the crystal field splitting, the *d* levels of the Co and Nb atoms are split due to the exchange interaction. The exchange splitting between the spin-up and down *d* electrons on the Co atom is about 0.5 eV. The corresponding splitting on the Nb atom is much smaller. Spin-orbit splitting of the *d* energy bands for both the Co and Nb atoms is much smaller than their spin and crystal-field splittings. The spin-polarized calculations show that Co_2NbSn in the high-temperature phase is not a half-metallic ferromagnet. The Fermi level crosses both the majority and minority spin energy bands.

The local symmetry in the low-temperature orthorhombic phase of Co_2NbSn reduces to C_2 and C_s at the 4*h* and 4*k* Co sites and to C_{2h} and C_{2v} at the 2*a* and 2*f* Nb sites,

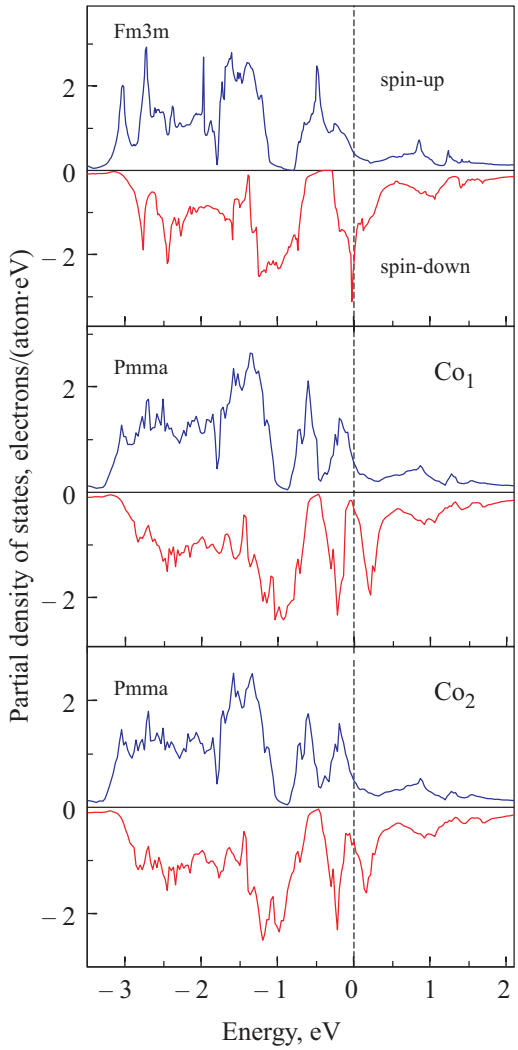

Fig. 22. The partial Co 3*d* density of states of Co_2NbSn for high, *Fm*3*m*, and low, *Pmma*, temperature structures [190].

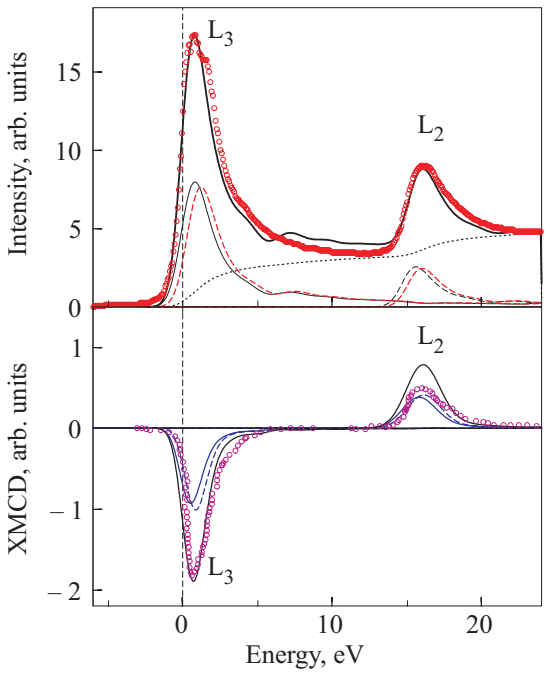

Fig. 23. Theoretically calculated (thick full line) and experimental (circles) isotropic absorption and XMCD spectra of Co_2NbSn at the Co $L_{2,3}$ edges. Experimental spectra [189] were measured at 50 K. The upper panel also shows the background spectra (dotted line) due to the transitions from inner $2p_{1/2,3/2}$ levels to the continuum of unoccupied levels [48]. Full and dashed lines present the spectra for Co_1 and Co_2, respectively [190].

respectively. The crystal field causes the *d* orbitals to split into five singlets at each site.

An important feature of the electronic structure of Co_2NbSn in the high temperature *Fm*3*m* structure is a high DOS of the minority-spin electrons at the Fermi energy, E_F. The Fermi level cuts the major peak of the density of antibonding Co *d* states of *E* symmetry at 10 meV from its maximum (Fig. 21). A large DOS at E_F signals an instability with respect to a structural phase transition. In the low temperature *Pmma* phase the Fermi level is situated in a local minimum of both the Co_1 and Co_2 *d* DOS's (Fig. 22). The value of the total DOS is decreased by more than a factor of two in going from the high to low temperature phase.

These changes of the density of states in the vicinity of the Fermi level are closely related to the changes of Co– Co interatomic distances (see Table 4). In the low-temperature phase Co_1–Co_1 and Co_2–Co_2 distances along the *y* direction shrink. The energy of Co orbitals forming σ bonds between these atoms (E orbitals in the *Fm*3*m* phase) increases and the corresponding peak of DOS is pushed above E_F. On the contrary, two of the four Co nearest neighbors in the *xz* plane move away from a Co site. The energy of the Co orbitals, that participate in σ bonds between these more distant atoms, lowers and the orbitals become occupied. This picture supports the suggestion made by Fujii et al. [186] that the driving force for the structural phase transition in Co_2NbSn is the band Jahn-Teller effect.

The experimentally measured dichroic lines have different signs at the L_3 and L_2 edges [189]. In order to compare relative amplitudes of the L_3 and L_2 XMCD spectra we first normalize the corresponding isotropic x-ray absorption spectra (XAS) to the experimental ones taking into account the background scattering intensity as described in Sec. 2. Figure 23 shows the calculated isotropic x-ray absorption and XMCD spectra of Co at the $L_{2,3}$ edges in the LSDA approach together with the experimental data [189]. The contribution from the background scattering is shown by dotted line in the upper panel of Fig. 23. The two nonequivalent Co ions produce similar XAS's with slightly different energy positions and different intensities, it leads to the peak structure with a high energy shoulder in L_3 and L_2 XAS's. This structure is less pronounced at the L_2 edge. This result can be ascribed to the lifetime broadening effect because the lifetime of the $2p_{1/2}$ core hole is shorter than the $2p_{3/2}$ core hole due to the Coster-Kronig decay [22].

Table 5 presents the comparison between calculated and experimental magnetic moments in Co_2NbSn. The spin magnetic moment at the tin site is very small. The spin moment at Nb sites is also small and for the low temperature phase has an opposite direction to the spin moment at Co sites.

The LSDA overestimates the spin moment on the Co site (Table 5). It might be connected with the presence of crystallographic disorder in this compound [182]. To investigate the crystallographic disorder we reduce the number of the symmetry operations to make all the atoms in the unit cell of *Pmma* lattice nonequivalent. Then we modeled the disorder by shifting some of Co, Nb, and Sn atoms from their nominal positions. We found that the displacement of only Nb and Sn atoms by 2% (with Co atoms in their nominal positions) reduces the average Co spin magnetic moment from 0.451 μ_B to 0.446 μ_B. However, the displacement of Co atoms by 2% (keeping Nb and Sn atoms in their nominal positions) leads to the reduction of the average Co spin magnetic moment to 0.325 μ_B. It is interesting to note that the displacements of Co atoms more than 4% from their nominal positions lead to a nonmagnetic ground state.

We also investigated the effect of the possible substitutional disorder in the compound by interchanging the Co ions with Sn or Nb ones. We found that the substitutional disorder greatly influences the spin magnetic moment of Co. The average Co spin magnetic moment is equal to 0.345 μ_B and 0.02 μ_B when 12.5% or 25% Co ions are interchanged with Sn or Nb ions, respectively.

It is interesting to compare the spin and orbital moments obtained from the theoretically calculated XAS and XMCD spectra through sum rules [Eqs. (15), (16)] with directly calculated LSDA values. In this case we at least avoid all the experimental problems. Sum rules reproduce the spin magnetic moments within 22% and 16% and the

Table 5 The experimental and calculated spin M_s and orbital M_l magnetic moments (in μ_B) of Co_2NbSn.

Method	Atom	M_s	M_l
Fm3m	Co	0.454	0.044
	Nb	0.0	0.012
	Sn	0.004	–0.001
Pmma	Co_1	0.491	0.031
	Co_2	0.410	0.028
	Nb_1	–0.013	0.007
	Nb_2	–0.015	0.010
	Sn_1	0.002	0.0
	Sn_2	0.005	0.0
sum rules	Co_1	0.380	0.024
	Co_2	0.343	0.020
sum rules[a]	Co_1	0.468	0.029
	Co_2	0.398	0.026
sum rules[b]	Co_1	0.480	0.030
	Co_2	0.416	0.027
expt. [189]	Co	0.38	0.09

Comment: [a]sum rules applied for the XMCD spectra calculated with ignore the energy dependence of the radial matrix element [b]sum rules footnote{sum rules applied for the XMCD spectra calculated with ignore the energy dependence of the radial matrix elements and ignore $p \to s$ transitions.

orbital moments within 22% and 29% for Co_1 and Co_2, respectively (Table 5). XMCD sum rules are derived within an ionic model using a series of approximations. We applied the sum rules to the XMCD spectra calculated neglecting the energy dependence of the radial matrix elements and the $p \to s$ transitions. As can be seen from Table 5 using the energy independent radial matrix elements reduces the disagreement in spin magnetic moments to 5% and 3% and in the orbital moment to 6% and 7% for Co_1 and Co_2, respectively. An additional omitting of the $p \to s$ transitions leads to almost perfect agreement between LSDA and sum rule results within 1–2% for the spin moments and 3% for the orbital moments. These results show that the energy dependence of the matrix elements and the presence of $p \to s$ transitions affect strongly the values of both the spin and the orbital magnetic moments derived using the sum rules.

The value of the orbital magnetic moment derived from the experimental XMCD spectra ($M_l^{\text{exp}} = 0.09\ \mu_B$ [189]) is considerably higher in comparison with our band structure calculations. It is a well-known fact, however, that LSDA calculations be inaccurate in describing orbital magnetism [20,22]. In the LSDA, the Kohn-Sham equation is described by a local potential which depends on the electron spin density. The orbital current, which is responsible for M_l, is, however, not included in the equations. This means, that although M_s is self-consistently determined in the LSDA, there is no framework to determine simultaneously M_l self-consistently. To calculate M_l beyond the LSDA scheme we used the rotationally invariant LSDA + U method [60]. We used $U = J = 1.0$ eV. The LSDA + U calculations produce the orbital magnetic moments equal to 0.046 μ_B for Co sites. This value is in better agreement with the experimental data but still smaller than the experimental estimations.

We should mention that in order to obtain the spin and orbital magnetic moments the authors of Ref. 189 first estimate the ratio $\langle l_z \rangle / \langle s_z \rangle$ without $\langle t_z \rangle$ term. To estimate the absolute values of M_s and M_l they used the value of the total magnetic moment at the Co site obtained by the magnetization measurements under high magnetic fields, neglecting the magnetic moments of other atoms. It is well known that the magnetic dipole operator t_z is quite small for cubic systems [22]. In our particular case the term $(7/2)\langle t_z \rangle$ in Eq. (16) is equal to 0.001 μ_B at Co site in the high-temperature cubic *Fm*3*m* structure. On the other hand, the experimental measurements in Ref. 189 have been done below Curie temperature, but for the low temperature orthorhombic *Pmma* structure the term $(7/2)\langle t_z \rangle$ is not small and is equal to 0.061 and 0.046 μ_B for Co_1 and Co_2, respectively. These two approximations can lead to additional errors in the estimation of the spin and orbital magnetic moments provided in Ref. 189.

The magnetic and structural phase transitions of the pseudo-ternary Heusler series $(Co_{1-x}Ni_x)_2NbSn$ (x = 0, 0.18, 0.56, 0.81, and 1) are experimentally studied in Ref. 187. The authors found that upon alloying Co_2NbSn with Ni, both the structural and the magnetic phase transition temperatures are suppressed to zero temperature with Ni content at $x = 0.32$ (T_c) and 0.47 (T_s).

We have calculated the electronic and magnetic structures as well as the XMCD spectra of the pseudo-ternary Heusler series $(Co_{1-x}Ni_x)_2NbSn$ for x = 0, 0.125, 0.25, 0.375, 0.5, 0.675, 0.75 and 1.0.

The simplest way to construct a pseudo-ternary Heusler alloy $(Co_{1-x}Ni_x)_2NbSn$ for $x = 0.5$ is to substitute one of the two inequivalent Co atoms by Ni in *Pmma* Co_2NbSn. The Ni atom can substitute Co atoms both at the 4*h* and 4*k* sites. The total energy calculations show that the more preferable site for Ni is the 4*k* site. Figure 24 presents the DOS's of CoNiNbSn compound in the *Pmma* crystal structure with Ni ions at the 4*k* site. To calculate the electronic structure of $(Co_{1-x}Ni_x)_2NbSn$ system for x = 0.125, 0.25, 0.375, 0.675 and 0.75 we reduce the number of the symmetry operations and make all the atoms in the unit cell of the *Pmma* lattice nonequivalent.

In contrast to the *Pmma* Co_2NbSn compound where the Fermi level is situated in a local minimum of the DOS, CoNiNbSn is characterized by quite high DOS at the Fermi energy. In the later case the Fermi level cuts the majority peak of Co spin-down *d* DOS at 20 meV from its maximum with the Ni atom at the 4*k* site (Fig. 24). When we place the Ni atom in the 4*h* site, E_F is situated exactly at the peak of Co spin-down density of states (not shown). The value of the total DOS in the $(Co_{1-x}Ni_x)_2NbSn$ system is increased by more than 30% going from $x = 0.0$ to $x = 0.5$. It should be mentioned, however, that this behavior is not monotonic and the lowest DOS was found for the alloy with $x = 0.25$. In this alloy the DOS is even smaller than in the stable Co_2NbSn compound. A large DOS at E_F for $x = 0.5$ alloy signals an instability of the crystal structure and can be considered as theoretical support of the experimental observation that upon alloying Co_2NbSn with Ni the structural phase transition temperatures are suppressed to zero temperature with Ni content at $x = 0.47$. Above this concentration the compound remains in the cubic *Fm*3*m* structure in the whole temperature range [187].

Our theoretical calculations give the ferromagnetic solution for the cubic *Fm*3*m* $(Co_{1-x}Ni_x)_2NbSn$ compounds only for for $x \le 0.125$. For larger Ni concentrations LSDA produces nonmagnetic solutions. Figure 25 presents partial DOS's of cubic *Fm*3*m* $(Co_{1-x}Ni_x)_2NbSn$ compound for $x = 0.5$. The DOS at the Fermi level in this case is considerably smaller in comparison with the DOS for the same compound in the *Pmma* crystal structure.

Table 6 presents the calculated magnetic moments for $(Co_{1-x}Ni_x)_2NbSn$ systems in the *Pmma* structure. The value of the magnetic moments in CoNiNbSn depends strongly on which site is occupied by the Ni atom. The band structure calculations give ferromagnetic solutions for the $(Co_{1-x}Ni_x)_2NbSn$ systems for *x* up to $x = 0.5$. Only alloys with $x \ge 0.625$ have no ferromagnetic solution. On the other hand, the experimental study of the magnetic phase transitions of the $(Co_{1-x}Ni_x)_2NbSn$ systems [187] reveals that the magnetic phase transition is suppressed already for $x = 0.32$. The LSDA overestimation of the

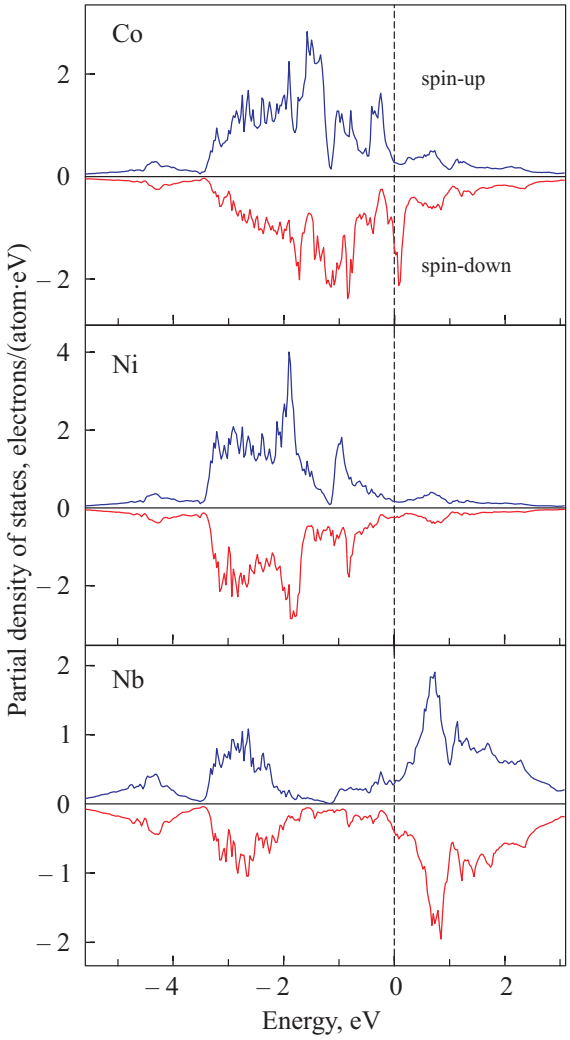

Fig. 24. The partial *d* density of states of $(Co_{1-x}Ni_x)_2NbSn$ for $x = 0.5$ system for *Pmma* structure with Ni atoms at the 4*k* site [190].

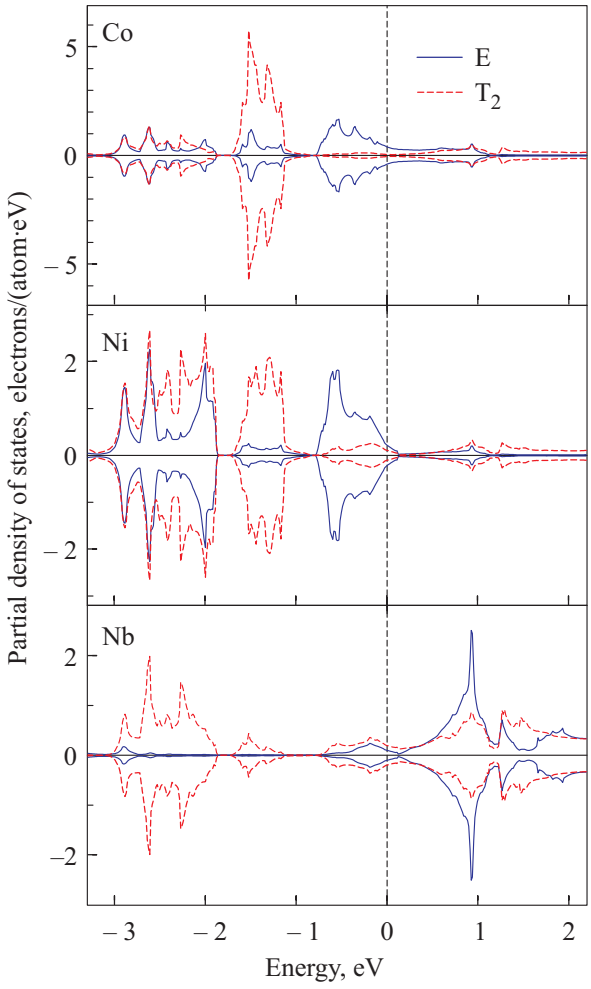

Fig. 25. The symmetry separated partial density of states of $(Co_{1-x}Ni_x)_2NbSn$ for the $x = 0.5$ system for the cubic *Fm*3*m* structure [190].

Table 6. The calculated spin M_s and orbital M_l magnetic moments (in μ_B) of $(Co_{1-x}Ni_x)_2NbSn$ systems in the *Pmma* structure for $x = 0.125$, 0.5 and 0.375. (We present averaged magnetic moments for different inequivalent sites.)

Method	Atom	M_s	M_l
$x = 0.5$	Co(4*h*)	0.506	0.032
Ni in 4*k*	Ni(4*k*)	0.006	0.001
	Nb(2*a*)	–0.019	0.0
	Nb(2*f*)	–0.026	0.010
$x = 0.5$	Co(4*k*)	0.351	0.031
Ni in 4*h*	Ni(4*h*)	0.004	0.001
	Nb(2*a*)	–0.009	0.009
	Nb(2*f*)	–0.021	0.002
$x = 0.125$	Co	0.435	0.032
	Ni	0.040	0.006
$x = 0.25$	Co	0.380	0.027
	Ni	0.025	0.001
$x = 0.375$	Co	0.431	0.030
	Ni	0.012	0.002
$x = 0.625$	Co	0.0	0.0
	Ni	0.0	0.0

tendency toward the magnetism in the $(Co_{1-x}Ni_x)_2NbSn$ systems is probably connected with the crystallographic disorder in these alloys [187].

The effect of Ni substitution for Co on the XMCD spectra of the pseudo-ternary Heusler series $(Co_{1-x}Ni_x)_2NbSn$ ($x = 0.5$) results simply in the disappearing of one of the components (dashed line at low panel in Fig. 23) because Ni $L_{2,3}$ spectra are situated in other energy range. As a result Co $L_{2,3}$ XMCD spectra are reduced in absolute value and slightly shifted to lower energy.

4.3. Noncollinear magnetism

4.3.1. IrMnAl. IrMnAl is classified as a weakly ferromagnetic compound with a Curie temperature of about 400 K [191]. IrMnAl crystallizes in the fluorite ($C1$) structure [191]. A Heusler structure differs from the $C1$ structure in having additional atoms at the edge centers and at the body center. The characteristic feature of the crystal structure of the intermetallic compound IrMnAl is the chemical disorder of Ir and Al atoms which randomly occupy the 8*c* positions in the $C1$ structure. Atomic disorder in the Heusler compounds is not a rare phenomenon and is well studied theoretically [150–156] and experimentally [192–195].

Recently x-ray magnetic circular dichroism in the ferromagnet IrMnAl has been measured at Ir $L_{2,3}$ edges [196]. The observation shows that Ir has a 5*d* magnetic moment in IrMnAl. Using the magneto-optic sum rules the spin moment and the orbital moment of Ir at 30 K have been deduced to be 0.018, and -0.0031 μ_B, respectively.

The magnetic moment in IrMnAl comes mainly from Mn atoms and has been reported to be 0.4 μ_B on the Mn site [191]. An even smaller magnetic moment of 0.123 μ_B/atom for IrMnAl was estimated from the magnetization measurements [196]. This magnetic moment is much smaller than the total moment of 2–5 μ_B found in ferromagnetic Mn compounds with either $L2_1$ or $C1_b$ crystal structure. For example, Mn has a moment of 4 μ_B in the Heusler alloy PtMnSb [197]. It is still not clear why Mn has a very small magnetic moment in IrMnAl although the Curie temperature is comparable to other Mn based ferromagnets. The small value of the net magnetic moment and the large Curie temperature of IrMnAl can be reconciled with either a small and partly delocalized Mn moment in an itinerant electron picture or with a large moment of Mn associated with a noncollinear magnetic structure. Here we address the possibility of noncollinear magnetic configurations in the $C1$ structure. We study the noncollinear magnetism by calculating the total energies for different spin spirals.

1. Crystal structure. The intermetallic compound IrMnAl crystallizes in the $C1$ structure [196] (space group: $F\bar{4}3m$, No. 225) in which Mn atoms occupy the 4*a* Wyckoff positions ($x = y = z = 0$) and Ir as well as Al atoms randomly occupy the 8*c* positions ($x = y = z = 1/4$), the vacancies are situated at the 4*b* sites ($x = y = z = 1/2$). The lattice constant a is found to be 5.992 Å [196]. To simplify the band structure calculations we assumed an additional ordering of Ir and Al ions in 8*c* sublattice (see Fig. 26) using the fcc structure with space group $F\bar{4}3m$ (No. 216). We place Ir and Al ions in 4*c* (1/4,1/4,1/4) and 4*d* (3/4, 3/4, 3/4) sites, respectively, leaving vacancies at the 4*b* (1/2, 1/2, 1/2) sites.

One should mention that in their early work. Matsumoto and. Watanabe [191] proposed another atomic occupation in the $C1$ structure of IrMnAl, namely, Mn atoms at the 4*a* sites, but Ir and Al randomly occupy 4*b* and 4*d* sites (with vacancies at the 4*c* sites). In this case 4*b* and 4*d* sites are not equivalent. Although the first configuration proposed in Ref. 196 seems to be more correct in our band structure calculations we used both the configurations to study possible intersite disorder in IrMnAl.

Table 7 presents the number and distance of the nearest neighbors for different type of atoms in the real structure (group 225) and model phases (group 216 and group 129) of IrMnAl investigated in Ref. 198.

2. Band structure. The total and partial DOS's of ferromagnetic IrMnAl obtained from the LSDA calculation are

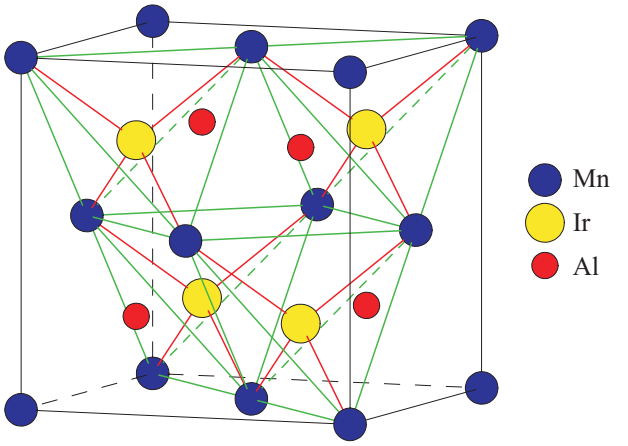

Fig. 26. The fcc structure of IrMnAl with space group $F\bar{4}3m$ (No. 216) with ordered Mn and Ir ions.

presented in Fig. 27. The occupied part of the valence band can be subdivided into several regions. The Al 3*s* bands appear between –8.4 and –5.5 eV. Al *p* states are spread over a broad energy range above –4.8 eV. The Ir and Mn *d* energy states are strongly hybridized and located above and below E_F at about –4.5 to 3.4 eV.

The *d* levels of the Mn and Ir atoms are split due to the crystal field. At both the Ir and Mn sites in the $F\bar{4}3m$ structure the crystal field causes the *d* orbitals to split into a doublet $e(3z^2-1$ and $x^2-y^2)$ and a triplet $t_2(xy, yz,$ and $xz)$. The spin-polarized calculations show that IrMnAl is not a half-metallic ferromagnet. The Fermi level crosses both the majority and minority spin energy bands. Spin-orbit splitting of the *d* energy bands for the Mn atoms is smaller than their spin and crystal-field splittings. The characteristic feature of the electronic structure of IrMnAl alloy is the strong hybridization of Mn 3*d* and Ir 5*d* states the later being more delocalized. Due to the hybridization the nonmagnetic Ir atom in IrMnAl becomes magnetic. The value of the Ir magnetic

Table 7. The number and distance of the nearest neighbors for different type of atoms in the real structure (group 225) and model phases (group 216 and group 129) of IrMnAl (in arb. units.).

Atom	Neighbors	Distance	Atom	Neighbors	Distance
group 216 Ir in 4*c*			group 216 Ir in 4*b*		
Mn	4×Ir	4.894	Mn	4×Al	4.894
	4×Al	4.894		6×Ir	5.651
	12×Mn	7.992		12×Mn	7.992
Ir	4×Mn	4.894	Ir	4×Al	4.894
	6×Al	5.651		6×Mn	5.651
	12×Ir	7.992		12×Ir	7.992
group 129			group 225		
Mn	4×Ir	4.894	Mn	4×Ir	4.894
	4×Al	4.894		4×Al	4.894
	12×Mn	7.992		12×Mn	7.992
Ir	4×Mn	4.894	Ir	4×Mn	4.894
	4×Ir	5.651		6×Ir/Al	5.651
	2×Al	5.651		12×Ir/Al	7.992
	4×Ir	7.992			
	8×Al	7.992			

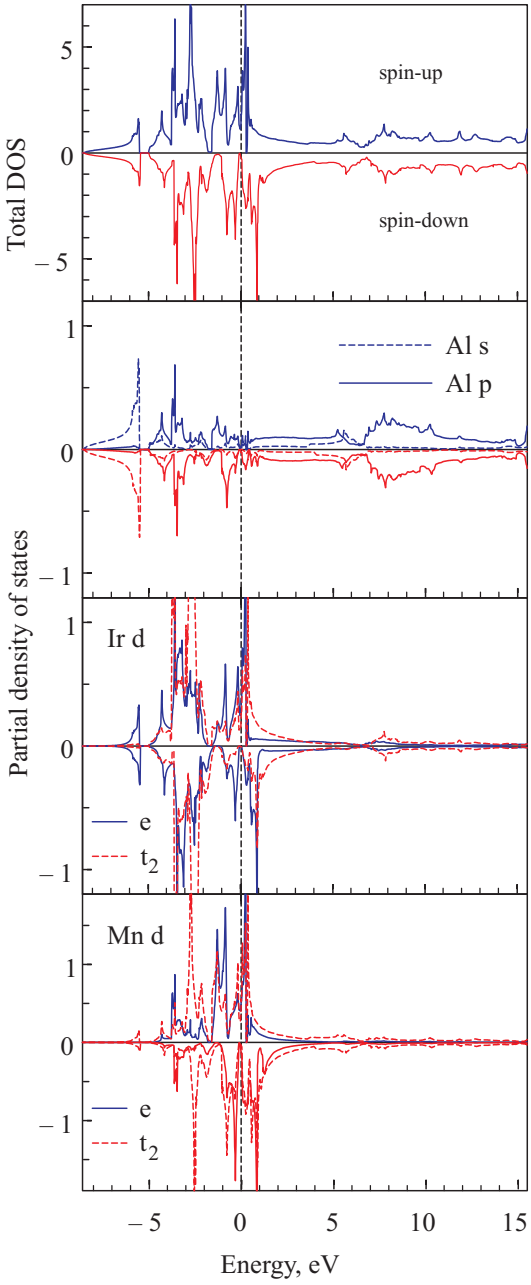

Fig. 27. The total (in states/(cell·eV)) and partial (in states/(atom·eV)) density of states of ferromagnetic IrMnAl in $F\bar{4}3m$ structure [198]. The Fermi energy is at zero.

moment depends on the number of the nearest neighbor Mn atoms and the Mn–Ir distances. The spin and orbital magnetic moments at the Ir site are equal to –0.063 μ_B and –0.094 μ_B, respectively. Due to strong Mn 3*d* and Ir 5*d* hybridization the spin magnetic moment at the Mn site is reduced to 1.105 μ_B, the orbital moment was found to be 0.114 μ_B.

3. Noncolinear magnetism. First, we have studied the possibility of noncollinear ordering by studying the energetics of spiral configurations. The total energy is calculated as a function of the spiral wave vector **q**, and the wave vector is varied along the high-symmetry directions [111], [100], and [110]. Vector **q** is given in units of $2\pi/a$ where *a* is the lattice constant of the *C*1 structure.

The total energies for the spiral wave vector **q** varying along the high-symmetry direction [111] are shown in Fig. 28. The variation of the total energy in [111] direction has the lowest energy for the antiferromagnetic configuration at **q** = (0.5, 0.5, 0.5). The corresponding spin magnetic structure is shown in Fig. 29 where we present only Mn and Ir spin moments in the positions according to the Fig. 26.

In order to obtain a deeper understanding of the energy dispersion we look into the behavior of magnetization. The Mn and Ir magnetic moments projected onto the local spin axis defined by the polar angles $\theta = 90^\circ$ and $\phi = \mathbf{qr}_n$ where $\mathbf{r}_n$ is the position of Mn or Ir site are shown in Fig. 28. The atomic magnetizations show that within the Mn spheres the magnetization is substantially increases going from the collinear ferromagnetic configuration **q** = (0, 0, 0) to the antiferromagnetic order **q** = (0.5, 0.5, 0.5). The magnetic moment in Ir changes a sign from negative to positive going from the collinear ferromagnetic configuration to the antiferromagnetic one.

The total energies for the spiral wave vector **q** varying along the high-symmetry directions [100] and [110] are shown in Fig. 30 together with the Mn and Ir spin magnetic moments. The variation of the total energy in [100] direction has the same tendency as it was observed in the [111] direction, namely the total energy monotonously lowers when going from the collinear ferromagnetic configuration **q** = (0, 0, 0) to the antiferromagnetic one **q** = (1, 0, 0). However, the total energy is slightly lower for the antiferromagnetic ordering with **q** vector along [100] direction in comparison with the [111] direction. The magnetization in Mn atomic sphere increases monotonically in the [100] direction going from the ferromagnetic to antiferromagnetic configuration.

The lowest total energy was found to be near the Brillouin-zone boundary at **q** = (0.75, 0.75, 0) corresponding to the spiral order which implies that the exchange coupling between nearest and next nearest Mn atoms is antiferromagnetic. In the [110] direction, the magnetization in Mn atomic sphere increases more rapidly reaching its maximum value of 2.603 μ_B at **q** = (0.6, 0.6, 0) before decreasing again to 2.45 μ_B in the antiferromagnetic state at **q** = = (1, 1, 0). The behavior of the Ir moment in the [110] symmetry direction shows stronger variation in comparison with the [100] direction. The spin magnetic moment at the Ir site reaches its maximum positive value at around **q** = (0.4, 0.4, 0) and vanishes for the antiferromagnetic configuration at **q** = (1, 1, 0).

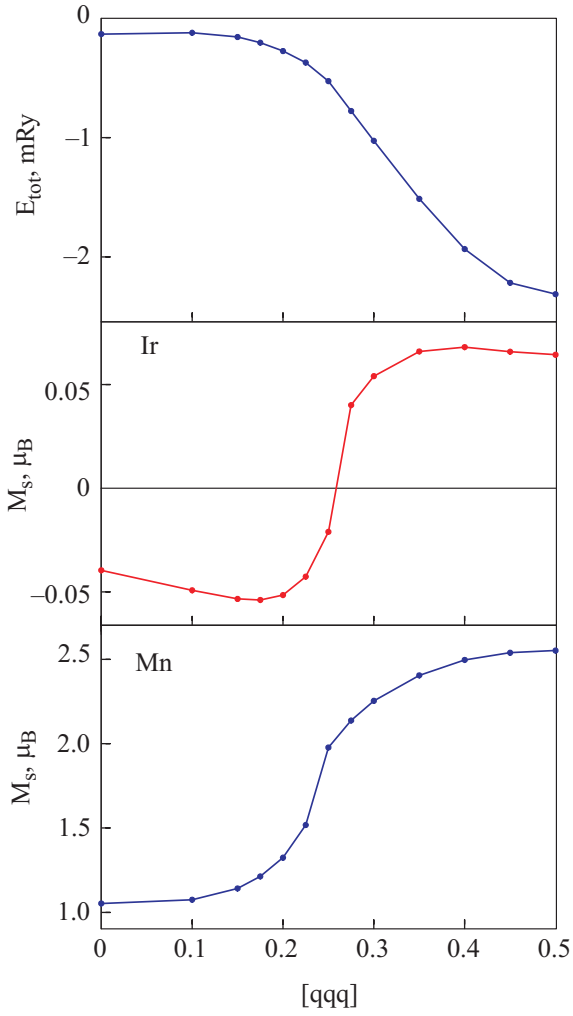

Fig. 28. Total energy and spin magnetic moments as a function of the spiral vector **q** varying along the [111] direction [198].

Figure 31 presents the spin magnetic structure for Mn and Ir sites corresponding to the spiral order for **q** = (0.75, 0.75, 0) possessing the lowest total energy. The electronic partial density of states for this spiral structure is presented in Fig. 32. Comparing Figs. 27 and 32 we can conclude that the electronic states are strongly redistributed going from the collinear ferromagnetic configuration to the magnetic spiral order.

These calculations show that the small value of the net magnetic moment in IrMnAl discovered experimentally [191] might be associated with noncollinear magnetic structure. A similar conclusion was drawn also by authors

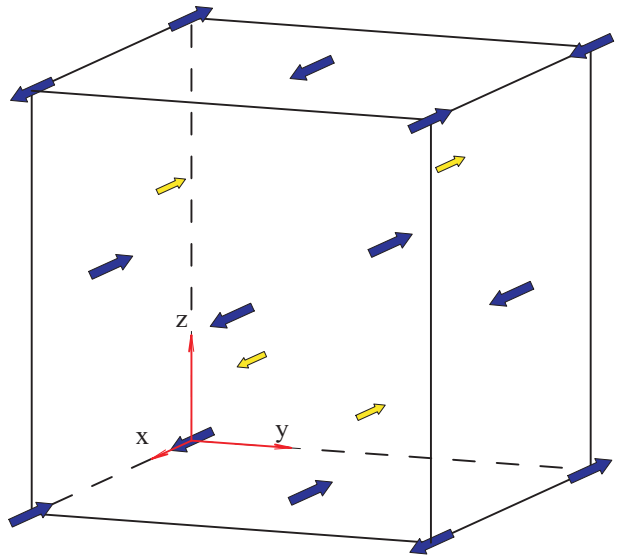

Fig. 29. Spin magnetic structure for spiral direction [111] and the spiral vector **q** = 0.5 (thick vector shows the spin direction of Mn atoms and thin one Ir atoms) [198].

of Ref. 196. Because we consider here only planar spirals, that is, $\theta_n = \pi/2$, the Mn and Ir spin magnetic moments are situated in the *xy* plane (Figs. 29 and 31) therefore the magnetization along the *z* axes is equal to zero.

From our band structure calculations IrMnAl has tendency for the antiferromagnetic ordering, the exchange coupling between nearest and next nearest Mn atoms is antiferromagnetic. On the other hand, the experimental magnetization measurements classified IrMnAl as a weakly ferromagnetic material with small net magnetization of 0.123 μ_B/atom [196]. The disagreements might be explained by the possible Mn — vacancy intersite disorder. To investigate such effect we carried out several super-cell band structure calculations in which we placed Mn atoms at variable vacant sites. We found that if some amount of the Mn atoms (from 12.5% to 25%) occupy vacant places the compound becomes ferrimagnetically ordered with the net magnetization of 0.068 –0.169 μ_B/atom depending on the number and the type of crystallographic positions occupied by the Mn atoms.

It is interesting to note that a full-Heusler compound Ir_2MnAl in $L2_1$ crystal structure without vacant places at all has an antiferromagnetic order [191].

4. XMCD spectra. At the core level edge XMCD is not only element-specific but also orbital specific. Recently, x-ray magnetic circular dichroism in the ferromagnet IrMnAl has been measured at Ir $L_{2,3}$ edges [196]. It was found that the experimentally measured dichroic lines have different signs at the L_3 and L_2 edges [196]. Figure 33,*a* shows the isotropic x-ray absorption and XMCD spectra of Ir at the $L_{2,3}$ edges calculated in the LSDA approach together with the experimental data [196]. The experimental measurements were carried out in external magnetic field of 1.15 T, and although the magnetization does not saturate at

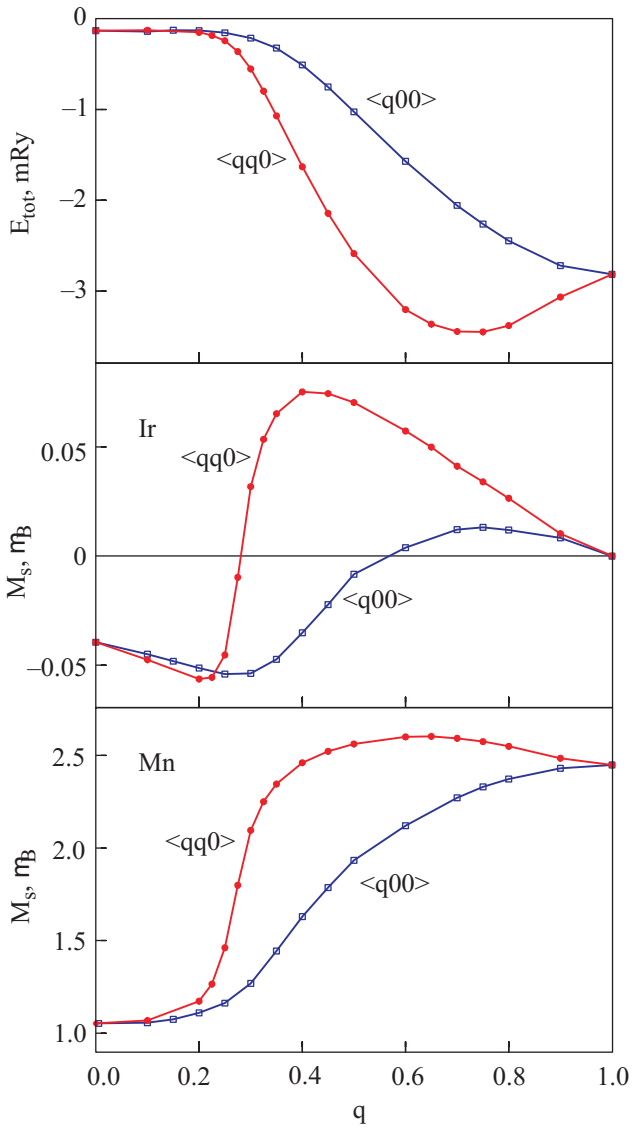

Fig. 30. Total energy and spin magnetic moments as a function of the spiral vector **q** varying along the [110] and [100] directions [198].

the highest applied field of 5.5 T we compare the measured XMCD spectra with calculated ones for the ferromagnetically ordered IrMnAl. It would be interesting to repeat the experiment at much higher magnetic fields to see how much the magnetic moments and the XMCD spectra change.

The experimental Ir L_3 XAS has a pronounced high energy shoulder. This structure is less pronounced at the L_2 edge. This result can be ascribed to the lifetime broadening effect because the lifetime of the $2p_{1/2}$ core hole is shorter than the $2p_{3/2}$ core hole due to the L_2L_3V Coster–Kronig decay. These features are due to the interband transitions from $2p$ core level to $3d$ empty states at around 8–20 eV above the Fermi level (Fig. 27) and quite well reproduced by the theoretical calculations (Fig. 33).

The theoretically calculated Ir $L_{2,3}$ XMCD spectra are in good agreement with the experiment, although small

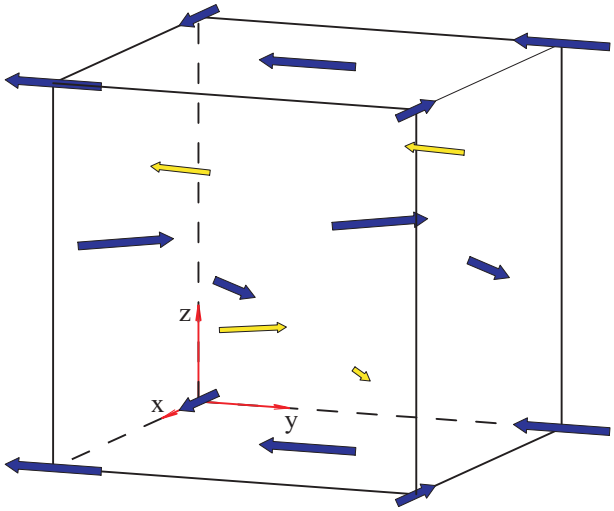

Fig. 31. Spin magnetic structure for spiral direction [110] and the spiral vector **q** = 0.75 (thick vector shows the spin direction of Mn atom and thin one Ir atom) [198].

shoulders at the high energy part of both the L_3 and L_2 spectra are not reproduced by our calculations. However, if we place Ir atoms at the 4*b* sites with Al atoms and vacancies at the 4*d* and 4*c* sites, respectively (as proposed by Matsumoto and Watanabe [191]) we have been able to reproduce these structures, but with much larger dichroic signal at the L_3 edge in comparison with the experimental data (not shown). We can conclude that probably some amount of Ir and Al atoms as well as vacant places randomly distributed between all the sites 4*c*, 4*d*, and 4*b* in the real IrMnAl crystal structure.

4.3.2. Mn_3ZnC. Ternary manganese compounds with a formula Mn_3MX (M = Ga, Sn, Zn and X = C and N) and the cubic crystal structure of a perovskite type have attracted much interest due to their large variety of magnetic orderings and structural transformations [199=207].

Mn_3GaC becomes a ferromagnet below T_c = 255 K. Furthermore, as the temperature decreases from T_c the first-order transition from a ferromagnet to an antiferromagnet, which involves a change of crystal structure from a cubic lattice to a rhombohedral one, has been observed at T_t = 165 K [208]. The antiferromagnetic ordering below T_t is of the second kind, with an easy axis along the [111] direction. In the case of Mn_3SnC the crystal structure is cubic in the whole temperature range and below T_c = 265 K this compound becomes magnetic. The magnetic ordering was reported to be complex [208].

In Mn_3ZnC, a magnetic phase transition occurs at T_t = = 233 K, which has been classified as a second-order transition from ferromagnetic phase (T_c = 380 K) to ferrimagnetic one with a non-collinear magnetic structure [206,207,209]. The transition is accompanied by a structural change from cubic to tetragonal. In the low-temperature phase, the tetragonality is monotonically decreased with decreasing temperature [210]. The magnetization also gradually decreases with temperature and eventually shows a cusp at T_t. In addition, Mn_3ZnC is magnetically hardened at low temperatures; the hysteresis loop becomes larger with decreasing temperature and the coercive force is linearly increased.

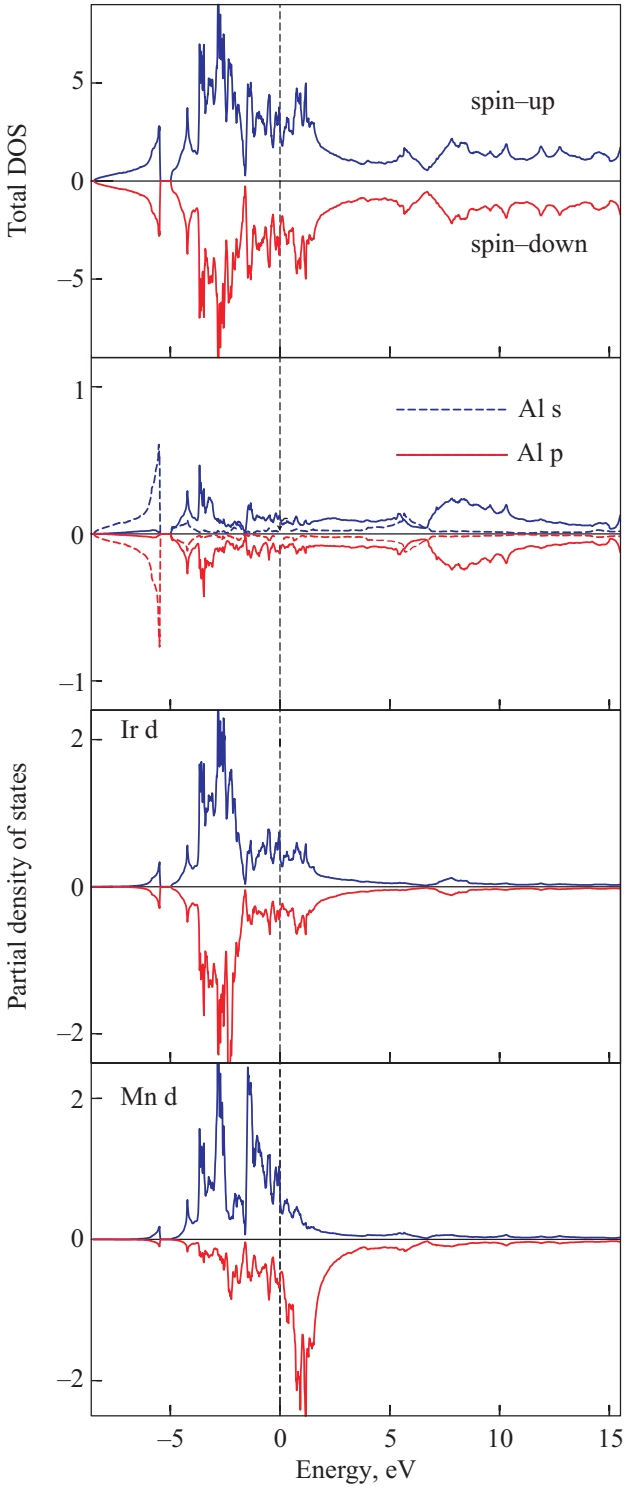

Fig. 32. The partial density of states of IrMnAl in $F4\bar{3}m$ structure for spiral direction [110] and the spiral vector **q** = 0.75 [198]. The Fermi energy is at zero.

In these three compounds the results of neutron diffraction show that the magnetic moments of Mn atoms are

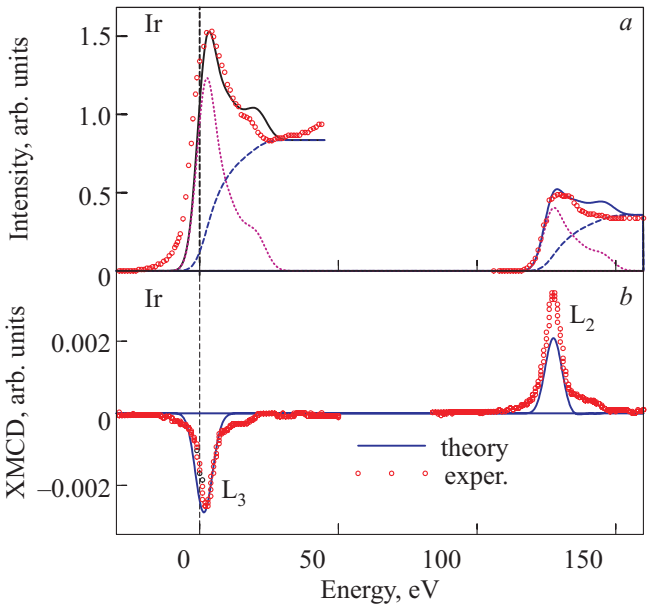

Fig. 33. Theoretically calculated [198] (dotted line) and experimental [196] (circles) isotropic absorption spectra of IrMnAl at the Ir $L_{2,3}$ edges. Experimental spectra were measured with external magnetic field (1.15 T) at 30 K. Dashed lines show the theoretically calculated background spectra, full thick lines are sum of the theoretical XAS and background spectra (*a*); Theoretically calculated (full lines) and experimental [196] (circles) XMCD spectra of IrMnAl at the Ir $L_{2,3}$ edges. (*b*).

much smaller than the $4-5\,\mu_B$ observed in other ordered manganese alloys [22]. This result indicates a strong itinerant character of 3*d* electrons of Mn atoms in Mn_3MX. The observed paramagnetic susceptibility obeys the Curie–Weiss law with $\mu = 1.9\,\mu_B$ for Mn_3ZnC and $\mu = 2.41\,\mu_B$ for Mn_3GaC [210]. In the case of Mn_3SnC the observed Curie-Weiss susceptibility has a slight upward convexity [207].

The electronic structure of these compounds plays the key role in determining their magnetic and structural properties. The energy band structure of the Mn_3MX system has been calculated by various methods [208,211–213]. Jardin and Labbe [211] performed a band calculation of cubic perovskite compounds Mn_3MX by applying a simple tight-binding approximation to the *d* electrons of Mn atoms and *p* electrons of X atoms. They found a sharp singularity in the electronic density of states at the Fermi level and pointed out that the singularity of the density of states could explain the nature of the magnetic and structural phase transitions. In Ref. 208 the electronic bands of Mn_3ZnC, Mn_3GaC, Mn_3InC and Mn_3SnC were calculated in the non-magnetic state of the cubic perovskite structure, by a selfconsistent augmented plane wave (APW) method. The ferromagnetic bands of Mn_3GaC has also been calculated in cubic structure. The energy band structure of Mn_3GaC in nonmagnetic, ferromagnetic (FM) and antiferromagnetic (AFM) states were calculated using a self-consistent linearized augmented-plane-wave (LAPW) method in Ref. 212. It was found that the conduction bands around the Fermi level consist mainly of the Mn 3*d* orbitals which are not bonding with C 2*p* orbitals. Total energies for both the FM and AFM states were calculated as a function of the unit cell volume.

The 4*p* states in transition metals usually attract only minor interest because they are not the states of constituting magnetic or orbital orders. Recently, however, understanding 4*p* states has become important since XMCD spectroscopy using *K* edges of transition metals became popular, in which the 1*s* core electrons are excited to the 4*p* states through the dipolar transition. The *K* edge XMCD is sensitive to electronic structures at neighboring sites, because of the delocalized nature of the 4*p* states. Recently in order to study the magnetic phase transition in Mn_3ZnC at 233 K, x-ray magnetic circular dichroism has been measured at the Mn *K*-edge as a function of temperature and magnetic field [210]. When the transition appears, the spectral intensity of the prominent peak shows an abrupt drastic increase with decreasing temperature and a linear reduction with increasing magnetic field.

1. Crystal structure..Mn_3ZnC at room temperature crystallize in the cubic perovskite-type structure with $Pm\bar{3}m$ space group (No. 221). Mn atoms being at the face centers, Zn atoms at the corners, and C atoms at the body center (see Fig. 34). The Mn atoms have two carbon nearest neighbors at the 1.965 Å distance. The second coordination consists of 8 Mn atoms and 4 Zn atoms at the 2.779 Å.

A ferromagnetic to ferrimagnetic phase transition in Mn_3ZnC at $T_t = 233$ K is accompanied by a structural change from cubic to tetragonal. Magnetic unit-cell of the low-temperature ferrimagnetic phase (*P*4*mmm* space group, No. 123) is composed of 4 formula units, and Mn ions form 4 layers and occupy 3 different sites [206]: Mn_1 possesses magnetic moments of 2.7 μ_B canting $\pm 65^\circ$ from the *c* –axis to [111] direction, the Mn_2 and Mn_3 have magnetic moments of 1.67 μ_B/Mn ferromagnetically aligned to the *c* –axis (Fig. 35). Therefore, the Mn moments constitute a non-collinear magnetic structure.

In the low-temperature tetragonal structure Mn–C interatomic distances are slightly decreased in comparison with the high temperature cubic phase up to the 1.958 Å. Mn_1 atoms are surrounded by $2Mn_2$ and $2Mn_3$ atoms at the 2.762 Å distance and $4Mn_1$ atoms at the 2.769 Å distance. Therefore, Mn–Mn interatomic distances are decreased through the cubic–tetragonal structure transition.

2. Energy band structure. The total and partial density of states of cubic ferromagnetic Mn_3ZnC are presented in Fig. 36. The results agree well with previous band structure calculations [212]. The occupied part of the valence band can be subdivided into several regions. C 2*s* states ap-

pear between –13.1 and –10.6 eV. Zn 3*d* states are fully occupied and cross the bottom of C 2*p* bands in a very narrow energy interval from –7.4 to –6.7 eV. C 2*p* states extended from –7 eV up to 15 eV. The states in the energy range –3.2 to 3.5 eV are formed by Mn *d* states. The crystal field at the Mn site (D_{4h} point symmetry) causes the splitting of *d* orbitals into three singlets a_{1g} and b_{1g} ($3z^2-1$ and x^2-y^2), $b_{2g}(xz)$ and a doublet e_g (xy, yz). The $a_{1g}-b_g$ and $b_{2g}-e_g$ splittings are negligible in comparison with its width in LSDA calculations, therefore we present in Fig. 36 DOS of e_g orbitals as a sum of the a_{1g} and b_{1g} ones and t_{2g} orbitals as a sum of the b_{2g} and e_g ones. One should mention that there is quite a small C 2*p*–Mn *d* hybridization in the valence bands below the Fermi level.

Mn_3ZnC in cubic perovskite type crystal structure has a local magnetic moments of 2.362 μ_B on Mn, –0.062 μ_B on Zn and –0.196 μ_B on C.

The orbital moments are equal to 0.028 μ_B, 0.001 μ_B and 0.0001 μ_B on the Mn, Zn and C sites, respectively. Our calculations produce larger magnetic moments at the Mn site in comparison with the Takahashi and Igarashi results [213]. The interaction between the transition metals is ferrimagnetic, leading to a total calculated moment of 6.935 μ_B.

Mn_3ZnC partial DOS's for the low-temperature tetragonal structure are presented in Fig. 37. For this crystal structure a spin magnetic moments are of 2.269 μ_B on noncollinear Mn_1 atom sites, 1.956 μ_B on collinear $Mn_{2,3}$ ones, –0.041 μ_B on Zn and –0.114 μ_B on C sites. The orbital moments are equal to –0.022 μ_B, 0.009 μ_B, –0.002 μ_B and –0.002 μ_B on the Mn_1, $Mn_{2,3}$, Zn and C sites, respectively. Our calculations produce smaller spin magnetic moments at the Mn_1 sites and larger at the $Mn_{2,3}$ sites in comparison with the experimental data [206].

3. XMCD spectra. Figure 38,*b* shows the theoretically calculated Mn *K*-edge x-ray absorption spectra as well as XMCD spectra in Mn_3ZnC in comparison with the corresponding experimental data [210]. In order to compare

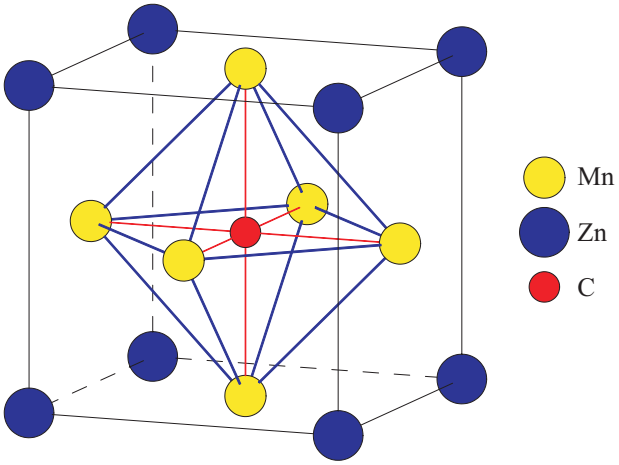

Fig.34. Cubic perovskite-type crystal structure of Mn_3ZnC at room temperature.

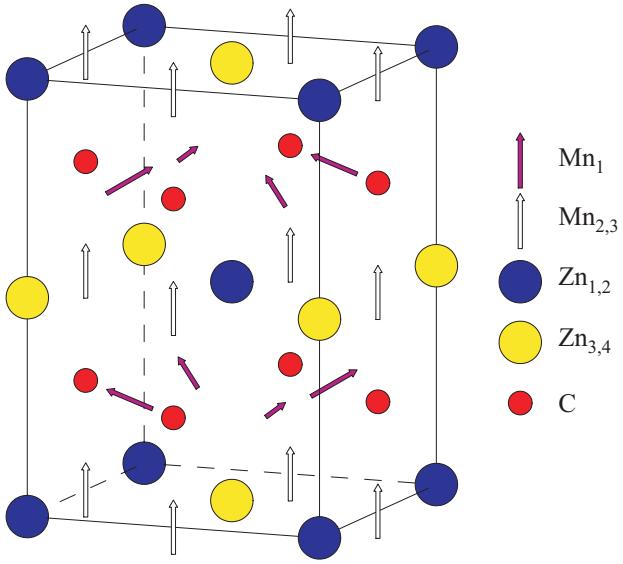

Fig. 35. Low-temperature magnetic structure of Mn_3ZnC.

relative amplitudes of the *K* XMCD spectra we first normalize the theoretically calculated x-ray absorption spectra to the experimental ones taking into account the background scattering intensity [48] (Fig. 38,*a*). There are no large differences in the shape of XAS for low- and high-temperature phases of Mn_3ZnC in agreement with the experimental measurements which show no significant temperature variation of XAS [210]. The experimental x-ray absorption spectra have three humps around 1.5, 5 and 10 eV above the Fermi level, which are well reproduced by the theoretical calculations.

Figure 38,*b* shows the experimental XMCD spectrum [210] measured at 300 K and the theoretically calculated one using the LSDA approximation for cubic high temperature phase. The theory is in good agreement with previous calculations [213] and the experimental measurements, although the calculated magnetic dichroism is somewhat too high at the 5 eV (peak *C*) and in the 9 to 13 eV energy range.

The 4*p*–3*d* hybridization and the spin-orbit interaction (SOI) in the 4*p* states play a crucial role for the *K* edge dichroism. We calculated the site-dependent function $dm_{tl}(E)$ (Eq. (36)) [139]. As can be seen from Fig. 38,*b* the *K* XMCD spectrum and $dm_{tl}(E)$ function are indeed closely related to one another giving a rather simple and straightforward interpretation of the XMCD spectra at the *K* edge.

The *K* XMCD spectra come from the orbital polarization in the empty *p* states, which may be induced by (1) the spin polarization in the *p* states through the SOI, and (2) the orbital polarization at neighboring sites through hybridization. We calculated the XMCD spectra at Mn sites in the ferromagnetic cubic phase of Mn_3ZnC with turning the SOI off separately on the Mn 4*p* states and the Mn 3*d* states, respectively. We found that when the SOI on

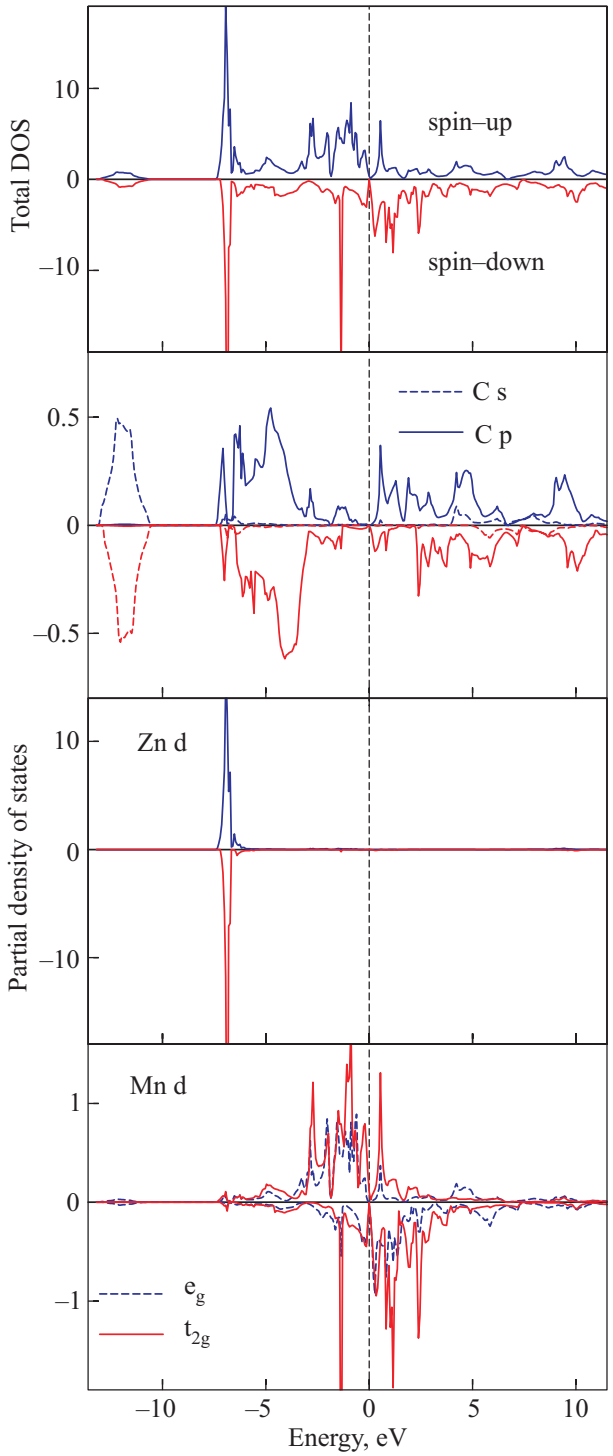

Fig. 36. The total (in states/(cell·eV)) and partial (in states/(atom·eV)) ferromagnetic density of states of Mn_3ZnC in cubic perovskite-type structure [214]. The Fermi energy is at zero.

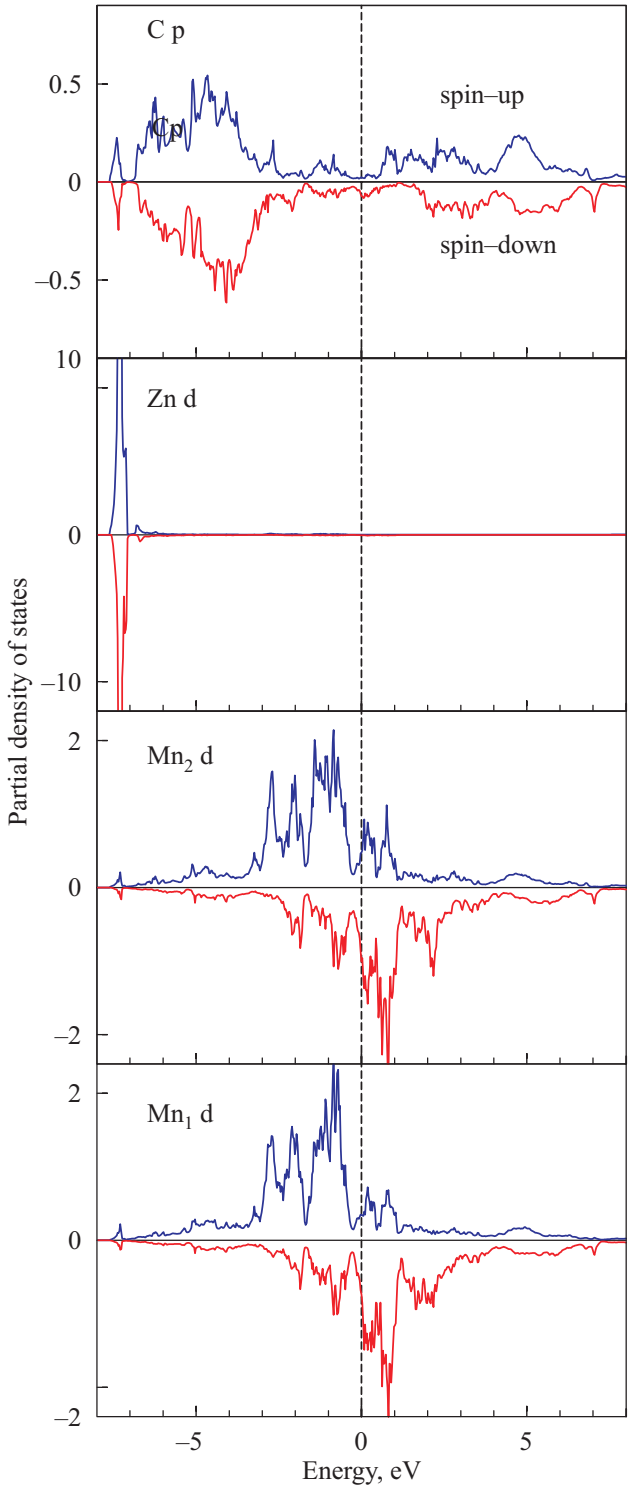

Fig. 37. Partial density of states (in states/(atom·eV)) of Mn_3ZnC in low temperature non-collinear tetragonal structure [214]. The Fermi energy is at zero.

the Mn 3*d* states is turned off the spectrum above 3.5 eV does not change, while the negative peak *B* is reduced and the prominent peak near the *K* edge (peak *A*) is largely diminished. On the other hand, when the SOI on the Mn 4*p* orbital is turned off, peaks *A* and *B* keep a similar shape, while peak *C* is reduced intensity and the minimum *D* almost vanishes. We can conclude that the 3*d* orbital polarization at neighboring Mn sites induces the *p* orbital polarization near the edge through the $4p-3d$ hybridization. The spectrum for 3.5 eV above the Fermi level originates from the spin polarization in the 4*p* symmetric states through the SOI. Similar results have been obtained

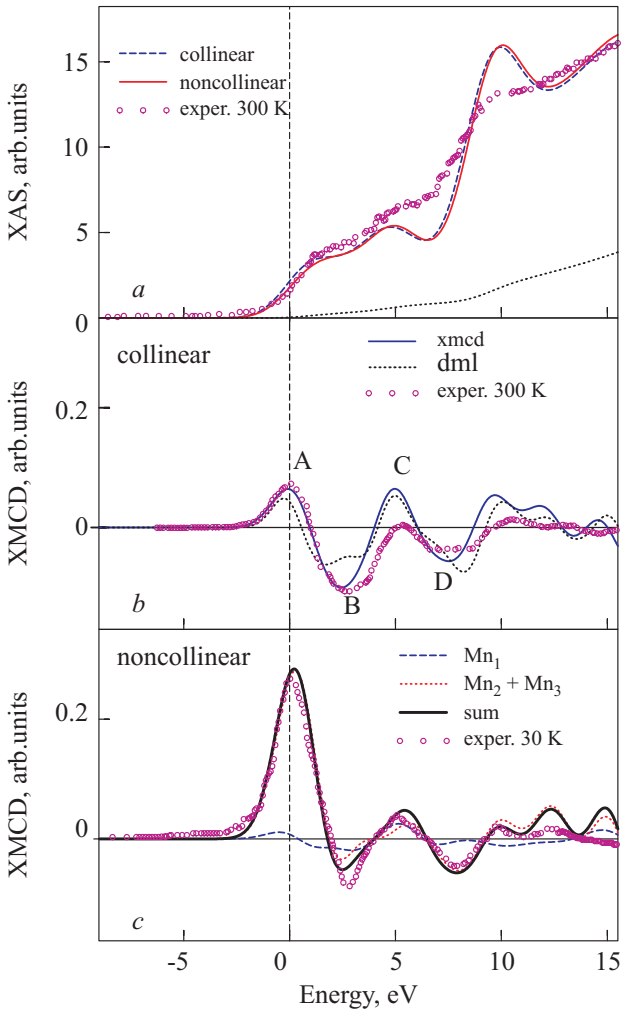

Fig. 38. Theoretically calculated [214] isotropic absorption spectra of Mn_3ZnC at the Mn K edge for cubic high temperature phase (dashed line) and low temperature tetragonal structure (full line) in comparison with the experimental spectrum [210] (circles) measured at 300 K. The dotted line shows the theoretically calculated background spectrum (*a*); The experimental XMCD spectrum [210] measured at 300 K (circles) and theoretically calculated XMCD spectra for cubic high temperature phase (full line), the dotted line presents the $dm_{l=1}(E)$ function (see the explanation in the text) (*b*); Theoretically calculated XMCD spectrum for low temperature tetragonal structure in comparison with the experimental measurements at 30 K [210] (circles); dashed and dotted lines show the theoretically calculated contributions from Mn_1 and $Mn_2 + Mn_3$ sites, respectively, the thick full line is the total spectrum (*c*).

by Takahashi and Igarashi in the ferromagnetic cubic phases of Mn_3GaC [213].

The experimental Mn K XMCD spectrum shows a noteworthy variation with temperature [210]. As the temperature is decreased the dichroic intensity of peak A is rapidly increased, with other peaks being almost unaffected. When the positive peak A overcomes the negative contribution of peaks B, C and D the value of $4p$ orbital magnetic moment M_L^p indicates a reversal of sign from positive to negative around 185 K. The change in orbital moment is obviously associated with the appearance of the noncollinear magnetic structure.

Figure 38,*c* presents the calculated XMCD spectra for low-temperature tetragonal Mn_3ZnC compound at the Mn K edges compared with the experimental data [210]. Although the number of Mn_1 atoms which are canting $\pm 65^\circ$ from the c axis to [111] direction is two times larger than the number of ferromagnetically aligned Mn_2 and Mn_3 atoms (Fig. 35) the main contribution to the prominent peak A situated near the Fermi-edge comes from the $Mn_{2,3}$ atoms (Fig. 38,*c*). We found that $dm_{l=1}(E)$ function is three times larger at the $Mn_{2,3}$ sites than at Mn_1 one around the Fermi edge. The orbital magnetic moment in p projected DOS is equal to $-0.00010\ \mu_B$ at Mn_1 and $-0.00102\ \mu_B$ at the $Mn_{2,3}$ sites. Therefore the effect of SO coupling in $4p$ states is different for particular Mn sites in Mn_3ZnC.

To estimate the Mn orbital moment in the p–projected states the authors of Ref. 210 integrated the experimental XMCD spectrum over a range of –5 eV to 13 eV. The integrated XMCD intensity has a positive value in the tetragonal ferrimagnetic phase, which signifies a negative orbital magnetic moment in the p-projected bands by the relation $M_L = -\langle l_z \rangle \mu_B$. On the assumption of $n_h = 6$, the magnitude of M_L^p was estimated to be around $-0.00075\ \mu_B$/Mn from the sum rules (Eq. (17)).

We apply sum rules to our theoretically calculated XMCD spectra and obtained $M_L^p = -0.00012\ \mu_B$ and $-0.00136\ \mu_B$ for the Mn_1 and the $Mn_{2,3}$ sites, respectively, which gives the value of the $M_L^p = -0.00054$/Mn μ_B in reasonable agreement with the experimental estimations and band structure calculations.

We found that the $dm_{l=1}(E)$ function is 1.5 times larger at the $Mn_{2,3}$ sites than at the Mn site in cubic hight temperature phase around the Fermi edge. Besides, due to lowering crystal symmetry from cubic to tetragonal through structural phase transition and decreasing the Mn –Mn interatomic distances the $4p-3d$ hybridization is increased. It affects mostly the states near the Fermi-edge because the Mn d DOS are rather small at ≥ 3.5 eV above the Fermi level (Fig. 37), therefore the main changes of the intensity of dichroic signal due to this effect one would expect at the prominent peak A (Fig. 38,*c*).

We can conclude that the increase of the $4p-3d$ hybridization and change of the effect of SO coupling in the $4p$ states leads to a strong increase of the spectral intensity of the prominent peak A through structural and magnetic phase transitions at $T_t = 233$ K.

The authors of Ref. 210 measured magnetic field variation of the dichroic spectrum and found surprising results: the peaks B and D are sensitive and increase with negative intensity, whereas the peak A is rather insensitive to the applied magnetic field (just slightly increases with increasing magnetic field from 0.5 to 10 T). There-

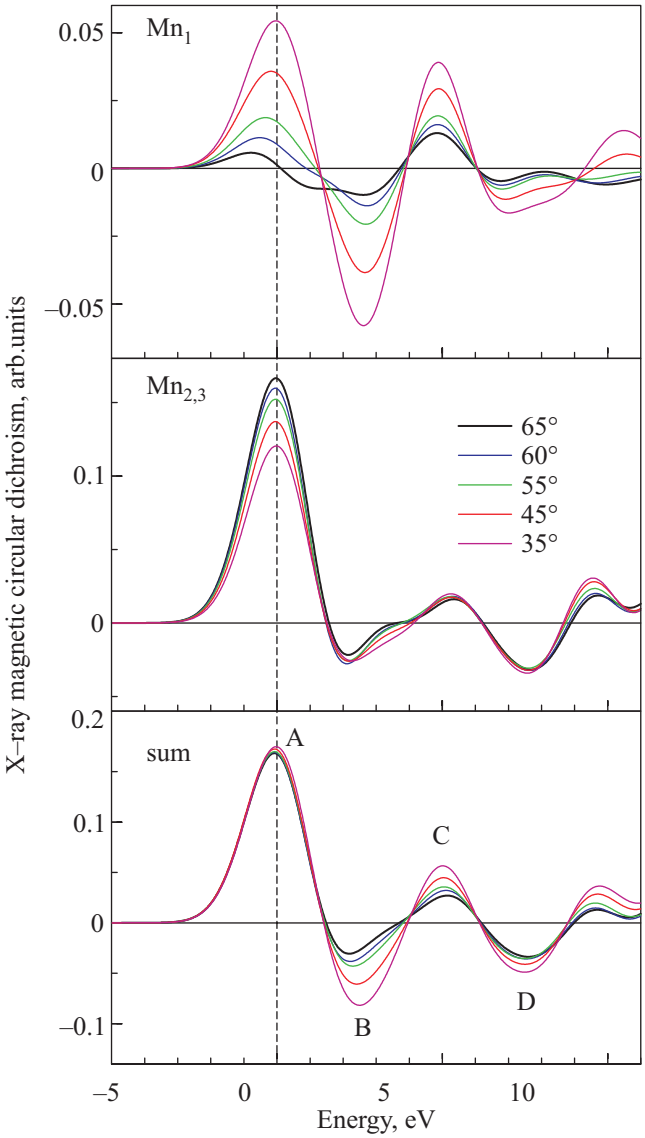

Fig. 39. Theoretically calculated [214] XMCD spectra at the Mn_1 and $Mn_{2,3}$ sites as a function of the canted Mn_1 angle for low-temperature tetragonal structure.

fore the dichroic spectral peak makes a different response to the external parameters; roughly, the peak *A* is sensitive to temperature, while the other peaks to magnetic field. The authors speculate that this behavior indicates a process in which the canted Mn orbital moments are forcedly aligned to the direction of applied magnetic field.

We investigated the influence of the Mn_1 canting angle on the XMCD spectra and $4p$ orbital magnetic moments at Mn sites. Figure 39 presents the theoretically calculated XMCD spectra at the Mn_1 and $Mn_{2,3}$ sites as a function of the Mn_1 canting angle for the low temperature tetragonal structure. We found that the prominent peak *A* is rather insensitive to the Mn_1 canting in the 65° to 35° angle interval. On the other hand, the peak *B* strongly increased in the same angle range. It can be explained by different behavior of the these peaks at the Mn_1 and

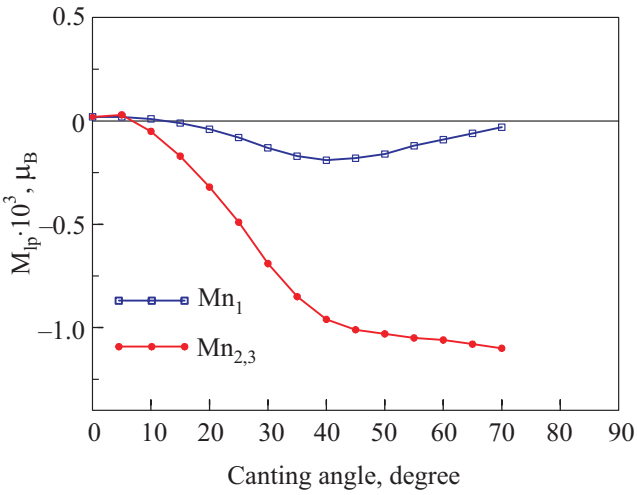

Fig. 40. Variation of Mn $4p$ orbital moments at the Mn_1 and $Mn_{2,3}$ sites with the canted Mn_1 angle [214].

$Mn_{2,3}$ sites. In decreasing of the canted angle the intensity of peak *A* is increased at the Mn_1 site and decreased at the Mn_1 sites, almost compensating each other. However, the peak *B* increased at both nonequivalent sites, with an especially strong increase at the Mn_1 site. We found a similar behavior also for the function $dm_{l=1}(E)$ (not shown).

Figure 40 presents variation of Mn $4p$ orbital moments at the Mn_1 and $Mn_{2,3}$ sites with the canting Mn_1 angle. Both the orbital moments are negative for most of the angle interval. The $Mn_{2,3}$ $4p$ orbital moments are slightly decreased when canting angle changes from 65° to 40°, and more quickly decrease with further decreasing of the canting angle. On the other hand, the Mn_1 $4p$ orbital moment is first increased from 65° to 40° and then decreased. As the canting Mn_1 angle is decreased further, the value of M_L^p indicated a reversal of sign from negative to positive around 15° and 7° for the Mn_1 and $Mn_{2,3}$sites, respectively, which is responsible for the trend that the negative peaks *B* and *D* overcome the positive contribution of peaks *A* and *C*.

1. M. Faraday, *Philos. Trans. R. Soc*. **136**, 1 (1846).
2. J. Kerr, *Philos. Mag*. **3**, 321 (1877).
3. M.J. Freiser, *IEEE Transactions on Magnetics* **4**, 1 (1968).
4. H.R. Hulme, *Proc. Roy. Soc. (London)* **A135**, 237 (1932).
5. C. Kittel, *Phys. Rev*. **83**, A208 (1951).
6. P.N. Argyres, *Phys. Rev*. **97**, 334 (1955).
7. B.R. Cooper, *Phys. Rev.* **139**, A1504 (1965).
8. R.Kubo, *J. Phys. Soc. Jpn*. **12**, 570 (1957).
9. A.E. Kondorsky and A.V. Vediaev, *J. Appl. Phys.* **39**, 559 (1968).
10. C.S. Wang and J. Callaway, *Phys. Rev.* **B9**, 4897 (1974).
11. M. Singh, C.S. Wang, and J. Callaway, *Phys. Rev.* **B11**, 287 (1975).
12. J.L. Erskine and E.A. Stern, *Phys. Rev*. **B12**, 5016 (1975).
13. B.T. Thole, G. van der Laan, and G.A. Sawatzky, *Phys. Rev. Lett.* **55**, 2086 (1985).

14. G. van der Laan, B.T. Thole, G.A. Sawatzky, J.B. Goedkoop, J.C. Fuggle, J.M. Esteva, R.C. Karnatak, J.P. Remeika, and H.A. Dabkowska, *Phys. Rev.* **B34**, 6529 (1986).
15. G. Schütz, W. Wagner, W. Wilhelm, P. Kienle, R. Zeller, R. Frahm, and G. Materlik, *Phys. Rev. Lett.* **58**, 737 (1987).
16. G. Schütz, R. Frahm, P. Mautner, R. Wienke, W. Wagner, W. Wilhelm, and P. Kienle, *Phys. Rev. Lett.* **62**, 2620 (1989).
17. H. Ebert, P. Strange, and B.L. Gyorffy, *J. Appl. Phys.* **63**, 3055 (1988).
18. C.T. Chen, F. Sette, Y. Ma, and S. Modesti, *Phys. Rev.* **B42**, 7262 (1990).
19. G. van der Laan and B.T. Thole, *Phys. Rev.* **B43**, 13401 (1991).
20. H. Ebert, *Rep. Prog. Phys.* **59**, 1665 (1996).
21. A. Yaresko, A. Perlov, V. Antonov, and B. Harmon, in: *Magnetism: A Synchrotron Radiation Approach*, Vol. 697 of *Lecture Notes in Physics*, F.S.E. Beaurepaire, H. Bulou, and J.-P. Kappler (eds.), Springer, Berlin–Heidelberg (2006), p. 121.
22. V. Antonov, B. Harmon, and A. Yaresko, *Electronic Structure and Magneto-Optical Properties of Solids*, Kluwer Academic Publishers, Dordrecht, Boston, London (2004).
23. J.P. Hannon, G.T. Trammel, M. Blume, and D. Gibbs, *Phys. Rev. Lett.* **61**, 1245 (1988).
24. S.W. Lovsey and S.P. Collins, *X-Ray Scattering and Absorption in Magnetic Materials*, Oxford University Press, Oxford (1996).
25. J.B. Kortight and S.-K. Kim, *Phys. Rev.* **B62**, 12216 (2000).
26. M.I. Friezer, *IEEE Transactions on Magnetics* **4**, 152 (1968).
27. G.Y. Guo, *Phys. Rev*. **B55**, 11619 (1998).
28. P.J. Durham, in: *The Electronic Structure of Complex Systems*, P. Phariseu and W.M. Temmerman (eds.), Plenum, New York (1984).
29. W.H. Kleiner, *Phys. Rev*. **142**, 318 (1966).
30. F.U. Hillebrecht, C. Roth, H.B. Rose, W.G. Park, E. Kisker, and J. Kirschner, *Phys. Rev*. **B55**, 2594 (1997).
31. J.G. Menchero, *Phys. Rev*. **B57**, 993 (1998).
32. G. van der Laan, *J. Magn. Magn. Mater*. **148**, 53 (1995).
33. G. van der Laan, *J. Electron. Spectrosc. Relat. Phenom*. **86**, 41 (1997).
34. G. van der Laan, *J. Phys.: Condens. Matter* **9**, L259 (1997).
35. G. van der Laan, *Phys. Rev*. **B57**, 5250 (1998).
36. J.G. Menchero, *Phys. Rev*. **B57**, 1001 (1998).
37. A. Fanelsa, R. Schellenberg, F.U. Hillebrecht, E. Kisker, J.G. Menchero, A.P. Kaduwela, C.S. Fadley, and M.A.V. Hove, *Phys. Rev.* **B54**, 17962 (1996).
38. J.G. Menchero, C.S. Fadley, G. Panaccione, F. Sirotti, G.J. Henk, and R. Feder, *Phys. Rev.* **B55**, 11476 (1997).
39. J.G. Menchero, *Phys. Rev*. **B55**, 5505 (1997).
40. R. Schellenberg, E. Kisker, A. Fanelsa, F.U. Hillebrecht, J.G. Menchero, A.P. Kaduwela, C.S. Fadley, and M.A.V. Hove, *Phys. Rev.* **B57**, 14310 (1998).
41. H. Ebert, L. Baumgarten, C.M. Schneider, and J. Kirschner, *Phys. Rev.* **B44**, 4406 (1991).
42. H. Ebert and G.-Y. Guo, *J. Magn. Magn. Mater.* **148**, 178 (1995).
43. G.Y. Guo, H. Ebert, W.M. Temmerman, and P.J. Durham, *Phys. Rev*. **B50**, 3861 (1994).
44. E. Tamura, G.D. Waddill, J.G. Tobin, and P.A. Sterne, *Phys. Rev. Lett.* **73**, 1533 (1994).
45. V.V. Nemoshkalenko and V.N. Antonov, *Computational Methods in Solid State Physics*, Gordon and Breach Science Publication, Amsterdam (1998).
46. V.N. Antonov, A.I. Bagljuk, A.Y. Perlov, V.V. Nemoshkalenko, Vl.N. Antonov, O.K. Andersen, and O. Jepsen, *Fiz. Nizk. Temp*. **19**, 689 (1993)[*Low Temp. Phys.* **19**, 494 (1993)].
47. V.V. Nemoshkalenko, V.N. Antonov, Vl.N. Antonov, W. John, H. Wonn, and P. Ziesche, *Phys. Status Solidi* **B111**, 11 (1982).
48. F.K. Richtmyer, S.W. Barnes, and E. Ramberg, *Phys. Rev.* **46**, 843 (1934).
49. G. van der Laan and B.T. Thole, *Phys. Rev.* **B38**, 3158 (1988).
50. B.T. Thole, P. Carra, F. Sette, and G. van der Laan, *Phys. Rev. Lett.* **68**, 1943 (1992).
51. P. Carra, B.T. Thole, M. Altarelli, and X. Wang, *Phys. Rev. Lett.* **70**, 694 (1993).
52. G. van der Laan and B.T. Thole, *Phys. Rev.* **B53**, 14458 (1996).
53. S. Uemoto, H. Maruyama, N. Kawamura, S. Uemura, N. Kitamoto, H. Nakao, S. Hara, M. Suzuki, D. Fruchart, and H. Yamazaki, *J. Synchrotron Radiation* **8**, 449 (2001).
54. V.I. Anisimov, J. Zaanen, and O.K. Andersen, *Phys. Rev*. **B44**, 943 (1991).
55. P.W. Anderson, *Phys. Rev*. **124**, 41 (1961).
56. J. Hubbard, *Proc. Roy. Soc. (London)* **A276**, 238 (1963).
57. J. Hubbard, *Proc. Roy. Soc. (London)* **A277**, 237 (1964).
58. V.I. Anisimov, I.V. Solovyev, M.A. Korotin, M.T. Czyzyk, and G.A. Sawatsky, *Phys. Rev.* **B48**, 16929 (1993).
59. I.V. Solovyev, A.I. Liechtenstein, and K. Terakura, *Phys. Rev. Lett.* **80**, 5758 (1998).
60. A.N. Yaresko, V.N. Antonov, and P. Fulde, *Phys. Rev.* **B67**, 155103 (2003).
61. H. Harima, *J. Magn. Magn. Mater.* **226–230**, 83 (2001).
62. C. Herring, in: *Magnetism*, G.T. Rado and H. Suhl (eds.), Academic, New York (1966), Vol. IV.
63. V.I. Anisimov and O. Gunnarsson, *Phys. Rev.* **B43**, 7570 (1991).
64. P.H. Dederichs, S. Blügel, R. Zeller, and H. Akai, *Phys. Rev. Lett.* **53**, 2512 (1984).
65. I.V. Solovyev, P.H. Dederichs, and V.I. Anisimov, *Phys. Rev.* **B50**, 16861 (1994).
66. W.E. Pickett, S.C. Erwin, and E.C. Ethridge, *Phys. Rev.* **B58**, 1201 (1998).
67. J. Enkovaara, A. Ayuela, J. Jalkanen, L. Nordström, and R.M. Nieminen, *Phys. Rev*. **B67**, 054417 (2003).
68. L.M. Sandratskii, *J. Phys.: Condens. Matter* **3**, 8565 (1991).
69. L. Sandratskii, *Adv. Phys.* **47**, 91 (1999).
70. L. Sandratskii and J. Kübler, *J. Phys.: Condens. Matter* **4**, 6927 (1992).
71. D.M. Bylander and L. Kleinman, *Phys. Rev.* **B59**, 6278 (1999).
72. K. Knöpfle, L. Sandratskii, and J. Kübler, *Phys. Rev*. **B62**, 5564 (2000).
73. P. Kurz, G. Bihlmayer, K. Hirai, and S. Blügel, *Phys. Rev. Lett.* **86**, 1106 (2001).

74. D. Hobbs and J. Hafner, *J. Phys.: Condens. Matter* **12**, 7025 (2000).
75. V.P. Antropov, M.I. Katsnelson, M. van Schilfgaarde, and B.N. Harmon, *Phys. Rev. Lett.* **75**, 729 (1995).
76. N.M. Rosengaard and B. Johansson, *Phys. Rev.* **B55**, 975 (1997).
77. M. Uhl and J. Kübler, *Phys. Rev. Lett.* **77**, 334 (1996).
78. S.V. Halilov, H. Eschrig, A.Y. Perlov, and P.M. Oppeneer, *Phys. Rev*. **B58**, 293 (1998).
79. M. Pajda, J. Kudrnovsky, I. Turek, V. Drchal, and P. Bruno, *Phys. Rev*. **B64**, 174402 (2001).
80. S. Stähler, G. Schütz, and H. Ebert, *Phys. Rev*. **B47**, 818 (1993).
81. F. Klose, O. Schulte, F. Rose, W. Felsch, S. Pizzini, C. Giorgetti, F. Baudelet, E. Dartyge, G. Krill, and A. Fontaine, *Phys. Rev*. **B50**, 6174 (1994).
82. S.P. Collins, M.J. Cooper, A. Brahmia, D. Laundy, and T. Pitkanen, *J. Phys.: Condens. Matter* **1**, 323 (1989).
83. H. Maruyama, T. Iwazumi, H. Kawata, A. Koizumi, M. Fujita, H. Sakurai, F. Itoh, K. Namikawa, H. Yamazaki, and M. Ando, *J. Phys. Soc. Jpn.* **60**, 1456 (1991).
84. G. Schütz and P. Fisher, *Z. Physik* **A341**, 227 (1992).
85. G. Schütz and R. Wienke, *Hyperfine Interactions* **50**, 457 (1989).
86. H. Maruyama, A. Koizumi, H. Yamazaki, T. Iwazumi, and H. Kawata, *J. Magn. Magn. Mater*. **104–107**, 2055 (1992).
87. F. Baudelet, C. Brouder, E. Dartyge, A. Fontaine, J.P. Kappler, and G. Krill, *J. Magn. Magn. Mater*. **104–107**, 1418 (1992).
88. J.C. Lang, X. Wang, V.P. Antropov, B.N. Harmon, A.I. Goldman, H. Wan, G.C. Hadjipanayis, and K.D. Finkelstein, *Phys. Rev*. **B49**, 5993 (1994).
89. O. Isnard, S. Miraglia, D. Fruchart, C. Giorgetti, S. Pizzini, E. Dartyge, and J.P. Kappler, *Phys. Rev*. **B49**, 15692 (1994).
90. S. Pizzini, A. Fontaine, E. Dartyge, C. Giorgetti, F. Baudelet, J.P. Kappler, P. Boher, and F. Giron, *Phys. Rev.* **B50**, 3779 (1994).
91. H. Sakurai, F. Itoh, H. Maruyama, A. Koizumi, K. Kobayashi, H. Yamazaki, Y. Tanji, and H. Kawata, *J. Phys. Soc. Jpn*. **62**, 459 (1993).
92. S. Stähler, M. Knülle, G. Schütz, P. Fischer, S. Welzel-Gerth, and B. Buchholz, *J. Appl. Phys.* **73**, 6063 (1993).
93. S. Pizzini, A. Fontaine, C. Giorgetti, E. Dartyge, J.-F. Bobo, M. Piecuch, and F. Baudelet, *Phys. Rev. Lett.* **74**, 1470 (1995).
94. S. Pizzini, A. Fontaine, C. Giorgetti, E. Dartyge, J.-F. Bobo, M. Piecuch, and F. Baudelet, *Physica* **B208–209**, 755 (1995).
95. F. Baudelet, E. Dartyge, G. Krill, J.P. Kappler, C. Brouder, M. Piecuch, and A. Fontaine, *J. Magn. Magn. Mater*. **93**, 539 (1991).
96. F. Baudelet, E. Dartyge, A. Fontaine, C. Brouder, G. Krill, J.P. Kappler, and M. Piecuch, *Phys. Rev*. **B43**, 5857 (1991).
97. F. Itoh, M. Nakamura, and H. Sakurai, *J. Magn. Magn. Mater*. **126**, 361 (1993).
98. S. Pizzini, F. Baudelet, E. Dartyge, A. Fontaine, C. Giorgetti, J.F. Bobo, M. Piecuch, and C. Marliere, *J. Magn. Magn. Mater.* **121**, 208 (1993).
99. S.-Y. Park, S. Muto, A. Kimura, S. Imada, Y. Kagoshima, T. Miyahara, T. Hatano, T. Hanyu, and I. Shiozak, *J. Phys. Soc. Jpn*. **64**, 934 (1995).
100. T. Böske, W. Clemens, C. Carbone, and W. Eberhardt, *Phys. Rev*. **B49**, 4003 (1994).
101. G.R. Harp, S.S.P. Parkin, W.L. O'Brien, and B.P. Tonner, *Phys. Rev*. **B51**, 3293 (1995).
102. W.L. O'Brien, B.P. Tonner, G.R. Harp, and S.S.P. Parkin, *J. Appl. Phys.* **76**, 6462 (1994).
103. D. Weller, Y. Wu, J. Stöhr, M.G. Samant, B.D. Hermsmeier, and C. Chappert, *Phys. Rev.* **B49**, 12888 (1994).
104. M.G. Samant, J. Stöhr, S.S.P. Parkin, G.A. Held, B.D. Hermsmeier, F. Herman, M. van Schilfgaarde, L.-C.Duda, D.C. Mancini, N. Wassdahl, and R. Nakajima, *Phys. Rev. Lett.* **72**, 1112 (1994).
105. P. Strange and B.L. Gyorffy, *J. Phys.: Condens. Matter* **2**, 9451 (1990).
106. N.V. Smith, C.T. Chen, F. Sette, and L.F. Mattheiss, *Phys. Rev*. **B46**, 1023 (1992).
107. H.J. Gotsis and P. Strange, *J. Phys.: Condens. Matter* **6**, 1409 (1994).
108. R. Wu and A.J. Freeman, *Phys. Rev. Lett.* **73**, 1994 (1994).
109. R. Wu, D. Wang, and A.J. Freeman, *J. Appl. Phys.* **75**, 5802 (1994).
110. J. Igarashi and K. Hirai, *Phys. Rev*. **B50**, 17820 (1994).
111. J. Igarashi and K. Hirai, *Phys. Rev*. **B53**, 6442 (1996).
112. P.G. van Engen, K.H.J. Buschow, R. Jongebreur, and M. Erman, *Appl. Phys. Lett.* **42**, 202 (1983).
113. B.M. Lairson and B.M. Clemens, *Appl. Phys. Lett*. **63**, 1438 (1993).
114. G.R. Harp, D. Weller, T.A. Rabedeau, R.F.C. Farrow, and M.F. Toney, *Phys. Rev. Lett.* **71**, 2493 (1993).
115. W.B. Zeper, F.J.A.M. Greidanus, P.F. Garcia, and C.R. Fincher, *J. Appl. Phys*. **65**, 4971 (1989).
116. D. Weller, H. Brändle, G. Gorman, C.-J. Lin, and H. Notarys, *Appl. Phys. Lett.* **61**, 2726 (1992).
117. J. Kübler, *J. Magn. Magn. Mater*. **45**, 415 (1984).
118. M. Podgorny, *Phys. Rev.* **B43**, 11300 (1991).
119. A. Hasegawa, *J. Phys. Soc. Jpn.* **54**, 1477 (1985).
120. T. Tohyama, Y. Ohta, and M. Shimizu, *J. Phys.: Condens. MatPartial density of states, electrons/(atom·eV)ter* **1**, 1789 (1989).
121. T. Suda, M. Shirai, and K. Motizuki, *Int. J. Mod. Phys.***B7**, 765 (1993).
122. M. Shirai, H. Maeshima, and N. Suzuki, *J. Magn. Magn. Mater.* **140-144**, 105 (1995).
123. G. Stajer, C.J. Yahnker, D.R. Haeffner, D.M. Mills, L. Assoufid, B.N. Harmon, and Z. Zuo, *J. Phys.: Condens. Matter* **11**, L253 (1999).
124. K. Iwashita, T. Oguchi, and T. Jo, *Phys. Rev*. **B54**, 1159 (1996).
125. P.M. Oppeneer, V.N. Antonov, T. Kraft, H. Eschrig, A.N. Yaresko, and A.Y. Perlov, *J. Phys.: Condens. Matter* **8**, 5769 (1996).
126. E.T. Kulatov, Y.A. Uspenskii, and S.V. Halilov, *J. Magn. Magn. Mater*. **163**, 331 (1996).
127. S. Uba, L. Uba, A.N. Yaresko, A.Y. Perlov, V.N. Antonov, and R. Gontarz, *Phys. Rev*. **B53**, 6526 (1996).

128. H. Maruyama, F. Matsuoka, K. Kobayashi, and H. Yamazaki, *Physica* **B208–209**, 787 (1995).
129. H. Maruyama, F. Matsuoka, K. Kobayashi, and H. Yamazaki, *J. Magn. Magn. Mater*. **140–144**, 43 (1995).
130. S. Imada, T. Muro, T. Shishidou, S. Suga, H. Maruyama, K. Kobayashi, H. Yamazaki, and T. Kanomata, *Phys. Rev.* **B59**, 8752 (1999).
131. E.E. Alp, M. Ramanathan, S. Salem-Sugui, Jr, F. Oliver, V. Stojanoff, and D.P. Siddond, *Rev. Sci. Instrum*. **63**, 1221 (1992).
132. W. Grange, M. Maret, L.-P. Kappler, J. Vogel, A. Frontaine, F. Petroff, G. Krill, A. Rogalev, J. Goulon, M. Finazzi, and N.B. Brookes, *Phys. Rev.* **B58**, 6298 (1998).
133. T. Shishidou, S. Imada, T. Muro, F. Oda, A. Kimura, S.S.T. Miyahara, T. Kanomata, and T. Kaneko, *Phys. Rev*. **B55**, 3749 (1997).
134. S.P. Collins, *J. Phys.: Condens. Matter* **11**, 1159 (1999).
135. V.N. Antonov, B.N. Harmon, and A.N. Yaresko, *Phys. Rev*. **B64**, 024402 (2001).
136. J.G. Booth, in: *Ferromagnetic Materials*, E.P. Wohlfarth and K.H.J. Buschow (eds.), North-Holland, Amsterdam (1988), Vol. 4.
137. M.B. Stern, in: *Magnetic Properties of Metals*, Vol. 19 *Landolt-Börnstein, New Series, Group III*, H.P.J. Wijn (ed.), Springer-Verlag, Berlin (1986).
138. H.S. Bennet and E.A. Stern, *Phys. Rev.* **137**, A448 (1965).
139. L. Uba, S. Uba, V.N. Antonov, A.N. Yaresko, T. Slezak, and J. Korecki, *Phys. Rev*. **B62**, 13731 (2000).
140. J.H. van Vleck, *Electric and Magnetic Susceptibilities*, Oxford University Press, Oxford (1932).
141. P. Carra, B.N. Harmon, B.T. Thole, M. Altarelli, and G. Sawatzky, *Phys. Rev. Lett.* **66**, 2495 (1991).
142. H. Ebert, *J. Phys.: Condens. Matter* **1**, 9111 (1989).
143. M.S.S. Brooks and B. Johansson, in: *Spin-Orbit Influenced Spectroscopies*, H. Ebert and G. Schütz (eds.), Springer, Berlin (1996), p. 211.
144. J.C. Fuggle and J.E. Inglesfield, *Unoccupied Electronic States. Topics in Applied Physics*, Springer, New York (1992), Vol. 69.
145. G.A. Prinz, *Science* **282**, 1660 (1998).
146. S.A. Wolf, D.D. Awschalom, R.A. Buhrman, J.M. Daughton, S. von Molnar, M.L. Roukes, A.Y. Chtchelkanova, and D.M. Treger, *Science* **294**, 1488 (2001).
147. R.A. de Groot, F.M. Mueller, P.G. van Engen, and K.H.J. Buschow, *Phys. Rev. Lett.* **50**, 2024 (1983).
148. S. Fujii, S. Sugimura, S. Ishida, and S. Asano, *J. Phys.: Condens. Matter* **2**, 8583 (1990).
149. S. Ishida, T. Masaki, S. Fujii, and S. Asano, *Physica* **B245**, 1 (1998).
150. D. Orgassa, H. Fujiwara, T. Schulthess, and W. Butler, *Phys. Rev.* **B60**, 13237 (1999).
151. D. Orgassa, H. Fujiwara, T. Schulthess, and W. Butler, *J. Appl. Phys.* **87**, 5870 (2000).
152. S. Picozzia, A. Continenza, and A.J. Freeman, *J. Appl. Phys.* **94**, 4723 (2003).
153. S. Picozzia, A. Continenza, and A.J. Freeman, *Phys. Rev.* **B69**, 094423 (2004).
154. Y. Miura, K. Nagao, and M. Shirai, *Phys. Rev.* **B69**, 144413 (2004).
155. Y. Miura, M. Shirai, and K. Nagao, *J. Appl. Phys*. **95**, 7225 (2004).
156. T. Block, M.J. Carey, B.A. Gurney, and O. Jepsen, *Phys. Rev.* **B70**, 205114 (2004).
157. I. Galanakis, *Phys. Rev.* **B71**, 012413 (2005).
158. K. Miyamotoa, K. Ioria, A. Kimuraa, T. Xiea, M. Taniguchia, S. Qiaob, and K. Tsuchiyac, *Solid State Commun.* **128**, 163 (2003).
159. K. Miyamotoa, A. Kimuraa, K. Ioria, T. Xiea, K. Sakamotoa, T. Mokoa, S. Qiaob, M. Taniguchia, and K. Tsuchiyac, *Physica* **B351**, 347 (2004).
160. V.N. Antonov, O. Jepsen, A.N. Yaresko, and A.P. Shpak, *J. Appl. Phys.* **100**, 043711 (2006).
161. P. Mavropoulos, I. Galanakis, V. Popescu, and P.H. Dederichs, *J. Phys.: Condens. Matter* **16**, S5759 (2004).
162. P. Mavropoulos, K. Sato, R. Zeller, P.H. Dederichs, V. Popescu, and H. Ebert, *Phys. Rev*. **B69**, 054424 (2004).
163. G.G. Scott, *J. Phys. Soc. Jpn.* **17**, 372 (1962).
164. W. Marshall and S.W. Lovsey, *Theory of Thermal Neutron Scattering*, Oxford University Press, Oxford (1971).
165. M. Blume, *J. Appl. Phys.* **57**, 3615 (1985).
166. L.H. Tjeng, C.T. Chen, P. Rudolf, G. Meigs, G. van der Laan, and B.T. Thole, *Phys. Rev*. **B48**, 13378 (1994).
167. J. Zaanen, G.A. Sawatzky, J. Fink, W. Speier, and J.C. Fuggle, *Phys. Rev.* **B37**, 4905 (1985).
168. J. Schwitalla and H. Ebert, *Phys. Rev. Lett.* **80**, 4586 (1998).
169. C.T. Chen, Y.U. Idzerda, H.-J. Lin, N.V. Smith, G. Meigs, E. Chaban, G.H. Ho, E. Pellegrin, and F. Sette, *Phys. Rev. Lett.* **75**, 152 (1995).
170. G. Vignale and M. Rasolt, *Phys. Rev. Lett.* **59**, 2360 (1987).
171. P. Skudlarski and G. Vigmale, *Phys. Rev*. **B48**, 8547 (1993).
172. M. Higuchi and A. Haegawa, *J. Phys. Soc. Jpn.* **66**, 149 (1997).
173. M.S.S. Brooks, *Physica* **B130**, 6 (1985).
174. O. Eriksson, M.S.S. Brooks, and B. Johansson, *Phys. Rev.* **B41**, 7311 (1990).
175. L. Severin, M.S.S. Brooks, and B. Johansson, *Phys. Rev. Lett.* **71**, 3214 (1993).
176. A. Mavromaras, L. Sandratskii, and J. Kübler, *Solid State Commun*. **106**, 115 (1998).
177. S.V. Beiden, W.M. Temmerman, Z. Szotek, and G.A. Gehring, *Phys. Rev. Lett.* **79**, 4970 (1997).
178. M.T. Czyżyk and G.A. Sawatzky, *Phys. Rev.* **B49**, 14211 (1994).
179. A.I. Liechtenstein, V.I. Anisimov, and J. Zaanen, *Phys. Rev.* **B52**, R5467 (1995).
180. Y. Ma, S. Awaji, M. Watanabe, M. Matsumoto, and N. Kobayashi, *Solid State Commun.* **113**, 671 (2000).
181. P.J. Webster, K.R.A. Ziebeck, S.L. Town, and M.S. Peak, *Phys. Rev.* **B49**, 295 (1984).
182. A.U.B. Wolter, A. Bosse, D. Baabe, I. Maksimov, D. Mienert, H.H. Klau, F.J. Litterst, D. Niemeier, R. Michalak, C. Geibel, R. Feyerherm, R. Hendrikx, J.A. Mydosh, and S. Sullow, *Phys. Rev.* **B66**, 174428 (2002).
183. M. Terada, Y. Fujita, and K. Endo, *J. Phys. Soc. Jpn.* **36**, 620 (1974).
184. K.U. Neumann, T. Kanomata1, B. Ouladdiaf, and K.R.A. Ziebeck, *J. Phys.: Condens. Matter* **14**, 1371 (2002).

185. D.E. Brandao, M.A. Boff, G.L.F. Fraga, and T. Grandi, *Phys. Status Solidi* **A176**, K45 (1993).
186. S. Fujii, S. Ishida, and S. Asano, *J. Phys. Soc. Jpn.* **58**, 3657 (1989).
187. S. Sullowa and C. Geibelb, *J. Magn. Magn. Mater*. **267**, 115 (2003).
188. C. Pfleiderer, G.J. McMullan, S.R. Julian, and G.G. Lonzarich, *Phys. Rev*. **B55**, 8330 (1997).
189. A. Yamasaki, S. Imada, R. Arai, H. Utsunomiya, S. Suga, T. Muro, Y. Saitoh, T. Kanomata, and S. Ishida, *Phys. Rev.* **B65**, 104410 (2002).
190. V.N. Antonov, B.N. Harmon, L.V. Bekenov, A. Shpak, and A.N. Yaresko, *Phys. Rev*. **B71**, 174428 (2005).
191. H. Masumoto and K. Watanabe, *J. Phys. Soc. Jpn.* **32**, 281 (1972).
192. K. Inomata, S. Okamura, R. Goto, and N. Tezuka, *Jpn. J. Appl. Phys.* **42**, L419 (2003).
193. H. Kubota, J. Nakata, M. Oogane, Y. Ando, A. Sakuma, and T. Miyazaki, *Jpn. J. Appl. Phys*. **43**, L984 (2004).
194. K. Kobayashi, R.Y. Umetsu, R. Kainuma, K. Ishida, T. Oyamada, A. Fujita, and K. Fukamichi, *Appl. Phys. Lett.* **85**, 4684 (2004).
195. R.Y. Umetsu, K. Kobayashi, R. Kainuma, A. Fujita, K. Fukamichi, K. Ishidaa, and A. Sakuma, *J. Appl. Phys*. **85**, 2011 (2004).
196. V.V. Krishnamurthy, N. Kawamura, M. Suzuki, T. Ishikawa, G.J. Mankey, P. Raj, A. Sathyamoorthy, A.G. Joshi, and S.K. Malik, *Phys. Rev*. **B68**, 214413 (2003).
197. V.N. Antonov, P.M. Oppeneer, A.N. Yaresko, A.Y. Perlov, and T. Kraft, *Phys. Rev*. **B56**, 13012 (1997).
198. V.N. Antonov, B.N. Harmon, A.N. Yaresko, L.V. Bekenov, and A.P. Shpak, *Phys. Rev.* **B73**, 094445 (2006).
199. M. Guillot and R.P. Pauthenet, *C. R. Acad. Sci. (Paris)* **258**, 3242 (1964).
200. J.P. Bouchaud and R. Fruchart, *C. R. Acad. Sci. (Paris)* **261**, 458 (1965).
201. J.J. Pierre, J.P. Bouchaud, R. Fruchart, M. Guillot, H. Bartholin, and F. Chaisse, *C. R. Acad. Sci. (Paris)* **261**, 655 (1965).
202. J.P. Bouchaud, R. Fruchart, P. Pauthenet, M. Guillot, H. Bartholin, and F. Chaisse, *J. Appl. Phys.* **37**, 971 (1966).
203. D. Fruchart, E.F. Bertaut, F. Sayetat, M.N. Eddine, R. Fruchart, and J.P. Senateur, *Solid State Commun.* **8**, 91 (1970).
204. A. Kenmotsu, T. Shinohara, and H. Watanabe, *J. Phys. Soc. Jpn.* **32**, 377 (1972).
205. D. Fruchart, E.F. Bertaut, B.L. Clerc, L.D. Khoi, P. Veittet, G. Lorthioir, M.E. Fruchart, and R. Fruchart, *J. Solid State Chem.* **8**, 182 (1973).
206. D. Fruchart and B.F. Bertaut, *J. Phys. Soc. Jpn.* **44**, 781 (1978).
207. T. Kaneko, T. Kanomata, and K. Shirakawa, *J. Phys. Soc. Jpn.* **56**, 4047 (1987).
208. K. Motizuki and H. Nagai, *J. Phys.* **C21**, 5251 (1988).
209. T. Kanomata, T. Kavashima, H. Yoshida, and T. Kaneko, *J. Appl. Phys.* **67**, 4824 (1990).
210. H. Maruyamaa, N. Ishimatsua, and N. Kawamurab, *Physica* **B351**, 328 (2004).
211. J.P. Jardin and Labbe, *Physique* **36**, 1317 (1975).
212. M. Shirai, Y. Ohata, N. Suzuki, and K. Motizuki, *Jpn. J. Appl. Phys.* **32**, 250 (1993).
213. M. Takahashi and J. Igarashi, *Phys. Rev.* **B67**, 245104 (2003).
214. V. Antonov, B. Harmon, A. Yaresko, and A. Shpak, *Phys. Rev.* **B75**, 165114 (2007).